# SOLAR FLARE ENERGY DEPOSITION AND RESPONSE THROUGHOUT THE CHROMOSPHERE AND TRANSITION REGION

BY

SEAN G. SELLERS, B.A.

A dissertation submitted to the Graduate School

in partial fulfillment of the requirements

for the degree

Doctor of Philosophy

Major Subject: Astronomy

New Mexico State University

Las Cruces, New Mexico

November 2022

Sean G. Sellers

*Candidate*

Astronomy

*Major*

This Dissertation is approved on behalf of the faculty of New Mexico State University, and is acceptable in quality and form for publication:

*Approved by the Dissertation Committee:*

R. T. James McAteer

*Chairperson*

Jason Jackiewicz

*Committee Member*

Moire Prescott

*Committee Member*

Thomas Hearn

*Committee Member*

# ACKNOWLEDGMENTS

I would be remiss if I did not first acknowledge and thank the several sources of funding for my graduate education. This work is funded in major part via two large research grants: NASA grant NNX17AD31G, and support from DoD Research and Education Program for Historically Black Colleges and Universities and Minority-Serving Institutions (HBCU/MI) Basic Research Funding Opportunity Announcement W911NF-17-S-0010, Proposal Number: 72536-RT-REP. In addition, I was awarded two years of funding through the New Mexico Space Grant (a NASA EPSCoR branch). Finally, I have received several smaller awards that facilitated conference and professional development opportunities, including from the SHINE student travel award, NSO/AURA travel support, and HAO/NOAA travel support.

The guidance and mentorship I have received throughout my education and career have been fundamental any successes I may claim. James McAteer, thank you for your infinite patience, mentorship, and support. This research would quite literally not have been possible without him. Ryan Milligan, another person with seemingly-infinite patience, thank you for the mountains of excellent advice on how to write for a formal academic setting. Sorry the paper took so long.

Even before graduate school, I had the great fortune to learn from giants of astronomy. Thank you to Dr. Colette Salyk, both for prompting me to learn Python, and for giving me my first real experience with astronomical research. Thank you to Dr. Fred Chromey, for teaching me the fundamentals of how to trap light in a bottle, as well as the admonitions not to "waste photons" when we occasionally failed. Dr. Debra Elmegreen, I could never begin to thank enough for the inspiration to try to be one of the legion of (slightly strange and frequently reclusive) scientists willing to throw open the gates of the universe.

I can honestly say that I would not have made it through graduate school without the cadre of friends and coworkers who made the entire experience bearable. Were I to give you all the thanks you deserve, the science wouldn't begin until somewhere around page 90. In short, thank you to all of my officemates, including Laurel, Emma, and Ethan, both for putting up with me, and for your

humor, validation, and support. To Jodi, David, Sarah, Sam, Caleb, Rachel (I of II), Candace, and Sam, friends and members of D&D groups both past and present, thank you for the escapism, excellent stories, and hours of camaraderie. Rachel (II of II) and Emmy, two of the best friends anyone could ask for, thank you for, well, everything. Rachel, particularly, thank you for not letting me drop out. It was a close call there a few times.

I would not be where I am today if not for my family, particularly my parents and my brother, Ethan. Thank you all for supporting me, and steadily refusing to believe that I *wouldn't* be able to graduate. Refusing to accept an alternative is more helpful sometimes than anyone could guess. Mom and Dad, thank you for raising me to be stubborn. I'm sure that was a pain for you, but it's really helped me.

Finally, to Julie. There's nothing I could write here that would adequately express the million ways your support and care have made my life infinitely better, just by virtue of existing. Thank you for the adventures, and for the constant belief.

# VITA

## EDUCATION

2012 - 2016 B.A., Physics & Astronomy with Honors
Vassar College
Poughkeepsie, NY, USA

## FIELD OF STUDY

Major Field: Solar Astronomy

## PUBLICATIONS

S. G. Sellers, R. O. Milligan, and R. T. J. McAteer *Call and Response: A Time-resolved Study of Chromospheric Evaporation in a Large Solar Flare*, 2022, The Astrophysical Journal, 936, 85

## CONFERENCE PROCEEDINGS

S. G. Sellers, R. T. J. McAteer, *Mr. Ellerman Or: How I Learned to Stop Wasting Photons and Watch the Bomb*, the 2022 Triennial Earth-Sun Summit (TESS), Aug. 2022

S. G. Sellers, R. O. Milligan, and R. T. J. McAteer *Call and Response: A Time-Resolved Electron Driver and its Consequences*, Solar Heliospheric and INterplanetary Environment (SHINE), Jun. 2022

## WORKSHOPS

*ASP, HAO, NCAR colloquium Solar Spectropolarimetry and Diagnostic Techniques*, attended Oct. 2018

*DKIST Critical Science Plan Workshop 5: Wave Generation and Propagation*, attended Dec. 2018

*2nd NCSP DKIST Data Training Workshop: Image treatment and time series*, attended Jan. 2020

*3rd NCSP DKIST Data Training Workshop: Milne-Eddington Spectropolarimetric Inversions*, attended Jul. 2020

*4th NCSP DKIST Data Training Workshop: An Introduction To Chromospheric Diagnostics*, Attended Jun. 2021

## AWARDS AND GRANTS

This work was funded by NASA grant NNX17AD31G and support from DoD Research and Education Program for Historically Black Colleges and Universities and Minority-Serving Institutions (HBCU/MI) Basic Research Funding Opportunity Announcement W911NF-17-S-0010, Proposal Number: 72536-RT-REP, Agreement Number: W911NF-18-1-0484.

Sunspot Solar Observatory Research and Outreach Fellowship (2018, 2019)

Sellers, S. G. (PI) & R. T. J. McAteer (Advisor) "The Explosive Sun: Characterizing the Chromospheric Response to Solar Flares" *New Mexico Space Grant* (2018, 2019)

## PROFESSIONAL ORGANIZATIONS

American Astronomical Society (Solar Physics Division)

## LEADERSHIP AND PROFESSIONAL EXPERIENCE

2018–2019 President, Astronomy Graduate Student Organization

2019–2020 President, NMSU Graduate Student Council

ABSTRACT

SOLAR FLARE ENERGY DEPOSITION AND RESPONSE
THROUGHOUT THE CHROMOSPHERE AND TRANSITION REGION

BY

SEAN G. SELLERS, B.A.

Doctor of Philosophy
New Mexico State University
Las Cruces, New Mexico, 2022
Dr. R. T. James McAteer, Chair

Solar flares are highly energetic events which can release up to $\approx 10^{32}$ ergs over the span of minutes. This energy is built and released in the corona, and is partitioned into several flare-associated phenomena. A significant fraction of flare energy is partitioned into the acceleration of nonthermal particles, which deposit their energy through nonthermal impacts in the solar chromosphere. The chromosphere serves as the reservoir of gas that is tapped to form hot, post-flare loops, but many aspects of the energy deposition and transport in the immediate wake of the injection of nonthermal particles are unclear.

Chromospheric signatures of nonthermal flare energy deposition are varied, and include small-scale brightenings around the energy injection sites, strong velocity flows that are frequently observed to be bidirectional, dramatic increases in

the widths of spectral lines, and significant density enhancements. The purpose of this research is to connect the profile of nonthermal energy injection to the deposition and response throughout the chromosphere and transition region.

For the purposes of studying flare-driven chromospheric evaporation, a study is made of an X1.6 flare, SOL2014-10-22. This entirety of the nonthermal injection event was covered by a variety of instruments. From this, we derived the energy contained in nonthermal electrons, and link the time-dependent profile of energy injection to the response in Doppler velocity, nonthermal velocity, and density, as a function of time, temperature, wavelength and space. The fast-temporal variations in nonthermal energy injection and deposition is studied via ground-based observations of the low chromosphere, which are connected to X-ray flux as a proxy for nonthermal energy. These observations provide invaluable observations of fundamental time variations of the nonthermal event, and connect these to the smallest-scale X-ray linked structures. Taken together, this work provides valuable characterizations and constraints for the refinement, guidance, and initialization of the hydrodynamic flare simulation codes that will be valuable tool for advancing our understanding of the flare phenomenon throughout the peak of the next solar cycle.

**Contents**

## LIST OF TABLES

## LIST OF FIGURES

LIST OF ABBREVIATIONS

| **Spectral ranges:** | |
|---:|---|
| HXR | Hard X-ray |
| SXR | Soft X-ray |
| UV | Ultraviolet |
| EUV | Extreme Ultraviolet |
| FUV | Far Ultraviolet |
| NUV | Near-Ultraviolet |
| **Instruments** | **& Telescopes:** |
| RHESSI | Reuven Ramaty High Energy Solar Spectroscopic Imager |
| STIX | Spectrometer Telescope for Imaging X-rays |
| EIS | EUV Imaging Spectrometer |
| IRIS | Interface Region Imaging Spectrograph |
| SDO | Solar Dynamics Observatory |
| AIA | Atmospheric Imaging Assembly |
| HMI | Helioseismic and Magnetic Imager |
| DST | Dunn Solar Telescope |
| IBIS | Interferometric BI-dimensional Spectropolarimeter |
| ROSA | Rapid Oscillations in the Solar Atmosphere |
| FIRS | Facility InfraRed Spectropolarimeter |
| UBF | Universal Birefringent Filter |
| DKIST | Daniel K. Inouye Solar Telescope |
| GOES | Geostationary Operational Environmental Satellite |
| **Jargon:** | |
| SAA | South Atlantic Anomaly |
| RMC | Rotating Modulation Collimator |
| KISIP | Kiepenheuer Institute Speckle Interferometry Package |
| FRT | Flow Reversal Temperature |
| AO | Adaptive Optics |
| HSM | Helmli & Scherer's Mean |
| SRM | Detector Response Matrix |

# 1. INTRODUCTION

## 1.1. The Sun and Solar Atmosphere

The Sun (see Figure 1.1) is a roughly-spherical collection of hydrogen, helium, and trace elements bound by its own gravity, and supported through much of its interior by hydrostatic pressures. By various metrics, it is a G2V star located at a distance of approximately 149 million kilometers from the Earth. It has a radius of $7 \times 10^{10}$ cm, and a mass of $2 \times 10^{33}$ g (Phillips 1995). Much of the mass of the Sun is reasonably well-behaved, insofar as any plasma can be. The core of the Sun is typically defined as the innermost ≈20% of its radius, contains half of the mass of the star, and undergoes nuclear fusion through various, primarily proton-proton chain reactions, at a fairly constant rate. The energy generated through this process totals a fairly-constant $3.8 \times 10^{33}$ erg $s^{-1}$. At Earth, this corresponds to an irradiance of $1.4 \times 10^{10}$ erg $s^{-1}$ $m^{-2}$. Variations in this irradiance are of extremely small amplitudes, on the order of 0.2% (Gough 1981). Once liberated from the hydrogen mass in the solar core, energy in the form of photons makes a tedious path through the radiative zone of the Sun. Extending from the edge of the solar core to 70% of the Sun's radius, the radiative zone comprises another ≈48% of the Solar mass. Here, still, the plasma is easily characterized. It is fully ionized, and atomic nuclei exist free of both the pressures of nuclear fusion, and the interminable quantified movements of electrons. Photons propagate through this region, taking long, meandering, thirty-thousand year pathways that are statistically trivial to characterize (Spiegel & Zahn 1992).

It is at this point that the plasma ceases to be well-behaved.

As the temperature gradient grows near the edge of the radiative zone, the convective movement of plasma becomes the most efficient energy transport process. The outer 30% of the Sun's radius, comprising 2% of its mass is entirely convective. The bottom of the convective zone is a shear interface layer. It is at this depth that the Sun ceases to rotate as a solid body, and begins to rotate differentially (Thompson et al. 2003; Miesch 2005), with longer rotation periods near the poles than the equator. Strong shear flows at the tachocline generate intense electrical currents, which in turn induce magnetic flux (Jones et al. 2010; Cameron et al. 2017). Tubes of magnetic flux are buoyed upward, with advection binding and deforming the flux tubes in the process.

The top of the convective zone signals a sudden change in density, and, coincidentally, the optical depth of the plasma. The top of the convective zone, the photosphere, is usually considered to be the "surface" of the sun, as the energy initially produced by fusion is radiated into space. The tops of convective cells are plainly visible as photospheric granules. It is here that the magnetic field becomes plainly visible.

Sunspots are dark spots appearing in the photosphere where convection is suppressed or absent. Their discovery is typically attributed to Galileo, from drawings around 1610 CE, and they were (often sporadically) catalogued for the next 300 years before the first clues as to their origin were unearthed. Hale (1908), using polarizing optics obtained on a hunch in the wake of the discovery of the Zeeman effect (Zeeman 1897) found signatures of kiloGauss-strength magnetic fields within sunspots. Gathered by plasma motions, and eaten at by advective currents, these features, larger in some cases than the planet Earth, are fully caused by the gathering of magnetic flux.

It is at this point that the plasma becomes exceptionally ill-behaved.

The solar atmosphere consists (broadly) of the chromosphere, transition region, and corona. The chromosphere, just above the photosphere is a factor of $10^4$ times less dense than the photosphere. The sudden drop in density coincides with a sudden drop in plasma pressure. In the solar atmosphere, the pressure due to magnetism becomes dominant (Mariska 1992a). This is usually expressed as the plasma $\beta$ parameter, which is the ratio of the plasma pressure to the magnetic pressure. Within the photosphere, the plasma pressure is dominant, and magnetic structures, like sunspots are confined. Not so throughout the solar atmosphere (Gary 2001). As the plasma $\beta$ becomes significantly less than 1, the atmosphere becomes dominated by magnetic structures, filamentary, looping and chaotic. This continues into the corona, the upper layers of the solar atmosphere, visible at extreme ultraviolet (EUV) wavelengths and during eclipses. Figure 1.1 shows the Sun as it appeared on 2022-10-10 across a variety of atmospheric layers from the photosphere to the low corona. The changing nature of structure with height is plainly visible. Figure 1.2 shows the evolution of the plasma $\beta$ parameter through the atmosphere, and Figure 1.3 shows the evolution of various structures throughout the solar atmosphere.

## 1.2. Solar Flares: A Qualitative Overview

Solar flares are extremely energetic events, with characteristic signatures across decades of spatial scales, temporal scales, and energy scales. A full overview of the physics leading to and resulting from a solar flare is beyond the scope of this introduction. An overview of the triggering event and immediate aftermath

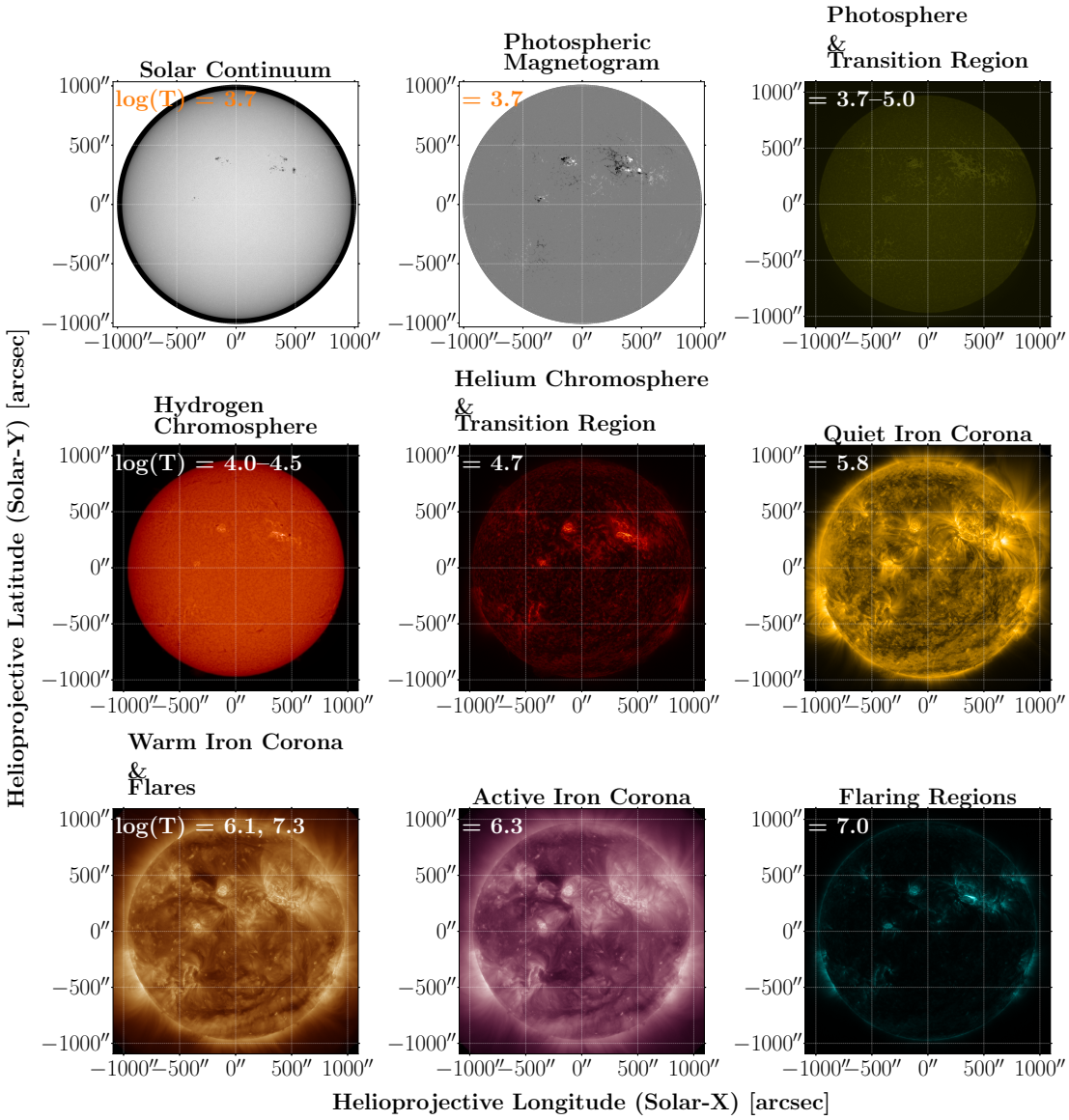


Fig. 1.1.— Images of the Sun as it was at midnight (UTC) on 2022-10-10, from the photosphere to the corona. Images of the photosphere and magnetic field are from the Helioseismic and Magnetic Imager aboard the Solar Dynamics Observatory, and the image of the Hydrogen Chromosphere is from the Global Oscillation Network Group. All other images are from the Atmospheric Imaging Assembly aboard the Solar Dynamics Observatory. The last is discussed in Chapter 2.4.

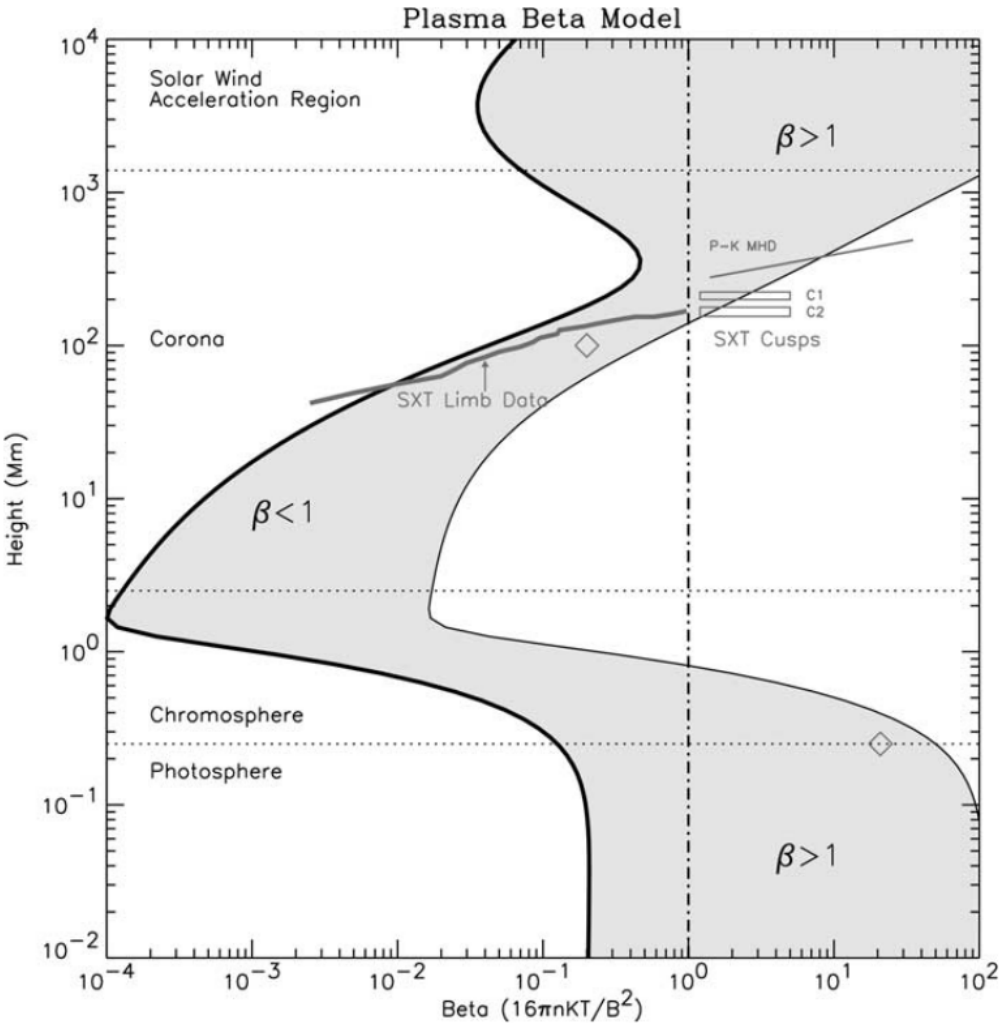


Fig. 1.2.— Plasma $\beta$ parameter as a function of height throughout the solar atmosphere. Reproduced from Gary (2001)

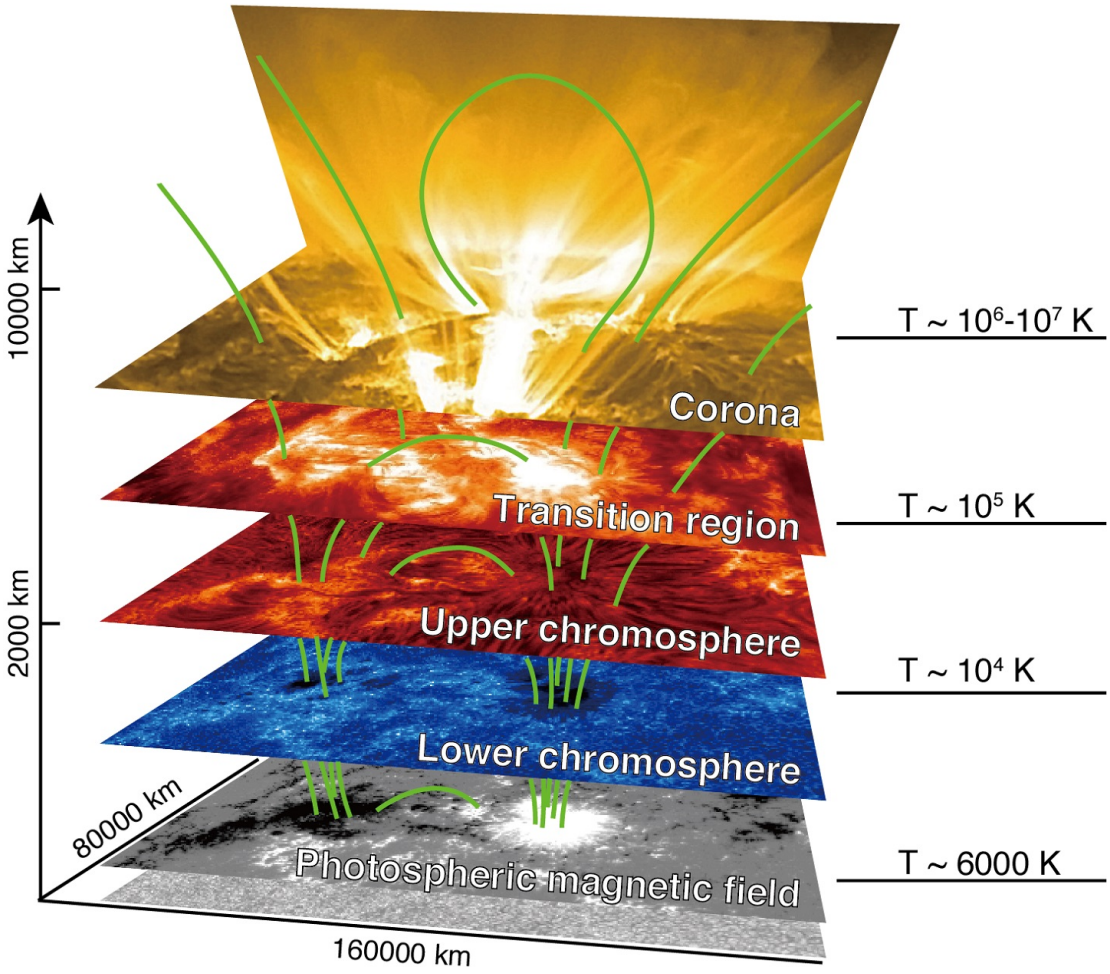


Fig. 1.3.— The structure of the magnetic sun. As plasma-$\beta$ decreases, the nature of solar structure changes from small-scale convective bubbles to elongated filaments and loops. Image courtesy of Solar-C, NOAJ/JAXA, NASA

can be found in Chapter 3, and this section will serve as a very basic overview. For an exhaustive overview, the reader might consider review articles by Fletcher et al. (2011); Milligan (2015); Shibata & Magara (2011).

At the most basic level, a solar flare is a localized, short-term (on the order of minutes to hours) enhancement in intensity. This enhancement is present at wavelengths across the electromagnetic spectrum, but need not be ubiquitous. The first flare, observed simultaneously (by the nature of the event) by astronomers Carrington and Hodgson (Carrington 1859; Hodgson 1859) was observed in the solar continuum (or white light). However, white light measurements for many years were overshadowed by other spectral bands in which the emission is more pronounced. Of particular note is the dramatic response in H$\alpha$, in which ribbons of heated plasma are observed to quickly unravel across the active region. For many years, flares were considered to be a chromospheric phenomenon, and classification was performed through the maximal disk coverage in H$\alpha$ (Tandberg-Hanssen & Emslie 1988). In more modern times, solar flares are classified through their flux in soft X-Ray (SXR) bands, which has proven to be a robust categorization system with a direct link to the energy release of the event (Reep et al. 2013).

Flares exhibit four main phases of development, each marked by emission in different wavelength regimes. The pre-flare phase spans the few moments before the event, and is marked by gradual increases in the SXR and EUV bands. The impulsive phase marks the main injection of energy into the lower solar atmosphere. During the impulsive phase, the most striking change is the sudden onset of emission in hard X-rays (HXR) energies (typically, emission above $\approx$ 15 keV can be considered HXR). Various radio bands also see sharp increases in emission, and small-scale, quickly-varying emission is seen in chromospheric lines, such as

H$\alpha$, the Ca II H& K doublet, and the infrared Ca II 8542Å line. The impulsive phase is short, lasting only a few minutes, and is followed by the flash phase. The flash phase can (and frequently does) overlap in time with the impulsive phase. During the few minutes that the flash phase lasts (usually $<$ 10 minutes), thermal energy is being distributed throughout the solar atmosphere, and the plasma pressure is increasing. This causes a rapid increase in H$\alpha$ intensity and line width. Overlapping with the flash phase is the gradual, or decay phase. Depending on which metrics are available, this is sometimes considered to begin when the SXR emission peaks, typically just after the end of HXR emission. The decay phase is the end of the flare, as the coronal and chromospheric plasma gradually returns to a nearly pre-flare state in terms of temperature, velocity, and density. This phase can be quick, lasting less than an hour, or extremely slow, lasting several hours. The length of this phase typically (but not always) correlates with the peak energy in SXR bands, with small events having short decay phases, and large events long decay phases. In the extreme case of SOL2003-11-04, the largest "modern" flare, with a *GOES* classification in excess of X25, the decay phase was evident for more than a day in the wake of the event. Figure 1.4 illustrates these phases for a generalized case.

On a slightly more complex level, a solar flare is the result of magnetic energy release in the solar atmosphere. The magnetic field, as it emerges from sunspots at the base of active regions, forms vast arcades of loops filled with trapped plasma throughout the chromosphere and corona. The differential rotation of the Sun and resultant shear cause these loops to form in geometries that are neither stable, nor simple. As these regions of field evolve, solutions to remedy unstable energy buildup present themselves. As loops with opposite direction polarity are forced

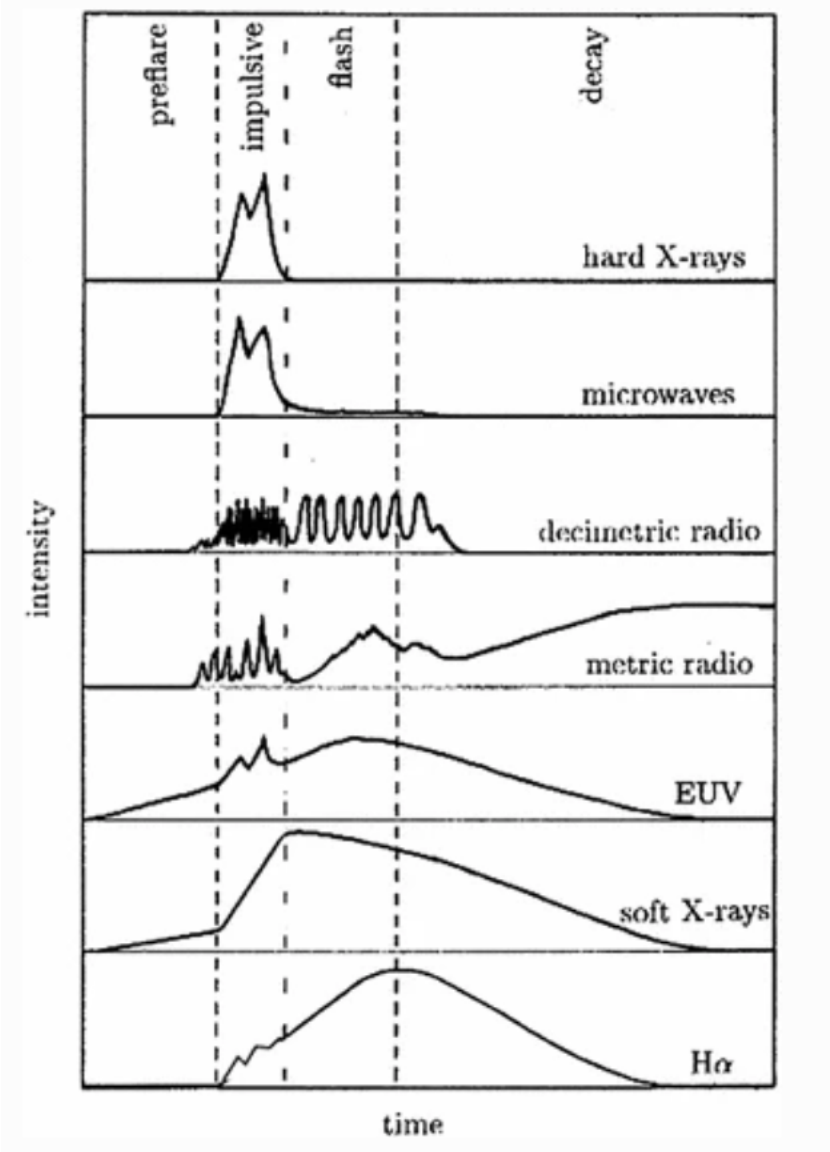


Fig. 1.4.— From Benz (2002), a schematic diagram of flare intensity across several wavelength regimes. The various phases can vary greatly with flare energy.

together, conditions in the solar atmosphere can lead them to reconnect, forming a new arcade of loops with a lower energy state. The process by which this is theorized to occur is called magnetic reconnection (discussed further in Chapter 3.1), and results in a significant release of energy over the span of seconds. Some of this energy is partitioned into the acceleration of particles.

These particles stream down the magnetic field lines from the reconnection site in the corona, at which point they encounter an obstacle in the form of the chromosphere. It is at this point that matters become complex. The sudden impact of nonthermal particles drives significant evolution within the chromosphere, driving, among other processes, the velocity flows that fill hot, post-flare loops with chromospheric plasma. This, of course, is not the extent of the changes inflicted upon the chromosphere by the injection of nonthermal energy. Among others are the rapid heating of chromospheric plasma, the compression of the local transition region into the chromosphere, sharp increases in density, increases in the nonthermal width of optically-thin spectral lines, and the excitation of a variety of quasi-periodic oscillations.

## 1.3. The State of the Art

Solar flares are pan-spectral events with varying signatures depending on the wavelength regime studied. In some spectral ranges, the signatures of the nonthermal particle deposition are quite obvious, such as the HXR regime and millimeter-wave radio. Others are sensitive to the thermal energy deposition, such as the core of H$\alpha$, and certain spectral lines are highly sensitive to density increases, velocity flows, and nonthermal broadening processes.

As the tools available to the community of solar astronomers increases, so too do the connections we are able to make between linked dynamic processes. Flares are fast, impulsive events that cause discontinuous breaks in every local metric, a vast puzzle extending from the photosphere to the outer corona. Every instrument added to the arsenal of solar physics illuminates a different piece of the puzzle. To reveal even the general shape of the full picture, an array of instruments is required.

The chromospheric pieces of the puzzle have long been shrouded in mystery. Despite being the primary layer of flare energy deposition, investigations of the chromosphere are difficult. The resting chromosphere exists outside of local thermodynamic equilibrium, and responds in often surprising ways to flare energy deposition. Empirical observations are frequently the best window into a general understanding, but these processes evolve quickly, last for many hours, and have important observational signatures at both length scales too small to resolve even with modern telescopes and too large for instruments with small fields of view. Coordinated observations using multiple instruments have opened new insights into the processes occurring within the post-flare chromosphere, but a full picture requires high resolution in each space, time, wavelength, and temperature.

## 1.4. Research Questions

This dissertation project attempts to resolve uncertainties surrounding the deposition of nonthermal energy during solar flare events. This is done by connecting flux in nonthermal hard X-ray emission to response signatures throughout the solar transition region and chromosphere. Tracing and accounting for these

energy signatures will allow for a more complete picture of atmospheric flare energy deposition. The deposition processes are important for understanding the conditions that will affect and change an active region in the wake of a flare event, including the bulk movements of mass and thermal energy. More specifically, this work seeks to answer:

1. How does chromospheric plasma evolve throughout the duration of, and in the immediate aftermath of, a temporally-resolved nonthermal energy injection event as a function of space, time, and temperature?

2. Can bright, short-lived, burst-like features in the wings of H$\alpha$ 6563Å and Ca II 8542Å reveal the locations of fine-scale nonthermal energy deposition and HXR production?

A detailed description of the instruments used in these projects is provided in Chapter 2, and an overview of the physical processes linked to solar flares can be found in Chapter 3. The first research question is addressed in Chapter 4 by comparing UV and EUV intensities, Doppler velocities, nonthermal velocities, and densities with the derived electron injection profile from a large solar flare. The approach taken is use HXR spectroscopy to derive the nonthermal energy profile, and couple it to an independent, time-dependant measurement of the deposition area. The energy deposition profile was compared against a menagerie of high-cadence spectral observations, which span a wide wavelength and characteristic temperature range.

The second question is discussed in Chapter 5 by comparing three days of ground based observations with flare-associated X-ray emission across these days.

A source extraction and tracking algorithm was developed to follow the evolution of flare kernels across periods of variable seeing. Extracted profiles were subject to comparison with curated HXR lightcurves, searching for intensity and oscillatory signatures characteristic of the HXR event.

With the rise of Solar Cycle 25, new observatories and instruments are becoming available that will allow us to follow up on these studies in greater detail. The new STIX (Krucker et al. 2020) and SPICE (Spice Consortium et al. 2020) instruments aboard Solar Orbiter will enable a new era of space based observations, closely complementing the capabilities of the multitude of venerable space- and ground-based observatories. Their unique heliocentric positioning will be vital for studying the activity that will accompany the rise of this new solar cycle. From the ground, the instruments at the Dunn Solar Telescope will complement the newest state-of-the-art available at the Inouye Solar Telescope (IST), whose unprecedented spatial resolution will revolutionize our understanding of the small-scale processes responsible for the buildup and release of magnetic energy over the solar cycle.

# 2. AN OVERVIEW OF RELEVANT INSTRUMENTATION & DATA

Solar observatories and instruments are quite unlike their night sky brethren. The abundance of photons from our stellar neighbor has allowed incredibly sophisticated observations, but with sophistication comes complication and specialization. This complication has led the field into the era of multi-messenger solar flare studies, where it is now necessary to use multiple instruments and a wide wavelength regime. This chapter is devoted to a brief description of each instrument used in this work, its operational concept, reduction processes, and the methodology used to obtain the final data products.

Each section of this chapter is devoted to a different instrument. Chapter 2.1 discusses the *RHESSI* HXR observatory, Chapter 2.2 discusses the *EIS* instrument aboard the *Hinode* observatory, Chapter 2.3 is devoted to the *IRIS* spacecraft, Chapter 2.4 provides a brief overview of the *AIA* instrument aboard *SDO*, and Chapter 2.5 is dedicated to the suite of ground-based instrumentation at the Dunn Solar Telescope in Sunspot, NM. This information is additionally summarized in Table 2.1.

## 2.1. The Reuven Ramaty High Energy Solar Spectroscopic Imager (RHESSI)

*RHESSI* (Lin et al. 2002; Hurford et al. 2002) was a solar X-ray observatory active from 2002 until its decommissioning in mid-2018. The observatory returned high-cadence observations of the solar X-ray spectrum from 3 keV to 17 MeV through two solar maxima, and, in doing so, revolutionized our understanding of

Table 2.1: Summary of Instrumentation

| Name: | Data Type: | Wavelength Regime | Spatial Resolution (Approximate) | Atmospheric Layer (Approximate) |
|---|---|---|---|---|
| ***RHESSI*** | Imaging<br>Spectroscopy<br>Time Series | HXR<br>3 keV – 17 MeV | 2.26″ | Chromosphere<br>Corona |
| ***EIS*** | Spectroscopy<br>Raster Imaging | EUV<br>170–210Å<br>250–290Å | 1″ | Transition Region |
| ***IRIS*** | Spectroscopy<br>Raster Imaging<br>Slit-jaw Imaging | NUV & FUV<br>1331.7–1358.4Å<br>1389–1407Å<br>2782.7–2851.1Å | 0.33″ | Transition Region<br>Chromosphere |
| ***AIA*** | Imaging | EUV & FUV<br>7 EUV Filters<br>2 FUV Filters | 0.6–1.0″ | Low Corona<br>Temperature Minimum (400–500 km) |
| ***IBIS*** | Imaging<br>Spectroscopy<br>Polarimetry | Visible (red)<br>Variable<br>(Typically 5500–9000Å) | 0.33″ | Chromosphere (1500–2800 km)<br>Photosphere |
| ***ROSA*** | Imaging | Visible (blue)<br>Variable<br>(Filters Typically < 5000Å | 0.2–0.33″ | Low Chromosphere (< 1300 km)<br>Photosphere (≈ 250 km) |

the high-energy processes associated with solar flares (Krucker et al. 2008; Benz 2017). Throughout this work, *RHESSI* lightcurves, spectra, and reconstructed images are used to quantify and compare the specifics of HXR emissions with the response throughout the solar atmosphere.

At its core, *RHESSI* consisted of nine high-purity germanium crystal detectors, electrically divided into front and rear segments. For this work, only the front segments, sensitive to emission up to 250 keV, were used. Several factors necessitate care when selecting and working with *RHESSI* data. The combination of the spacecraft's 90 minute orbital period and intersection with the South Atlantic Anomaly result in a duty cycle of ≈43% for all detectors, with the exception of detector 8 which has a slightly lower duty cycle as a result of interference with the spacecraft's antenna during transmission windows. For the purposes of this study, the impulsive phase of a given flare must be captured within the active portion of

the *RHESSI* duty cycle, as the impulsive phase coincides with the primary release of nonthermal energy (Fletcher et al. 2011).

Additionally, the each detector experienced periods of reduced sensitivity, or loss of energy discrimination. In particular, detectors 2 and 7 experienced problems from the mission outset. Attempts to recover sensitivity, and even revive degraded detectors were possible due to the five anneal periods the spacecraft successfully completed. Annealing is the process of heating the detectors above their 115 K operating temperature in order to repair radiation damage in the germanium crystals. This process had mixed results, thus care was taken to work with each viable detector as a separate instrument. Significant processing is required before the set of working detectors can be combined to form a single spectrum or lightcurve.

### *2.1.1. RHESSI Spectra & Lightcurves*

The *RHESSI* detectors have a theoretical cadence of ≈1 ms, corresponding to the frequency of live time measurements. In practice, during flares, the minimum theoretical cadence is closer to 100 ms. The discrepancy is due to the pulse-pileup phenomenon. Each *RHESSI* detector measures the time and energy of an incident X-ray, however, when two events with similar energies occur within a short enough time frame (50 ms), the spacecraft measures a single event with twice the energy. Even with longer time bins, this effect is pronounced, and requires corrections in the spectral fitting process. The effective minimum cadence after detector degradation circa 2013–2014 is approximately 2 seconds for simple lightcurves, and 16 seconds for spectra requiring detailed fitting.

### *2.1.2. RHESSI Images*

The detectors themselves carried no spatial information, but merely recorded the precise time and energy of incident photons. Spatial information is provided by the Rotating Modulation Collimator (RMC) system. The RMC system consists of 9 sets of two grids each, placed in front of each detector. The grids consist of parallel slats of X-ray blocking material, separated by X-ray transmitting windows, with a different width per each detector. Each grid pair is mounted to either end of the 1.55 m RMC assembly. The result is that, for an instantaneous moment in time, each detector is sensitive to X-rays from a subset of incidence angles defined by the grid spacing. The maximum resolution is determined by the finest grid spacing, which is 2.26″for detector 1.

The 4-second rotation period of the spacecraft causes these grids to selectively occult X-rays from various position angles, allowing imaging via Fourier component reconstruction, without having to focus or divert X-rays (Lin et al. 2002; Hurford et al. 2002). In theory, images could be made for periods as short as a few tens of ms with a subset of Fourier components, and the full spatial resolution could be realized with an integration time of 2 seconds. In practice, by 2013–2014, multiple rotations are required to compute usable images.

There are several image reconstruction algorithms available for application to *RHESSI* data. For this work, images are primarily formed using the `CLEAN` algorithm, and various maximum entropy methods (`MEM_GE`, Bong et al. (2006); Narayan & Nityananda (1986); Schmahl et al. (2007); Massa et al. (2020)). These algorithms were originally developed for radio interferometry, however, the visibilities derived from radio antenna baseline pairs and those derived from *RHESSI*

detector grid spacing are extremely similar. A full review of these algorithms can be found in Dennis & Pernak (2009); Warmuth & Mann (2013), and Massa et al. (2020). Briefly, the `CLEAN` algorithm assumes a source can be expressed as a superposition of point sources, and fits point sources to the backtraced "dirty" map, which are formed directly from the modulated count rate in each detector. Maximum entropy methods use visibilities computed from the modulated detector count rate. Each visibility is a vector representation of the amplitude and phase of a given spacecraft roll angle. These visibilities are used to maximize the computed entropy function. Maximum entropy methods are, using this information, able to resolve sources smaller than the the finest *RHESSI* grid pair. Figure 2.1 shows a comparison between `CLEAN` and `MEM_GE` image creation techniques. While the HXR sources shown in Figure 2.1 are noticeably more compact when the image is formed using the `MEM_GE` algorithm when compared to the `CLEAN` image, the `MEM_GE` algorithm likely still overestimates HXR source sizes (Dennis & Pernak 2009). The various maximum entropy methods are also prone to source breakup, particularly when the regularization parameter is not well-matched to the flare, when the finest grid pair spacings are included, or when the number of visibilities is small.

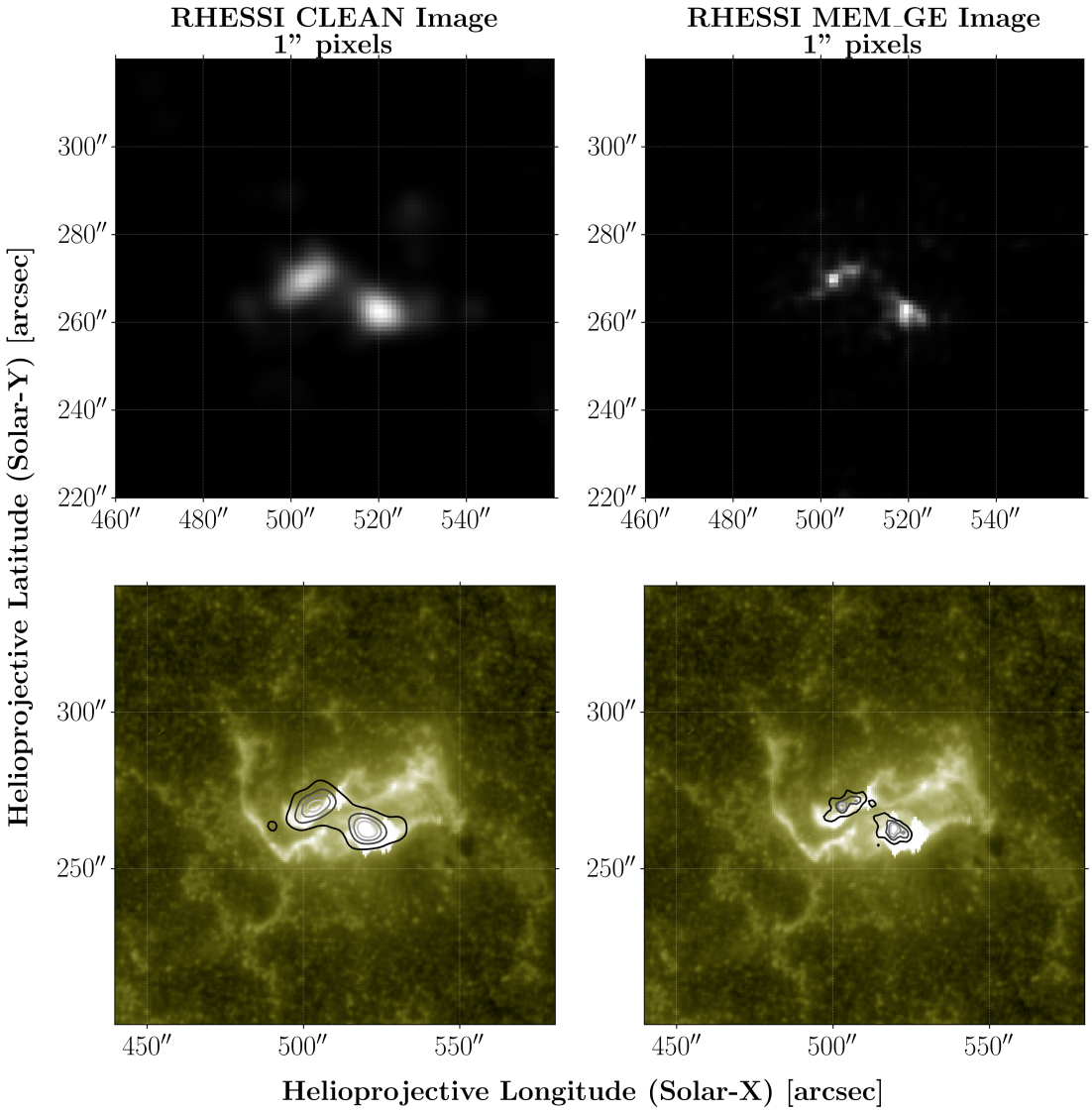


Fig. 2.1.— Comparison between methods of forming *RHESSI* images. An image formed using the CLEAN algorithm is shown in the left column as an intensity map (**Top**) and as contours against a context *AIA* 1600Å image (**Bottom**). The right column shows the same for an image formed using the MEM_GE algorithm. Images were formed during an X1.0 flare on SOL2014-03-29 for an energy range spanning 30–100 keV. Contours are shown at the 10%, 30%, 50%, 70%, and 90% levels. All nine detector front segments were used in the reconstruction of these images.

## 2.2. The Extreme Ultraviolet (EUV) Imaging Spectrometer (EIS)

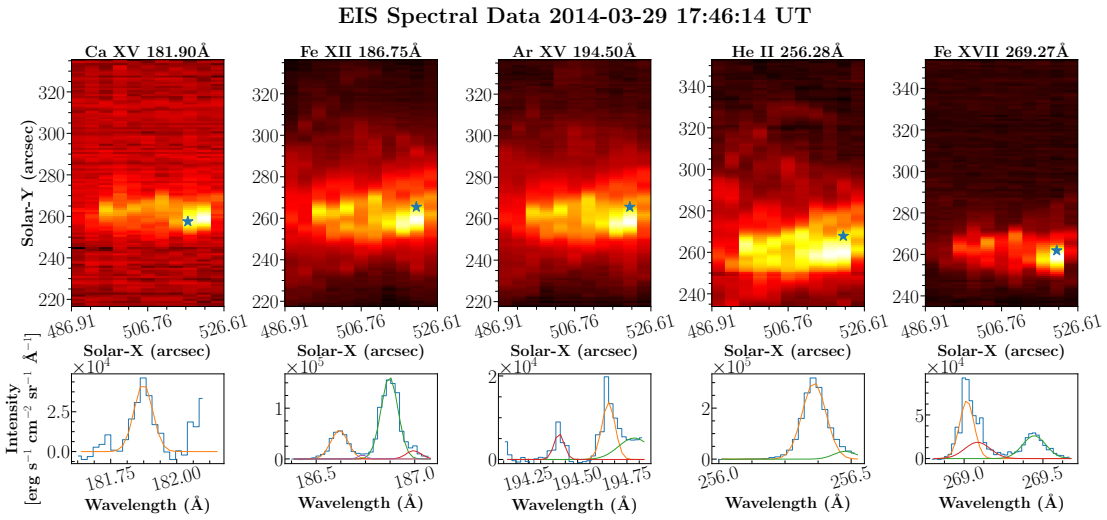


Fig. 2.2.— An example of *EIS* data from SOL2014-03-29 during an X1.0 flare. The top row shows the integrated emission in each spectral line window. The blue star denotes the location used to form the example spectrum shown in the bottom row. Example spectra are fit with a combination of Gaussian profiles to highlight the blended nature of *EIS* emission lines.

*EIS* (Culhane et al. 2007) is a slit spectrometer aboard the *Hinode* spacecraft, launched in 2006. The instrument is a two channel slit spectrometer, spanning 170–210Å, and 250–290Å. These spectral ranges correspond to temperatures characteristic to transition region, coronal, and flare lines. While the instrument has several modes, including slot imaging capabilities, the data set used in this work is an active region rastering mode, consisting of 20 slit positions using a 2″slit.

The emission lines observed by *EIS* are optically thin, and are prime targets for measuring Doppler and nonthermal velocities across a wide range of temperatures. Though optically thin, spectral fitting for *EIS* is complicated by line blends.

Nevertheless, once instrumental decay has been accounted for (Del Zanna 2013; Warren et al. 2014), the *EIS* instrument provides some of the best direct velocity and nonthermal width measurements available. The multiple spectral windows additionally contain numerous density-sensitive line pairs, including the Fe XIV 264274Å line pair used in this work.

## 2.3. The Interface Region Imaging Spectrometer (IRIS)

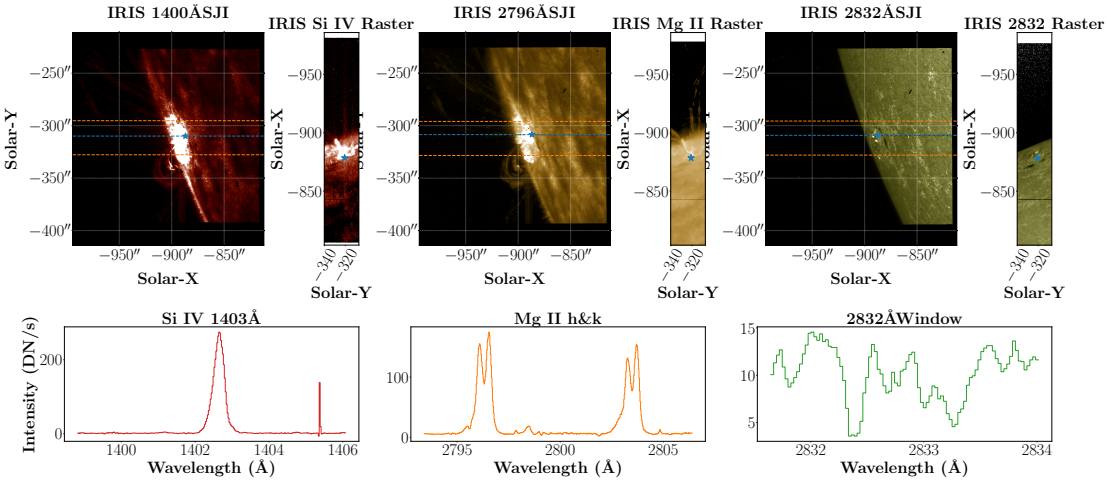


Fig. 2.3.— An example of *IRIS* data from SOL2015-06-11 in the wake of an M1.0 flare. The top row shows the slit-jaw image, with the raster extent marked in orange, and the slit position marked in blue. The corresponding raster image, summed across the spectral window is shown to the right of each slit-jaw image. The bottom row shows the raster spectrum taken from the location marked by the blue stars in the top row images.

*IRIS* (De Pontieu et al. 2014) is a slit spectrometer and accompanying slit-jaw imager, launched in 2013 as part of NASA's Small Explorer Program. The spectrograph has three channels, two FUV and one NUV channel, spanning 1331.7–

1358.4Å, 1389–1407Å, and 2782.7–2851.1Å. These spectral windows cover a variety of chromospheric and transition region lines, and provide a valuable insight into the dynamics of lower atmospheric layers, including the Mg II line complex, which contain a wealth of chromospheric diagnostics. The slit-jaw camera is operated continuously while the spacecraft is observing, with several filters available, including filters centered around the C II 1330Å, Si IV 1400Å, and Mg II k 2796Å lines.

The spectrograph is typically operated in either a rastering mode, or a "sit-and-stare" mode with a stationary slit with a width of 0.33–0.4″(depending on the spectral window), and a length of 175Å. While the strongest lines observed with the *IRIS* instrument are either optically thick, or have the potential to become optically thick during flare events, they nevertheless provide valuable velocity diagnostics in the lower solar atmosphere. Even the optically thick and complex Mg II h&k line pair can be used to derive velocity gradients via bisector analysis (discussed further in Chapter 4).

## 2.4. The Solar Dynamics Observatory (SDO) Atmospheric Imaging Assembly (AIA)

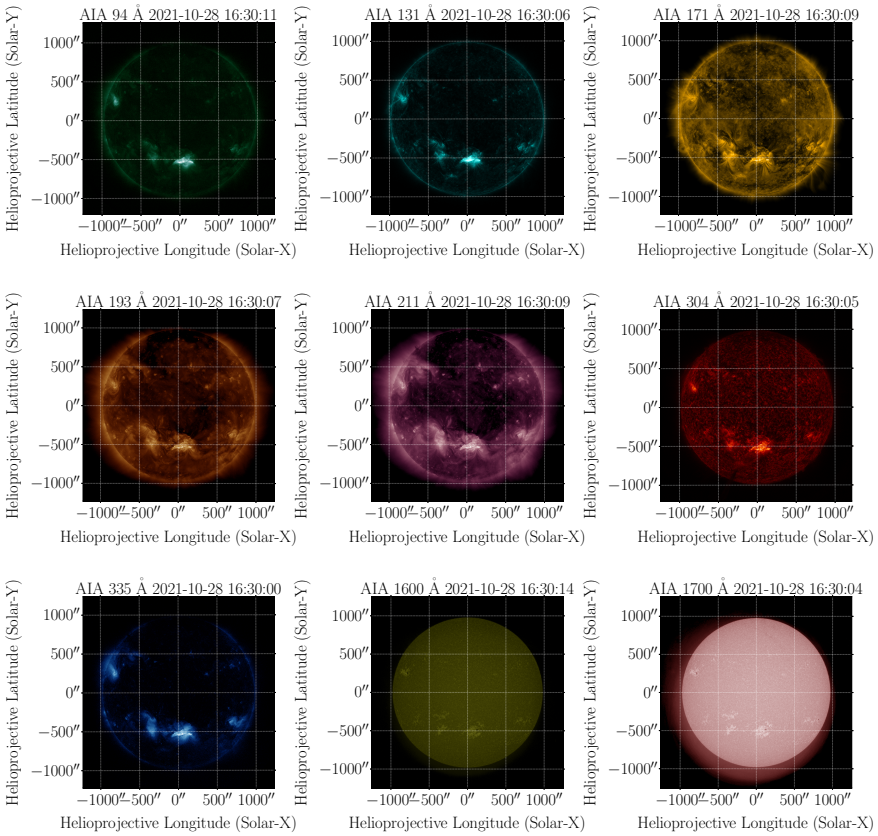


Fig. 2.4.— Example of *AIA* filtergrams for all UV channels. Data were obtained during an X1 flare on SOL2021-10-28.

SDO launched in 2011 carrying as one of its primary instruments, the *AIA* array (Lemen et al. 2012). *AIA* provides near-continuous full-disk solar observations in EUV and FUV bands, with a cadence of 12 seconds for EUV images, and

24 seconds for the 1600 & 1700Å FUV channels. The 4096×4096 images have a spatial resolution of 0.6″. In addition to the valuable time information contained in *AIA* images, the instrument also provides a convenient full-disk reference for use in the alignment of other instruments.

## 2.5. The Dunn Solar Telescope (DST)

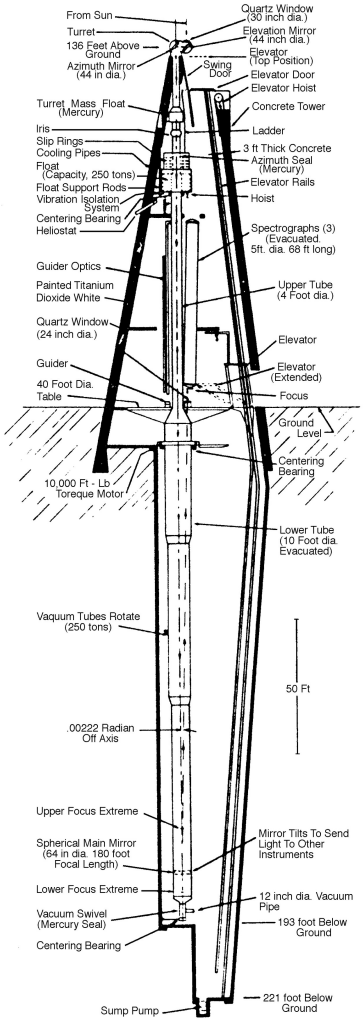


Fig. 2.5.— Cutaway schematic diagram of the Dunn Solar Telescope showing the light path from the entrance window (top) to the primary mirror (bottom) and instrument table (middle). Image courtesy of NSF NOIRLab, NSO/AURA.

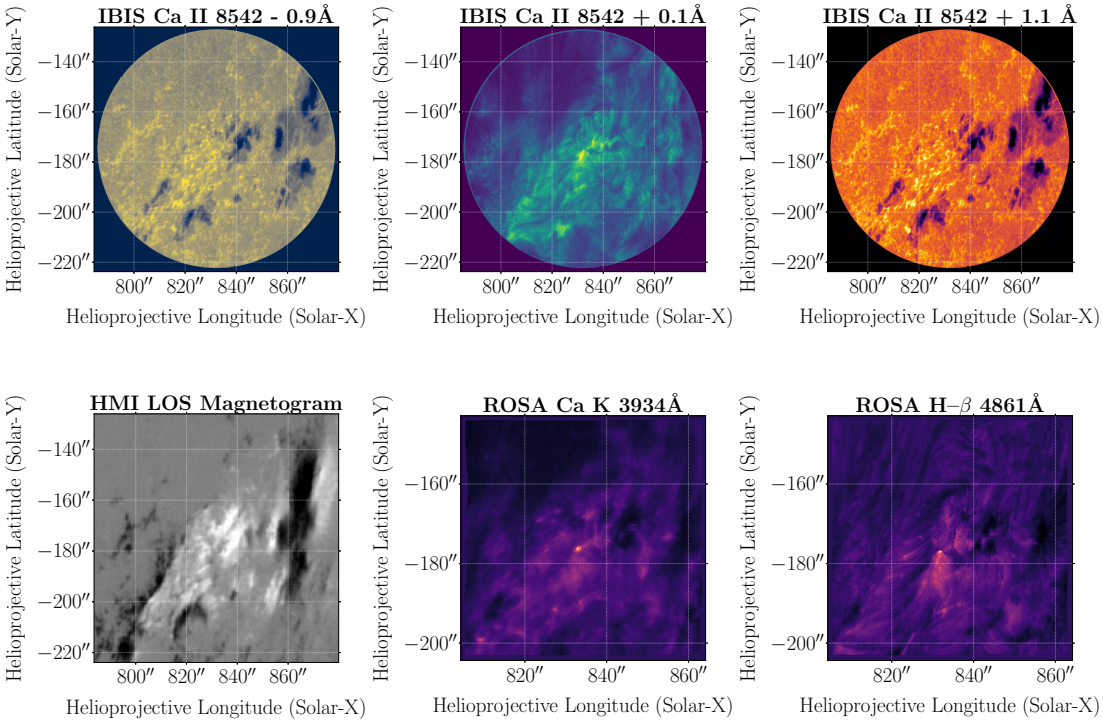


Fig. 2.6.— An example of *IBIS* and *ROSA* images obtained at the Dunn Solar Telescope on SOL2013-10-17. A cotemporal HMI magnetogram is shown for context.

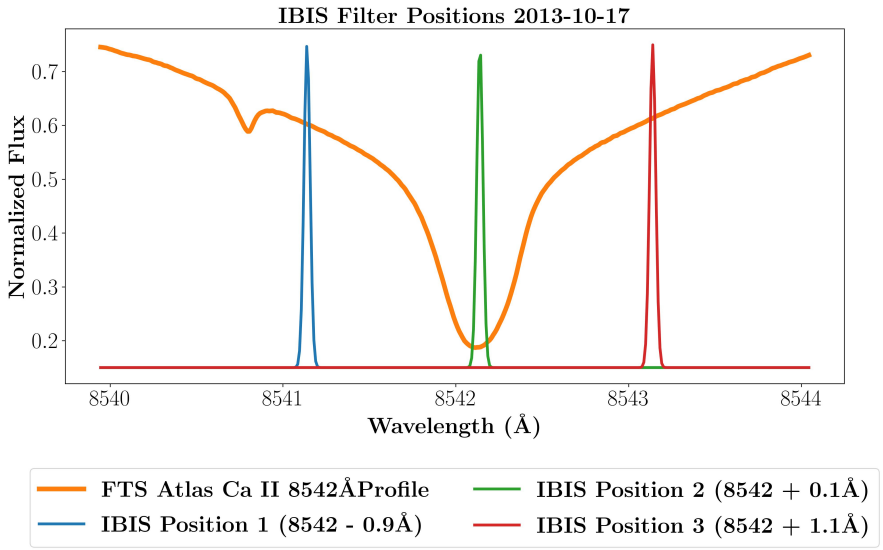


Fig. 2.7.— The Fabry-Pérot modulation scheme used to obtain the *IBIS* images shown above.

The Dunn Solar Telescope was initially proposed by Richard B. Dunn in 1965, and built from 1966–1969, as a solution to several persistent issues that have plagued ground-based solar astronomy since its inception:

- The massive amount of light being focused requires very high focal ratio, particularly in the era prior to extremely high cadence CCD and sCMOS arrays, and active cooling. This can be accomplished by either having a small entrance window, a small mirror, or a long focal length. In order to produce high-resolution images of the solar atmosphere, a larger aperture or mirror must be used, which necessitates a long focal length. The solar towers used by Hale on Mt. Wilson had 18 and 46 meter focal lengths.

- During the day, the ground turbulence layer is significant, particularly in southern New Mexico. Situating some or all of the optics high above the ground can mitigate this effect, however,

- Placing the primary mirror atop the tower causes difficulties keeping the mirror at an equilibrium with the surrounding air, resulting in yet another site of turbulence, and,

- Due to the requirement of a long focal length, this creates a large column of air, and therefore turbulence, between the tower optics and the ground (or below ground)-level optics.

- The rotation of the Earth causes the Sun, and every other astronomical object, to rotate as they move across the sky. De-rotation must be carried out at some level. The preferred method is to rotate the telescope and all of the detectors in use.

The solution Dunn settled upon was novel, to say the least. The 1.5 meter primary mirror was to be placed underground for temperature stability, near the bottom of a 60 meter pit. Solar tracking was to be carried out by flat mirrors at the top of a 40 meter tower, and the instruments were to be placed at ground level. Everything between the 76 cm entrance window atop the tower to the primary mirror was enclosed, and brought to a low vacuum. The resultant system has an effective focal ratio of approximately $f/72$. The entire enclosed section, along with a 10 meter observing table was to be suspended from a mercury float bearing in order to carry out image de-rotation. The addition of a modern adaptive optics system in 2011 resulted in a system that is remarkably flexible and stable to an extent that even other modern telescopes have difficulties matching.

While the instrumentation of the telescope has gone through numerous iterations over its half-century of operations, during the period of 2013–2014, the telescope was operating the Facility InfraRed Spectropolarimeter (*FIRS*, Jaeggli et al. 2010), the Rapid Oscillations in the Solar Atmosphere (*ROSA*, Jess et al. 2010) instrument, and the Interferometric BI-dimensional Spectro-polarimeter (*IBIS*, Cavallini 2006). A brief description of the *ROSA* and *IBIS* instruments are given below. The FIRS instrument was not used for this work.

### *2.5.1. ROSA*

The *ROSA* instrument is a high-cadence array of detectors, synchronized through a trigger unit to ensure all detectors in the array begin observing at the same time. During the time period studied, *ROSA* typically operated at cadences as high as 33 frames per second (fps), however, certain filters required much

lower cadences. In particular, when the Universal Birefringent Filter (UBF) was used, cadences as low as 8 fps were used to compensate for the comparatively low throughput.

The *ROSA* reduction process requires two nonstandard steps: speckle burst reconstruction and destretch correction. Speckle burst reconstructions are carried out using the triple-correlation application of the KISIP code (Wöger & von der Lühe 2007, 2008) in order to correct for residual seeing effects. This step further reduces the cadence of the final data set, as many images are combined to form a single specklegram. The destretch algorithm is a first-order kernel-based seeing correction that additionally corrects for artifacts introduced in the speckle reconstruction step.

### *2.5.2. IBIS*

The *IBIS* instrument was a dual Fabry-Pérot interferometer, with a filter wheel situated between the etalons as a method of rejecting unwanted orders. The resultant data set is a series of extremely narrow-band ($\approx$ 40 mÅ FWHM) images scanned across a spectral line. There is a time component to each spectral scan, however, the time required to change the filter tuning is small. The maximum cadence for a single scan used in this work is approximately 2.5 fps. The behaviour of the instrument was well-characterized by Reardon & Cavallini (2008) and Righini et al. (2010). For the purposes of this study, no polarimetric data are used, and no speckle reconstructions are carried out in order to preserve the high cadence of the instrument.

# 3. PHYSICS OF SOLAR FLARES

Solar flares are explosive phenomena that generate energy through the slow buildup and rapid release of magnetic energy, and propagate that energy through an atmosphere populated by magnetized plasma. With energy releases of up to $10^{32}$ erg, and a duration that can range from seconds to hours, the emission signature of flares is quite capable of spanning the electromagnetic spectrum as well as the solar atmosphere. More extreme events are capable of prompting a response from the photosphere in the form of white-light brightening. Recent studies, such as Kuhar et al. (2016) indicate that energies above 50 keV are key in producing white-light events.

While the most easily-observed signatures of solar flares are found in the chromosphere (notably in the H$\alpha$ ribbons accompanying an event), the initial liberation of magnetic energy is a coronal phenomenon, with energy transported from the corona both inward and outward. In this chapter, we focus on the physics underlying the observations used throughout this work. A basic overview of magnetic reconnection as the cause of solar flares is provided in Chapter 3.1, the injection of energy via nonthermal particle acceleration is discussed in Chapter 3.2, and the particulars of the chromospheric response are discussed in Chapter 3.3.

## 3.1. Magnetic Reconnection as the Flare Driver

Barely a decade after Zeeman (1897) remarked upon the broadening of sodium spectral lines in the presence of a magnetic field, sunspots were confirmed to exhibit magnetic fields of kilogauss strength (Hale 1908). Remarkably, his measured

magnetic field strength ($\approx$ 2.6 kG) is consistent with modern measurements of large sunspots, and he even (correctly) predicted that the strength of this field drops rapidly in higher atmospheric layers. Hale's remarkable observations and analysis built, in the span of 33 pages, the foundations for more than a century of solar observations.

Subsequent observations further codified the magnitude of energy that could be stored within the solar magnetic field. The total energy stored by a typical sunspot with a field strength $B$ and size $L$ is

$$E_{mag} \simeq L^3 \frac{B^2}{8\pi} \tag{3.1}$$

With typical kilogauss fields, sunspot length scales measured in tens of megameters, and lifetimes of days, magnetism provides a well for the generation and storage of energy sufficient to power a flare, although the bulk of the energy is distributed throughout the potential field (Shibata & Magara 2011).

The conversion of magnetic energy stored within a current sheet above a sunspot group into kinetic and thermal energy is carried out through magnetic reconnection. Magnetic reconnection is fundamentally the consequence of Ohmic dissipation. Dissipation drives the loss of energy in the magnetic field, which creates a strong convective electric field, leading to the acceleration of charged particles. Early proposals (Hoyle 1949; Giovanelli 1947) to explain the contribution of the magnetic field were stymied by problems of the time scale for diffusion in the corona (Cowling 1953).

$$t_{diff} \simeq \frac{\Delta^2}{\eta} \tag{3.2}$$

Where $\Delta$ is the characteristic length scale. In a plasma, the magnetic diffusivity, $\eta$

$$\eta \propto \frac{v_c}{n_e} \tag{3.3}$$

where $v_c$ is the collision frequency. This can be simplified and expressed as a function of temperature:

$$\frac{1}{\eta} \simeq 10^7 T^{\frac{3}{2}} \tag{3.4}$$

For semi-realistic values of the length and temperatures found in the corona, diffusive timescales are on the order of $10^{11-12}$ s. From the other direction, the timescales associated with flares yield spatial scales as small as $10^3$ cm, which is far too small to contain the requisite energies.

The Sweet-Parker model (Sweet 1958; Parker 1957) took steps to reconcile this disparity by introducing plasma flow, but were unable to fully realize the timescales required for observations of typical flares. A better model was proposed by Petschek (1964), in which slow, standing, magnetohydrodynamic shocks are introduced. The resultant reconnection rate and timescale can be best expressed by the Alfvén mach number, a non-dimensional flow velocity expressed as

$$M_o = \frac{v_i}{V_A} \tag{3.5}$$

Where $v_i$ is the inflow speed of the plasma, and $V_A$ is the Alfvén velocity measured in the inflow region

$$V_A = \frac{B_i}{\sqrt{4\pi\rho}} \tag{3.6}$$

which depends on the magnetic field, $B_i$, and plasma density, $\rho$.

Petschek's remarkable insight yields a simple relation for the non-dimensional

flow velocity that depends only on the inverse logarithm of the magnetic Reynolds number, ($R_m \propto \frac{v_i \Delta}{\eta}$, where $\Delta$ is a characteristic length scale)

$$M_{o,max}^2 = \frac{\pi}{4 \ln 2 M_{o,max}^2 R_m} \tag{3.7}$$

For the corona, the typical value for $M_{o,max}$ ranges between 0.01–0.1 (Petschek 1964). If we define the reconnection time within a current sheet of length $L$ to be

$$t_{rec} = \frac{L}{V_A M_o} \tag{3.8}$$

Observations show the scale of typical coronal magnetic structures to be between $10^4$–$10^5$ cm. The resultant timescale is $10^2$–$10^4$ s, comparable to the reported durations of typical flares.

The intervening sixty years has seen a variety of models attempting to apply magnetic reconnection to the phenomenology observed in solar flares. The closest approximation to a standard model explaining the dynamics and phenomena associate with a flare is the CSHKP model, named after a variety of pioneering models (Carmichael 1964; Sturrock 1966; Hirayama 1974; Kopp & Pneuman 1976). These models all assume a similar configuration of the magnetic field, and the dynamic processes leading to, and in the aftermath of, a flare. Figure 3.1 shows a modern schematic of this model from Shibata & Magara (2011); Shibata et al. (1995).

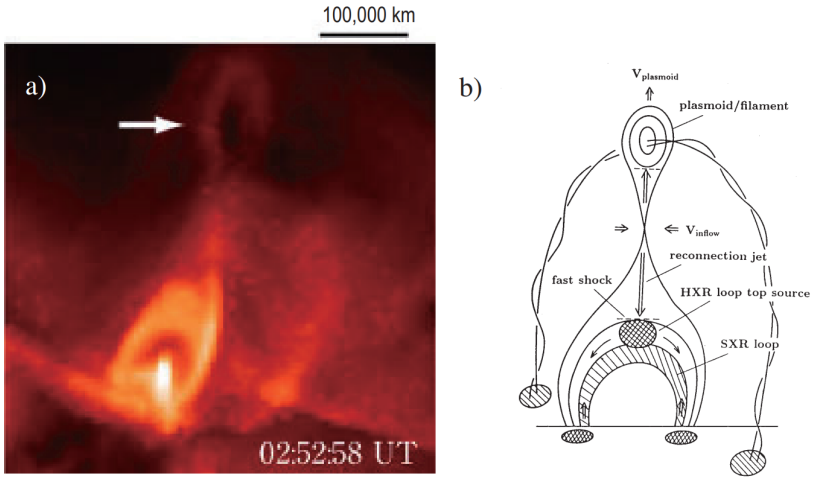


Fig. 3.1.— (a) Observed by *Yohkoh*'s SXR telescope, this event clearly shows the hallmarks of a magnetic reconnection event. (b) a schematic of the modified CSHKP model. Reproduced from Shibata et al. (1995); Shibata & Magara (2011)

### 3.2. Nonthermal Particles and Energy Deposition

In a fundamental sense, the theory of magnetic reconnection was intended to provide an explanation for accelerated particles observed in solar flares. Magnetic reconnection provides a method for creating strong electric fields that accelerate charged particles, and magnetic structures to funnel them into the lower solar atmosphere. The specific method for producing large populations of accelerated electrons is not fully understood. Many scenarios have been proposed and discussed (for a comprehensive review of acceleration scenarios, see Zharkova et al. (2011)). For this work, however, our focus is not on the method of particle acceleration, but rather the consequences thereof. So let us suffice then to say merely that, in the wake of magnetic reconnection, a population of accelerated electrons is introduced to the solar chromosphere at the base of the flare loop.

This simplification is justified in large part by the Neupert effect (Neupert 1968). Neupert noted that SXR flux during the rise phase of a solar flare corresponded to the time integral of centimeter radio flux. The same correlation was later found between SXR flux and HXR flux. It is frequently expressed as the reverse of Neupert's observation such that:

$$\frac{d}{dt}F_{SXR}(t) \propto F_{HXR}(t) \tag{3.9}$$

The broader implication of this empirical relationship (an example of which is presented in Fig. 3.2) suggests that there is a direct causal relationship between energetic electrons producing HXR flux, and the thermal plasma. The SXR emission originates from a plasma heated primarily by energy deposited through flare accelerated electrons.

HXR radiation (above ≈3 keV) is typically produced by Coulomb collisions via the bremsstrahlung process. There are exceptions, notably the 6.7 keV line from Fe XXV, the blended 8 keV Fe/Ni line, the 511 keV positron annihilation line, and the 2.22 MeV neutron capture line. In general, however, when discussing HXR emission, the mechanism is the bremsstrahlung process, a form of free-free radiation. In solar flare HXR spectra, a mix of thermal and nonthermal bremsstrahlung is observed. Thermal bremsstrahlung assumes an initial population of electrons with a Maxwellian distribution. This contribution dominates at temperatures below ≈15 keV. The electron population produced by magnetic reconnection, however, is distinctly non-Maxwellian, and is typically represented by a power law distribution of electron energies. In general, the observed HXR

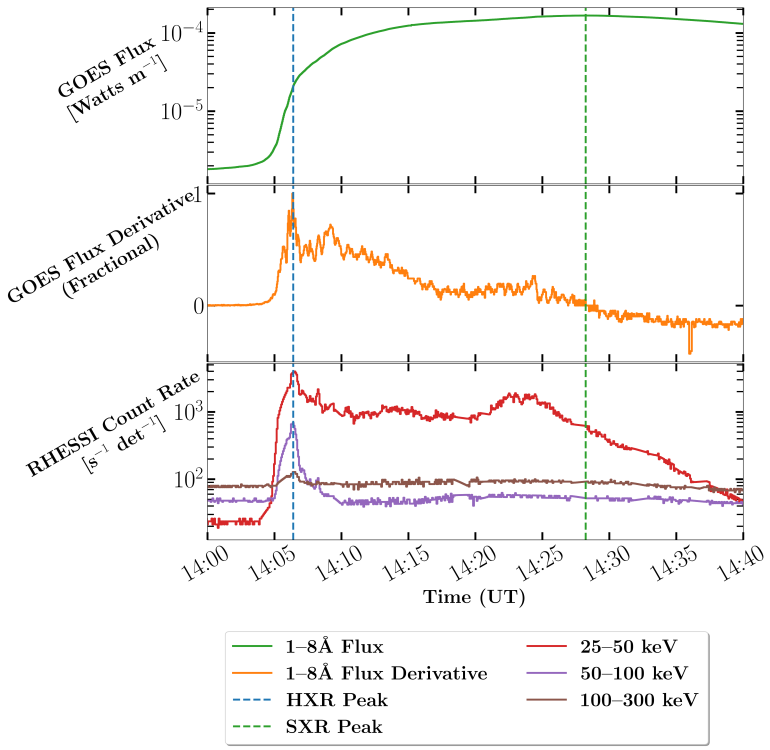


Fig. 3.2.— Observational Demonstration of the Neupert effect during an X1.6 flare on SOL2014-10-22. **Top:** SXR Flux in the GOES 1–8
AA band. **Middle:** Derivative of SXR flux. **Bottom:** HXR emission in three *RHESSI* bands, 25–50 keV, 50–100 keV, and 100–300 keV.

spectrum can be formulated as

$$I(\epsilon) = \frac{1}{4\pi R^2} \int_{\epsilon}^{\infty} Q(\epsilon, E) \langle nVF(E) \rangle dE \tag{3.10}$$

where $\epsilon$ is the photon energy (in keV), $E$ is the electron kinetic energy, $Q(\epsilon, E)$ is the bremsstrahlung cross section from Bethe-Heitler formalism, and the quantity $\langle nVF(E) \rangle$ is the density-weighted mean electron flux spectrum, integrated over the flaring region (Brown et al. 2003; Kontar et al. 2019). Here, the factor $\frac{1}{4\pi R^2}$ is a distance scale factor for the distance from the Sun to the observer. The observed spectrum is expressed as photons cm$^{-2}$ s$^{-1}$ keV$^{-1}$. The eventual goal is to find the injected electron spectrum, $\dot{N}(E_0)$, from the mean electron flux spectrum, $\langle nVF(E) \rangle$. This requires a model of the electron dynamics in the flare. The basic model for flare electron dynamics for the past 50 years has been the collisional cold thick-target model, first proposed by Brown (1971), and further codified for practical use by Emslie (1978).

A full review of the collisional cold thick-target model is outside the scope of this chapter. The major assumption of this model is that an electron incident to the "target" will lose all of its kinetic energy in Coulomb collisions with a population of electrons that have a far lower energy than the incident population. The electron energy loss rate then is

$$\frac{dE}{dt} = -\frac{2\pi e^4 n_e v_e \ln \Lambda}{E} \tag{3.11}$$

where $\ln \Lambda$ is the Coulomb logarithm, $n_e$ is the ambient density, $v_e$ is the electron velocity, and $e$ is the electron charge. Given that, observationally, $I(\epsilon) \propto \epsilon^{-\gamma}$, the accelerated electron spectrum can also be expressed as a power law (Brown 1971;

Brown et al. 2003; Holman et al. 2011):

$$\dot{N}(E) = \dot{N}_0 \frac{\delta - 1}{E_c} \left( \frac{E}{E_c} \right)^{-\delta} \tag{3.12}$$

where $\delta = \gamma + 1$ ($\gamma$ being the index of the power law describing the intensity), $E_c$ is the low-energy cutoff to the injected electron spectrum, and $\dot{N}_0 = \int_{E_c}^{\infty} \dot{N}(E_0) dE_0$ ($s^{-1}$), the total rate of electron acceleration. From this, the total power $P$ (keV $s^{-1}$) can be computed from the integral of $N$ to be

$$P = \frac{1}{\delta - 2} E_c^{2-\delta} \left[ \dot{N}(E_c) E_c^{\delta} \right] \tag{3.13}$$

For a given accelerated spectrum, $P$ is then strongly dependant on the value for the low-energy cutoff $E_c$. Figure 3.3 shows example spectra from *RHESSI* of typical HXR spectra found in large flares. As these spectra are combinations of lower-energy thermal, and higher-energy nonthermal bremsstrahlung radiation, the measurement of the low-energy cutoff is difficult, but not impossible, as we will show in Chapter 4.

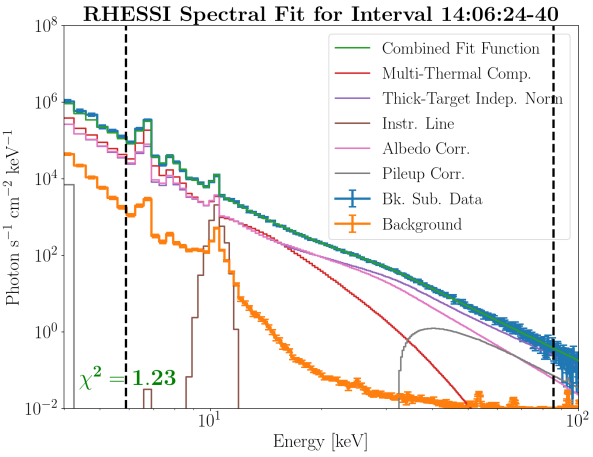


Fig. 3.3.— *RHESSI* photon spectrum from an X1.6 flare on SOL2022-10-22. The difference between the thermal and nonthermal HXR spectrum is clearly visible, even when accounting for instrumental effects.

## 3.3. Chromospheric Response

### *3.3.1. Chromospheric Evaporation*

The response of the chromosphere to the injection of energy via nonthermal particles is multifarious, and many aspects of the chromospheric response to energy injection are poorly or barely understood. In this section, we will focus on the particulars of the chromospheric response nonthermal energy injection, including the evaporation of plasma into the corona, the ionization of the lower chromosphere, and the global oscillations of chromospheric plasma.

Chromospheric evaporation is thought to be a direct result of energetic particle precipitation into a dense plasma. The energy produced by the electron beam via Coulomb collisions causes a dynamic response in the plasma.

When the energy input to the chromosphere exceeds that which can be shed as radiation or conductive losses, the chromospheric plasma must heat and expand upward, into the lower-density corona. This process fills overlying magnetic structures of lower density with high-temperature plasma, which strongly emits extreme ultra-violet (EUV) and soft X-ray (SXR) emission. This chromospheric evaporation (Neupert 1968; Bornmann 1999; Fletcher et al. 2011) can occur explosively, with high-temperature lines exhibiting blueshifts, while cooler emission lines exhibit redshifts (Doschek 1983; Brosius & Phillips 2004; Milligan & Dennis 2009); or gently, with blueshifted emission lines across a wide temperature range (Fisher et al. 1985; Brosius & Phillips 2004; Allred et al. 2005; Milligan et al. 2006; Brosius & Daw 2015). The mode of evaporation is dependant first on the mechanism of flare energy transport. In the case of energy transport by a nonthermal electron driver, the mode of evaporation is further dependant on the energy flux, low energy cutoff, and population distribution of accelerated electrons reaching the chromospheric footpoints.

Canfield & Gayley (1987) and Fisher et al. (1985) first deduced this effect and placed a lower limit on the requisite energy flux density required to drive explosive evaporation of $E_{e^-} \geq 3 \times 10^{10}$ erg cm$^{-2}$ s$^{-1}$. If the incoming electron flux is above this threshold, determined by balancing the heating rate and the hydrodynamic expansion timescale, the over-pressure of the hot rising material causes the denser layers below to recoil, resulting in the cool, redshifted emission characteristic to explosive evaporation.

Thermal conduction-driven chromospheric evaporation, in contrast, does not appear to be subject to above restrictions on flux deposition. Longcope (2014) found that even the smallest energy fluxes studied produced explosive chromo-

spheric evaporation. This result was also noted in earlier models from Fisher (1989).

In addition to the Doppler velocity signatures of chromospheric evaporation, excess nonthermal width in optically thin spectral lines has been observed in flare conditions. One possible explanation is the superposition of unresolved flows. In this case, the nonthermal width is a measure of the velocity distribution of the plasma (Doschek et al. 2008). Newton et al. (1995) attempted to generalize both excess line widths and blue wing enhancements by the computation of a Velocity Differential Emission Measure (VDEM), which treats the observed line profile as a continuum of Gaussian components driven by variations in the line-of-sight velocity. This treatment is supported by reported correlations between Doppler velocities and nonthermal velocities within solar active regions (Hara et al. 2008; Doschek et al. 2008; Bryans et al. 2010; Peter 2010). Another possible explanation for excess line widths is the influence of pressure or opacity broadening in regions of enhanced electron density. Milligan (2011) showed a correlation between electron density and nonthermal velocity broadening, although neither pressure broadening nor opacity effects were able to account for any significant portion of the excess width.

The flare-driven mass flow rate into the solar corona remains one of the more difficult solar flare metrics to disentangle from observations, requiring both accurate velocity information, and a measure of plasma mass. As a proxy, the electron density of the active region can be used (Milligan et al. 2005; Doschek et al. 2008). Density enhancements have been observed to be cospatial with the locations of flare footpoints (Graham et al. 2011). Densities, when combined with the emission measure (Del Zanna et al. 2011), may also provide information

about the dynamics of the evaporating region. The previously mentioned VDEM (Newton et al. 1995) is derived in part from the electron density, and provides direct insight into plasma transport during a solar flare.

### *3.3.2. Lower Chromospheric Response*

While evaporation tends to affect the upper layer of the chromosphere, lower layers also exhibit a pronounced response to a nonthermal injection event. By far the most noticeable is the significant enhancement in the H$\alpha$ line, to the extent that historically, flares were considered to be purely chromospheric phenomena. In the H$\alpha$ core, the global or regional lightcurves peak well after the HXR event peak, however, initial intensity enhancements nearly simultaneous with HXR bursts are well-established (Canfield et al. 1984; Canfield & Gayley 1987; Fisher et al. 1985; Hawley & Fisher 1994; Abbett & Hawley 1999). In the wing of H$\alpha$, this effect is particularly pronounced, with Stark broadening (Stark 1913) producing deep chromospheric emission (Svestka 1976; Canfield & Gayley 1987; Wuelser & Marti 1989).

Small-scale emission enhancements in the wings of chromospheric lines date back to the earliest days of solar astronomy (Ellerman 1917). When observed in H$\alpha$ and Ca II 8542Å, they are typically termed "Ellerman Bombs". They are likely related (Ortiz et al. 2020) to phenomena such as "*IRIS* bursts" (Peter et al. 2014), or Solar Orbiter "campfires" (Berghmans et al. 2021). Numerous studies of Ellerman bombs have been carried out, notably by Watanabe et al. (2011); Vissers et al. (2013), and Vissers et al. (2015). These studies tracked morphological, temporal, and intensity differences between wavelength regimes,

and found these events to be the signature of magnetic reconnection occurring at near-photospheric altitudes.

Wang et al. (2000) observed the blue wing of H$\alpha$ and found that, on sub-second timescales, certain Ellerman-like events were correlated to the production of HXR emission. This observation provides a clue as to the production, generation, and deposition of flare energy. Another clue as to the nature of H$\alpha$ wing emission was provided by McAteer et al. (2005), who found quasi-periodic pulsations in the flare ribbon lightcurve. These oscillations were not present in the region prior to the flare, and have periodicities differing from known chromospheric oscillations, such as the ubiquitous 3-minute oscillations, which are thought to be fundamentally chromospheric in origin (Milligan et al. 2017; Farris & McAteer 2020). Radziszewski et al. (2011) studied H$\alpha$ observations for a series of flares, attempting to codify the time delays found in certain flare kernels with respect to HXR emission, and found that kernels with the shortest delays exhibited remarkable correlations to the HXR emission. The implications of these observations are far-reaching. If the generation of HXR emission can be tracked to these small scale structures, then the fundamental scale of the energy injection region may be orders of magnitude smaller than typically assumed. These observations also provide valuable evidence of episodic or periodic injection of nonthermal electrons, with broad implications for models of magnetic reconnection.

# 4. CALL AND RESPONSE: TRACKING THE CHROMOSPHERIC RESPONSE TO A NONTHERMAL ENERGY INJECTION

## 4.1. Introduction

The flare chosen for the subject of this study, an X-class flare on 22 October, 2014[1], is a well studied event. Bamba et al. (2017) studied the precursor conditions to this event in order to determine triggering conditions in the chromosphere and photospheric magnetic field. Veronig & Polanec (2015) attempted to quantify the magnetic reconnection flux and rate. Li et al. (2015) utilized data from *IRIS* and *RHESSI* instruments to study Doppler velocities in Fe XXI and C I, and HXR intensities. Thalmann et al. (2015) focused on the rate of magnetic reconnection. Lee et al. (2017) measured electron flux at each HXR peak using *RHESSI*, and linked the electron energy budget with observed low chromospheric and photospheric energetic response. These studies showed that energy was injected via high-energy electrons, which was sufficient to produce white-light emission.

In this study, detailed, time-resolved *RHESSI* HXR spectral fit parameters are presented in order to quantify the nonthermal electron energy injection profile. The profile of electron energy injection is then connected to multispectral observations of the chromospheric evaporation response. Emission line intensities, electron densities, and Doppler and nonthermal velocities from several instrumental sources were combined in order to study the response of the flaring solar atmosphere across time, space, and temperature. Due to the abundance of data available for this flare, this event is ideally-suited to constrain detailed

[1]A context movie for this flare can be found at `https://youtu.be/9DGCLvuPouY`

hydrodynamic modeling of energy transport.

## 4.2. Data Description and Processing Methods

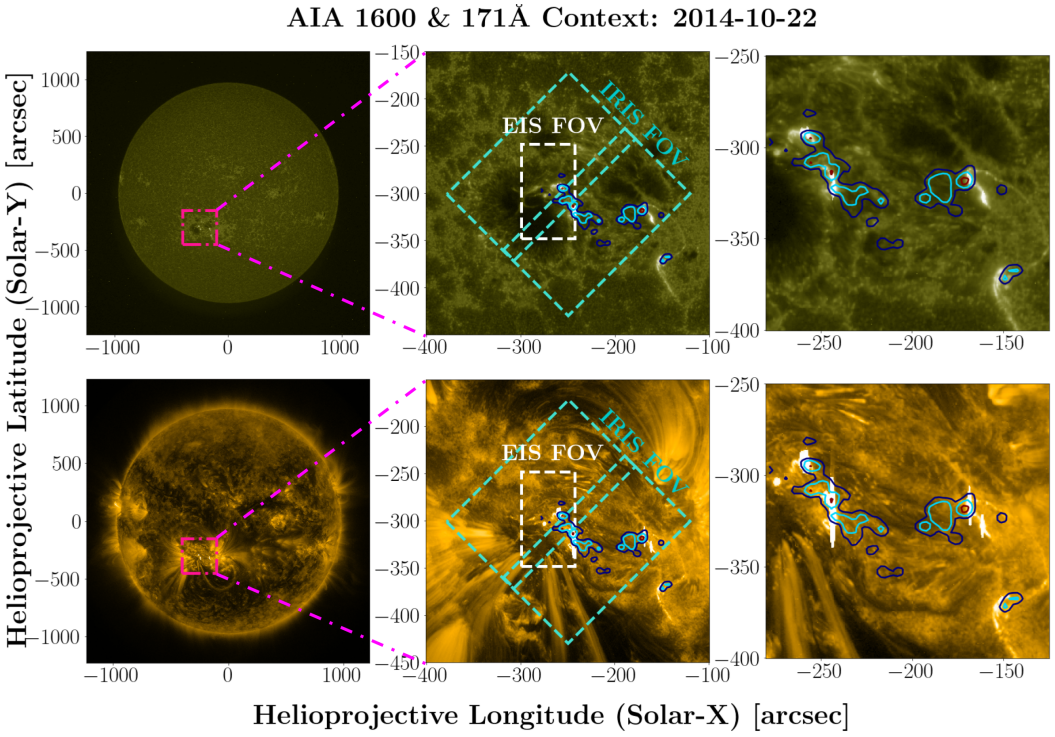


Fig. 4.1.— **Left:** Full-disk solar filtergrams on 2014 October 22 from *AIA* 1600Å (top) and 171Å (bottom) bands. **Middle:** Image of NOAA 12192 during the X1.6 flare with *RHESSI* 40–100 keV 20%, 40%, and 60% contours (multiple colors), *IRIS* slit-jaw imager and slit field of view (FOV) (cyan), and *EIS* raster (white). **Right:** Detail of NOAA 12192 to highlight correlation between *AIA* intensity enhancements and *RHESSI* HXR footpoints.

The X1.6 flare selected for study occurred on 2014 October 22, beginning at 14:02:00 UT, and was one of the largest flares produced by flare-productive NOAA AR 12192. In Figure 4.1 the active region is presented in the 1600Å and

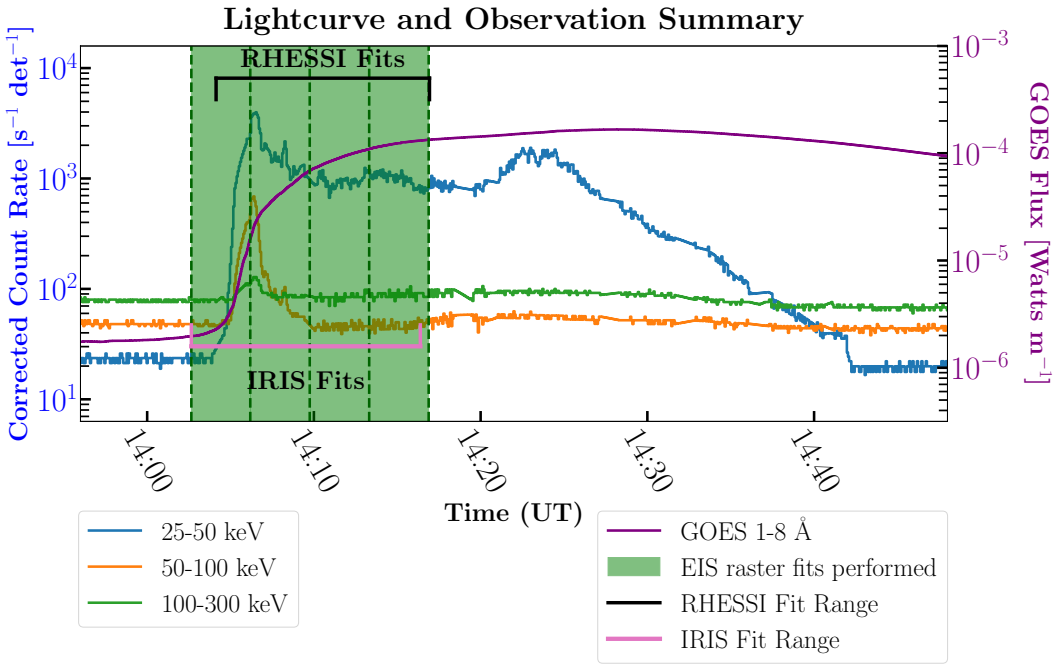


Fig. 4.2.— Lightcurves for *GOES* (purple line) and *RHESSI* (blue, orange, and green lines), with *EIS* raster times overlaid (translucent green blocks), as well as the interval in which *RHESSI* fits are performed (solid black line), and *IRIS* fits are performed (solid pink line).

171Å passbands of *AIA*, with the fields of view of the *EIS* and *IRIS* instruments overlaid, and with HXR contours from *RHESSI* imaging superimposed to highlight the primary footpoints of the flare. Two HXR sources are well-defined and are cospatial with intensity enhancements in *AIA* images. A third, compact HXR kernel appears to the southwest of the primary flare loop, corresponding to a possible tertiary footpoint, or merely an extension of the large western footpoint. Figure 4.2 shows the *RHESSI* HXR lightcurves in three energy bands (25–50, 50–100, and 100–300 keV) as well as SXR emission from the GOES 1-8Å band. Figure 4.2 provides additional context, with the time intervals where *EIS*, *IRIS* and *RHESSI* spectral fits were performed.

The GOES flux for this event plateaus through much of the event, with a SXR peak found well after the peak of HXR emission (14:28 UT, versus 14:06 UT). Hereafter, when the peak of the flare is referred to, it is in reference to the peak of HXR emission.

### *4.2.1. RHESSI Analysis*

The full duration of this flare was well-covered by the *RHESSI* instrument. *RHESSI* entered its daylight phase just prior to the onset of the flare, and exited during the gradual phase, after the *RHESSI* HXR peak and the GOES SXR peak. As of August 2014, the *RHESSI* spacecraft had undergone its fourth successful anneal, allowing five of the original nine detectors to regain high spectral resolution.

*RHESSI* spectra from 14:04:40 – 14:16:56 UT were obtained with 16 second time bins for detectors 1, 3, 6, 8, and 9, which had consistently high count rates

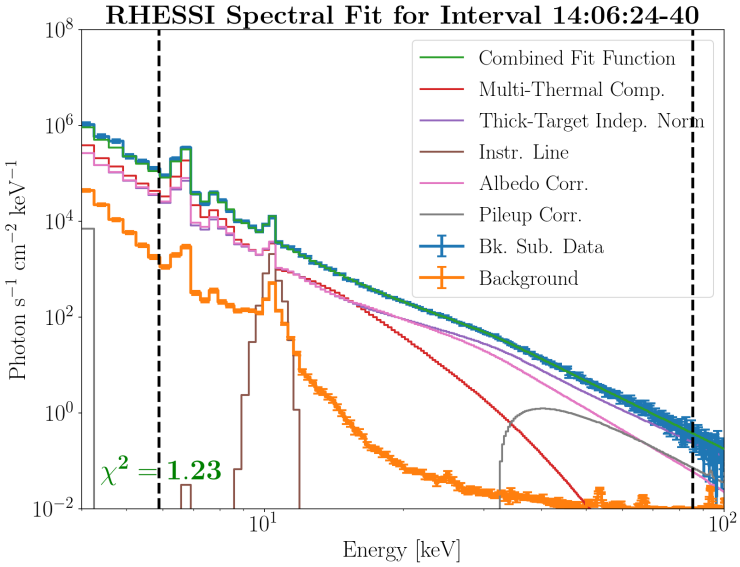


Fig. 4.3.— Example spectral fit from *RHESSI* detector 6. The time range shown had the highest integrated count level within the dataset, spanning 14:06:24–14:06:40 UT. A strong nonthermal component dominates energies above $\approx 15$ keV. The heavy black dashed line denotes the fit energy range.

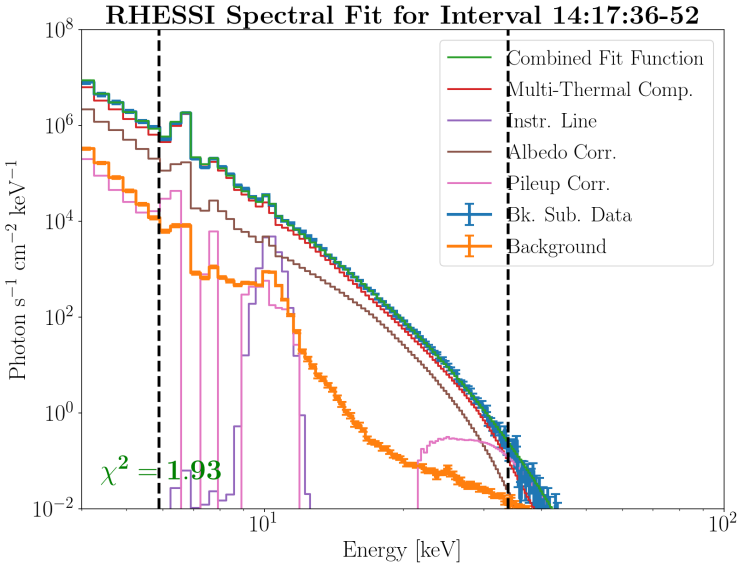


Fig. 4.4.— Example spectral fit from *RHESSI* detector 6. The time range shown is after the cessation of nonthermal energy injection, spanning 14:17:36–14:17:52 UT. The heavy black dashed line denotes the fit energy range, but the bounds of the plot are scaled to match Figure 4.3.

during the flare, signifying that they retained sufficient sensitivity to be usable. From the peak counts, detector 6 was determined to be the most sensitive, while detector 1 was the least, leading to different fit results and higher values of $\chi^2$ for detector 1. Background characterization and spectral fitting were performed for each individual detector using the `OSPEX` package in *SolarSoftWare* (SSW). For each detector, the background profile was determined by using the smoothed emission profile of the 100–300 keV energy band in the same detector. Save for one brief ($< 32$s) spike during the impulsive phase of the flare, emission in this energy range showed only a slow variation throughout the *RHESSI* orbital cycle. This time-varying profile was used as a template for the background in lower energy bands. The count rate during *RHESSI*'s night was used to determine the relative scaling between energy bands, and served as anchor points for application of the template.

Spectra were fit using a methodology similar to that adopted by Milligan et al. (2014). The thermal portion of the *RHESSI* spectrum was best fit by a multithermal model, similar to studies by Aschwanden (2007), Battaglia et al. (2015), and Choithani et al. (2018). The multithermal model selected was characterized by a power-law differential emission measure (DEM) between a fixed minimum plasma temperature (0.5 keV) and a variable maximum plasma temperature. The nonthermal portion of the *RHESSI* spectrum was best fit by a thick-target electron beam model, with an electron distribution characterized by a single power-law. Additional instrumental effects were accounted for by modifying the detector response matrix (`drm_mod`), accounting for instrumental pileup (`pileup_mod`), albedo, and incorporating an additional Gaussian component to account for the 10 keV instrumental line (Phillips et al. 2006).

Sample spectra are shown in Figures 4.3 and 4.4, along with the combined fit functions used to characterize the HXR profile for a time interval with a significant nonthermal component (Figure 4.3) and a time interval without (Figure 4.4). Note that while spectra in these figures are shown in units of photons $s^{-1}$ $cm^{-2}$ $keV^{-1}$, spectral fitting was carried out in count space. The use of the calculated photon spectrum exaggerates several notable features, such as the 10 keV instrumental line first characterized by Phillips et al. (2006). Summaries of major parameters obtained via *RHESSI* spectral fitting are discussed in Section 4.3.1.

We also make use of the unique imaging capabilities of *RHESSI* in order to identify the flare footpoints. The `CLEAN` algorithm was applied to detectors 1, 3, 6, 8, and 9 during the impulsive and peak phases of the flare to identify sources of HXR emission throughout the flare duration. Contours of these images are overlaid on the center and right–hand columns of Figure 4.1 to provide context for other observations and constrain the locations of HXR emission during the peak of the flare.

### *4.2.2. EIS Analysis*

Using the 2″ slit, the *EIS* instrument performed rasters of NOAA AR 12192, capturing the pre-flare, impulsive, peak, and gradual phases of the solar flare centered around the eastern flare footpoint, as identified by *RHESSI* HXR imaging. The rasters had a cadence of 214 seconds, covering a field of view (FOV) approximately 60″ × 152″, as shown in Figure 4.1. The spatial resolution of the *EIS* instrument is 3″ in the horizontal, 1″ in the vertical, with a spectral resolution of 22.3 mÅ. During this event, the footpoint was captured in several emission lines

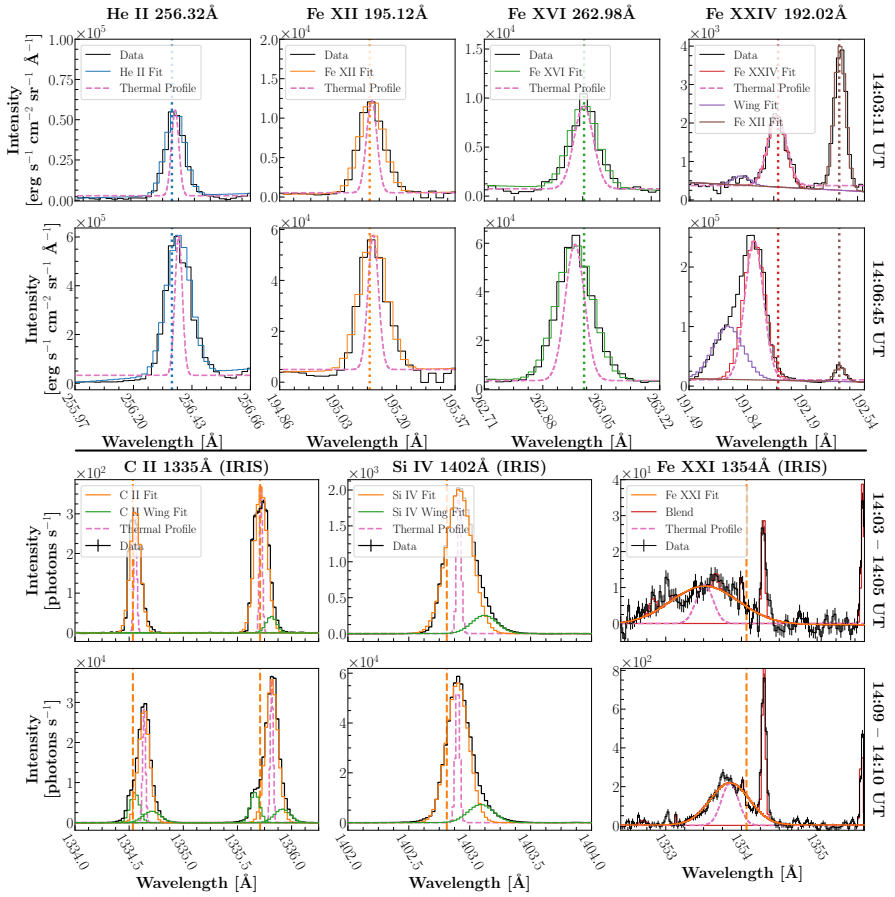


Fig. 4.5.— Example spectral fits from the *EIS* and *IRIS* instruments. The top two rows show fits from the *EIS* instrument, while the bottom two rows show fits from the *IRIS* instrument. For each instrument, the top row shows fits from a time early in the flare, while the bottom row shows fits from approximately the time of peak HXR emission. For the *EIS* instrument, spectral windows containing He II 256.35Å, Fe XII 195.12Å, Fe XVI 262.98Å, Fe XXIV 192.02Å, and Fe XII 192.39Å are shown left to right. The faint blend with Fe XII 195.12Å is not shown, as the major line dominates the window. For the *IRIS* instrument, spectral windows containing the C II 1334.54Å and 1335.71Å doublet, the Si IV 1402.81Å line, and the Fe XXI 1354.07Å line are shown left to right. In each panel, the vertical line(s) denotes the calculated rest wavelength, while the pink dashed profile shows the profile of a line with the same peak and offset, but only thermal and instrumental width, without nonthermal broadening (Equation 1).

Table 4.1: *EIS* Line Summary

| **Ion** | **Formation Temperature [MK]**[a] | **Central Wavelength [Angstrom]** |
|---|---|---|
| Fe XXIV | 18.20 | $192.026 \pm 0.003$ |
| Fe XXIV | 18.20 | $255.13 \pm 0.047$ |
| Fe XXIII | 14.13 | $263.78 \pm 0.053$ |
| Ca XVII | 6.31 | $192.845 \pm 0.008$ |
| Fe XVI | 2.51 | $263.004 \pm 0.003$ |
| Fe XV | 2.0 | $284.182 \pm 0.003$ |
| Fe XIV | 1.82 | $274.225 \pm 0.003$ |
| Fe XIV | 1.82 | $264.808 \pm 0.003$ |
| Fe XII | 1.35 | $192.391 \pm 0.003$ |
| Fe XII | 1.35 | $195.122 \pm 0.003$ |
| Fe X | 1.0 | $184.536 \pm 0.012$ |
| He II | 0.05 | $256.349 \pm 0.005$ |

[a]Assuming ionization equilibrium.

Table 4.2: *IRIS* Line Summary

| **Ion** | **Formation Temperature [MK]**[a] | **Central Wavelength [Angstrom]** |
|---|---|---|
| Fe XXI | 11.48 | $1354.067 \pm 0.04$ |
| O I[b] | N/A | $1355.599 \pm 0.04$ |
| Si IV | 0.08 | $1402.812 \pm 0.057$ |
| C II | 0.01 | $1334.543 \pm 0.026$ |
| C II | 0.01 | $1335.705 \pm 0.024$ |
| Mg IIk | 0.015–0.03 | $2796.370 \pm 0.023$ |
| Mg II Triplet 1 | 0.015–0.03 | $2791.593 \pm 7.609 \times 10^{-5}$ |

[a]Assuming ionization equilibrium.

[b]Used only for Fe XXI reference wavelength

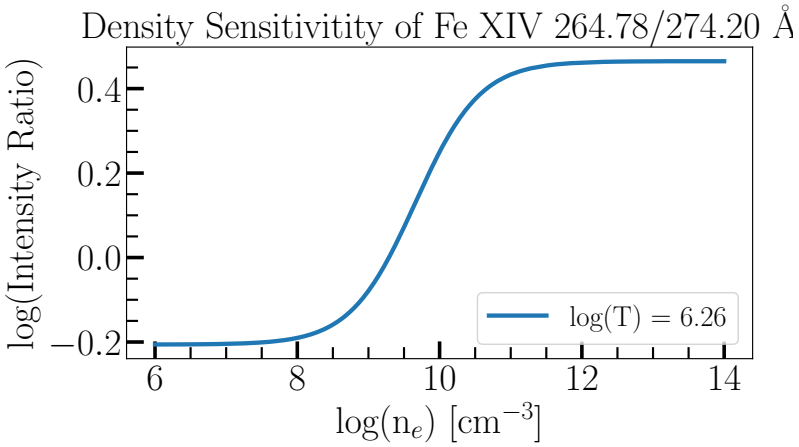


Fig. 4.6.— For Fe XIV 264.81/274.23Å the theoretical curve describing the relationship between the intensity ratio of each line, and the electron density Fe XIV. The theoretical curve is formed from the CHIANTI 10.0 atomic database (Dere et al. 1997; Dere et al. 2019).

in the raster FOV; the observed emission lines are detailed in Tables 4.1 and 4.2, which also includes information on emission lines from the *IRIS* instrument. Gaussian fits were performed for a set of twelve emission lines from nine different ions. While most of the ions studied required only single-component fits, multiple component fits were performed in order to examine the effects of blended lines. The He II 256.35Å, Fe XIV 272.20Å, Fe XV 284.18Å, and Ca XVII 192.83Å lines required two or more Gaussian profiles to account for known line blends (Young et al. 2007). Even in these spectral windows, the presence of strong blended lines was not consistent over each raster, or at each time. Additionally, the Fe XXIII 263.78Å, Fe XXIV 255.13Å, and Fe XXIV 192.02Å lines required multiple components to account for both blends and a blue-wing enhancement (Milligan & Dennis 2009).

The spectral fits were used to determine Doppler velocities, nonthermal ve-

locities, electron densities, and intensities as functions of both temperature and time. Example fits from a selection of emission lines are shown in Figure 4.5. The profiles chosen showcase a wide temperature range, from a location within the eastern footpoint early in the flare, and during the HXR peak.

The rest wavelength for every emission line, save Fe XXIII and Fe XXIV, was determined from the mean central wavelength across the less-active raster regions. In the case of Fe XXIII and Fe XXIV, no plasma can be assumed to be at rest, and an alternate method was required. For Fe XXIV 192.02Å the Fe XII 192.39Å line was used to constrain the rest wavelength from the theoretical separation of the two lines from the CHIANTI database (Dere et al. 1997; Dere et al. 2019). For Fe XXIII and Fe XXIV 255.13Å lines, the mean central wavelength from the 14:31:12 UT raster was used, as this raster consists entirely of emission produced after the nonthermal electron injection event.

For ions with strong blue wing enhancements (Fe XXIII and Fe XXIV), the Doppler velocities presented for the blue wing were calculated with the same reference wavelength used for the line core.

Nonthermal velocities were calculated using the method described by Mariska (1992b), and utilized in several other studies (Doschek et al. 2007; Harra et al. 2009; Milligan 2011), where the most probable nonthermal velocity ($v_{nth}$) is calculated using the form:

$$W^2 = 4 \ln 2 \left(\frac{\lambda}{c}\right)^2 (v_{th}^2 + v_{nth}^2) + W_{inst}^2, \tag{4.1}$$

where W is the measured full width at half maximum of the Gaussian profile, $W_{inst}$ is the instrumental width (0.056 mÅ Doschek et al. 2007 and Harra et al. 2009).

The *EIS* dataset used in this work contains the density-sensitive line pair of Fe XIV 264.81/274.23Å. The theoretical relationship between the intensity ratio and electron density for this line pair is shown in Figure 4.6, from the CHIANTI v10.0 database (Dere et al. 1997; Dere et al. 2019). This line pair is sensitive to densities between $10^8 < n_e < 10^{12}$ cm$^{-3}$. It is important to note that the relationship between the Fe XIV intensity ratio and electron density is formed under the assumption of ionization equilibrium, which may not be valid during large dynamic events such as solar flares. The Doppler and nonthermal velocity results from *EIS* fitting are discussed in Sections 4.3.2 and 4.3.3, while the correlation between velocity parameters and electron density are discussed in Section 4.3.4.

### *4.2.3. IRIS Analysis*

In this study, both the spectral and slit-jaw imaging data from the *IRIS* instrument were used. For the entire duration of this event, the *IRIS* instrument performed a repeated fast raster scan (131.1 s cadence per complete raster) of AR 12192, with a 45° roll angle. Each spectral raster contained eight slit positions, with a spacing of 2″ and 16.32 seconds between positions. The spatial resolution for each raster was 0.33″ along the slit, with a slit width of 0.33″. No onboard spatial summing was carried out for these observations. The spectral resolution was 25.96 mÅ in the far-ultraviolet (FUV) spectral window.

The *IRIS* slit-jaw camera was used to determine the area of each flare foot-

point. While this is not a direct measurement of the HXR source size, *RHESSI* `CLEAN` imaging tends to significantly overestimate the source size (Dennis & Pernak 2009; Milligan & Dennis 2009), and *AIA* chromospheric images for this event were severely saturated during the period of interest.

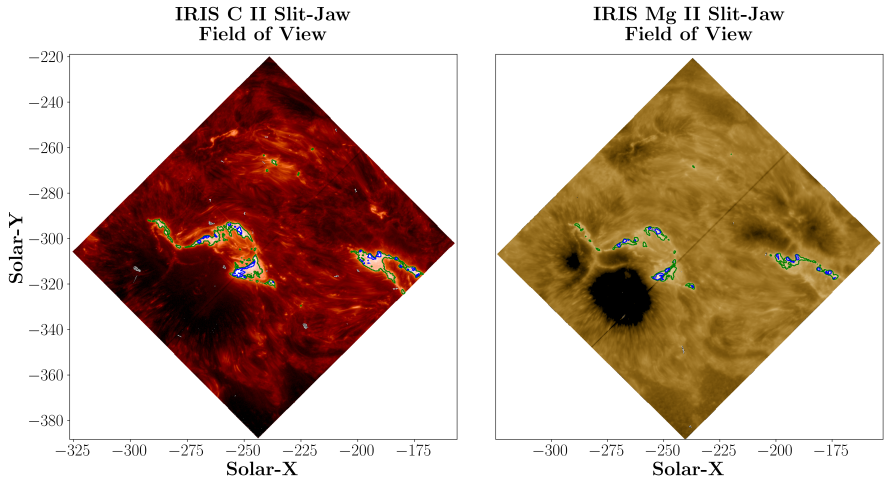


Fig. 4.7.— *IRIS* slit-jaw images showing the contours used to determine HXR footpoint areas. **Left:** C II slit-jaw image, 10% and 50% of the frame maximum. **Right:** Mg II slit-jaw image, 25% and 50% of the frame maximum.

Ribbon areas were determined from *IRIS* slit-jaw images using the 10% and 50% levels of each frame maximum. This time-dependant area measurement was interpolated from a 32-second cadence to a 16-second cadence, and rebinned to match the *RHESSI* spectral time bins. The *IRIS* slit-jaw camera experienced minimal saturation in two exposures during the peak of the flare; these were omitted from the final calculation of the footpoint area. The time-dependant areas were used to determine the injected electron energy flux in erg $s^{-1}$ $cm^{-2}$.

*IRIS* spectra were available for several ion species during this flare, from which the C II line doublets at 1334.54 and 1335.71Å, the Si IV 1402.81Å line, the

hot Fe XXI line at 1354.07Å, and the Mg II h&k doublet were selected for study. Using the standard method described by Wülser et al. (2018), radiometric and instrumental calibrations were performed. The calibrated spectra for C II, Si IV, and Fe XXI were fit with multiple component Gaussian profiles, accounting for blends where applicable (Graham & Cauzzi 2015; Young et al. 2015), and allowing for additional blue- and red-wing components to account for asymmetry in the complex C II and Si IV emission lines.

Despite the increased emissivity of the faint Fe XXI line during the flare, it becomes more difficult to accurately fit during the peak of nonthermal electron injection. This is primarily due to the *IRIS* instrument automatic exposure compensation, which scales exposures in order to avoid saturation in the more emissive ion species. During the peak of the flare, this has the unfortunate side effect of obscuring weak lines, such as Fe XXI, within the noise of the continuum. In an attempt to maximize the signal from the Fe XXI 1354.07Å line, data from this spectral window were binned by a factor of four along the slit.

Of the four species studied, only the Fe XXI emission line is known to be optically thin. However, simulations have shown that Doppler shifts of the optically-thick C II lines are well-correlated with the plasma velocity (Rathore & Carlsson 2015; Rathore et al. 2015; Rathore et al. 2015). The Si IV line is sometimes optically thin (Kerr et al. 2019; Cai et al. 2019; Peter et al. 2014), with complex wavelength and structure-dependant behaviour (Zhou et al. 2022). Unfortunately, the diagnostic line at 1393Å was not observed, and the opacity of the line could not be determined. Nevertheless, Doppler shifts were present within the line core, as were widths in excess of the thermal profile that could not be accounted for by known blends or observed asymmetry. While the calculation of nonthermal

velocity given by Equation 4.2.2 is valid only for optically thin profiles, the same quantity calculated for an optically thick profile is a useful measure of line width. In the case of an optically thick line, variations in the width of the line are linked to changes in the optical depth of the line. As with the *EIS* measurements, the quiescent regions in Si IV and C II rasters were used to calculate reference rest wavelengths. For the broad Fe XXI line, quiescent region emission of the nearby O I line is used to infer the rest wavelength.

The Mg II h&k doublet provide some of the best available chromospheric diagnostics (Leenaarts et al. 2013a,b) within the *IRIS* spectral range. Flare conditions complicate the analysis of these lines somewhat; during a flare, the self-absorption core is observed to give way to a full emissive profile, and the subordinate Mg II triplet in the same spectral region transitions from absorption to emission (Pereira et al. 2015). The Mg II k line around 2796.4Å and the T1 triplet component around 2791.6Å were chosen for study. The h component displayed behaviour extremely similar to the k line to the point of redundancy, with the k line displaying less contamination from blends, while the T1 component was resistant to saturation, but remained in absorption outside the flaring region. Utilizing a combination of the subordinate triplet component and the strong k line allowed for a balance of sensitivity outside the flare region with resistance to detector saturation.

In order to recover the general properties of these lines, two methods were used: bisector analysis and quartile analysis. Bisector analysis is performed by measuring the midpoint of the emission at different intensity levels. It is a robust and familiar method of recovering the amplitude and evolution of chromospheric condensation in optically-thick profiles (Ding et al. 1995; Graham & Cauzzi 2015).

Bisectors were measured at a variety of levels for both lines, with the 30% and 80% levels selected as proxies for the velocity of chromospheric condensation. The difference in these bisectors can additionally provide a measure of the skew or asymmetry of the line. Quartile analysis is a statistical method, computed from the normalized cumulative distribution function of the line profiles, as described by Kerr et al. (2015). The wavelengths corresponding to the 25% ($Q_1$), 50% ($Q_2$), and 75% ($Q_3$) quartiles were found, and used to derive the line center, width, and skew as

1. $\lambda_c = Q_2$, centroid
2. $W = Q_3 - Q_1$, width
3. and $S = \frac{(Q_3 - Q_2) - (Q_2 - Q_1)}{Q_3 - Q_1}$, skew.

The reference wavelengths for these lines were calculated with different methods. The Mg II k line reference wavelength was calculated from quartile analysis carried out over the quiescent regions of the raster, as it is agnostic to features such as the self-absorption core. For the Mg II T1 subordinate component, a simple Gaussian was fit to the line core across the same region, where the line profiles were simple, and observed in absorption only.

## 4.3. Results & Discussion

### *4.3.1. RHESSI Results*

*RHESSI* spectral fits were used to derive a set of thermal and nonthermal parameters for the X1.6-class flare on 2014 October 22. The thermal X-ray pa-

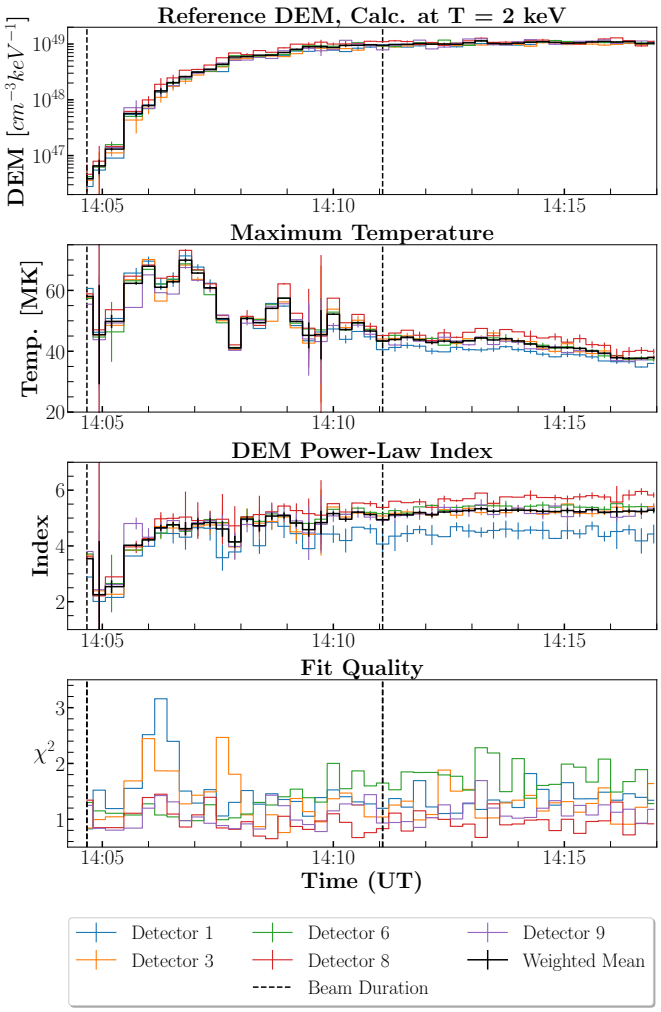


Fig. 4.8.— Thermal parameters from *RHESSI* spectral fitting. **Panel 1:** The reference differential emission measure (DEM) calculated at T=2 keV ≈ 23.2 MK) over all fitted intervals and detectors. **Panel 2:** The maximum temperature of the plasma in MK for all fit intervals and detectors. **Panel 3:** The power-law index used to calculate the DEM for all fit intervals and detectors. **Panel 4:** The reduced $\chi^2$ per fit interval and detector. The black dashed lines denote the range shown in Figure 4.9, where nonthermal emission was found.

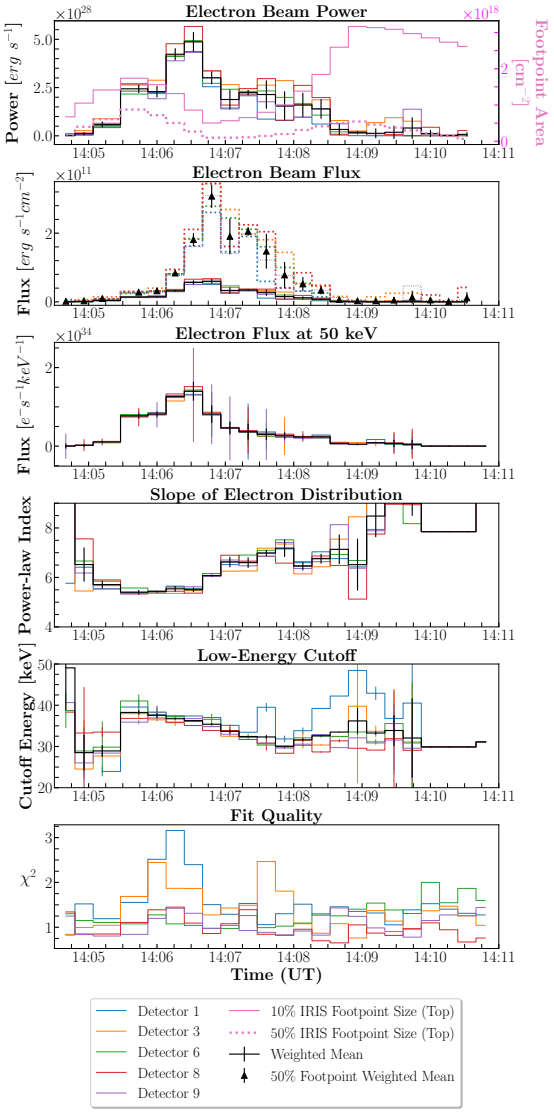


Fig. 4.9.— **Panel 1:** The power in nonthermal electrons from spectral fitting and two estimates for the *IRIS* time-dependant footpoint area, as discussed in Section 4.2.3. The time-dependant footpoint areas are shown in pink, and correspond to the right-hand axis. **Panel 2:** The flux of nonthermal electrons, obtained by dividing the power shown in Panel 1 by the time-dependant footpoint area. The conservative estimate given by the 10% footpoint contours is given as solid lines, while the estimate from a compact 50% footpoint area is shown in the dotted lines. **Panel 3:** The electron flux at the reference energy of 50 keV in units of $10^{34}$ $e^{-}$ s$^{-1}$ keV$^{-1}$. **Panel 4:** The power law slope of the nonthermal electron distribution. **Panel 5:** The low-energy electron cutoff in keV. **Panel 6:** The reduced $\chi^2$ per fit interval and detector.

rameters, derived from the multithermal model are presented in Figure 4.8. The top panel shows that the reference DEM (calculated at 2 keV, $\approx$ 23.2 MK) rose sharply soon after the onset of electron injection, and remained at approximately the same level ($\approx 10^{49}$ cm$^{-3}$ keV$^{-1}$), well after the cessation of the injection event. The upper limit on temperature, found in the second panel of the same figure, reached a peak of 70 MK early in the flare, and continued to decline for the rest of the studied interval. It is important, however, to note that this is the maximum temperature of the plasma, as characterized by a power-law DEM, and is not characteristic of the mean plasma temperature. The power-law index of the DEM increased slowly throughout the flare, as the bulk of the plasma cooled.

The nonthermal electron parameters are presented in Figure 4.9. The nonthermal electron population is best characterized by a single-power law distribution of electrons, that lasted for 352 seconds, and deposited $> 4.8 \times 10^{30}$ erg of energy. The nonthermal electron flux was first observed during the 14:04:40–14:04:56 UT interval, peaked during the interval 14:06:40–14:06:56 UT, 68 seconds after the first interval where the presence of nonthermal electrons was detected, and had ceased by 14:10:32 UT.

During the peak interval, the flux in nonthermal electrons was calculated to be between $5.99 \pm 0.66 \times 10^{10}$ erg s$^{-1}$ cm$^{-2}$, for a larger estimate of the footpoint area (corresponding to 10% of the frame maximum for *IRIS* slit-jaw imaging) and $3.07 \pm 0.34 \times 10^{11}$ erg s$^{-1}$ cm$^{-2}$, for a smaller estimate of the footpoint area (the 50% of the frame maximum).

Lee et al. (2017) fit the *RHESSI* spectrum of this event for two intervals during this flare, and calculated an energy flux of $7.7 \times 10^{10}$ erg cm$^{-2}$ s$^{-1}$ during

the time interval 14:05:32–14:06:32 UT. This is similar to the value obtained for the time interval 14:06:16–14:06:32 UT of $8.37 \pm 0.62 \times 10^{10}$ erg cm$^{-2}$ s$^{-1}$ for the more conservative 50% intensity threshold used to determine the area of the energy injection region. These results presented here are not compared with results from the second interval shown by Lee et al. (2017) ($6.1 \times 10^{10}$ erg cm$^{-2}$ s$^{-1}$ at 14:11 UT). The differences between the these two studies are primarily due to differences in footpoint area determination and the determination of the low-energy electron cutoff. This study used the time-varying 10% and 50% contours of *IRIS* imaging for footpoint area determination while Lee et al. (2017) take the 60% contour of *RHESSI* HXR imaging. This study additionally allows the low-energy electron cutoff to vary in time. This results in a cutoff between 5 and 8 keV higher than the 30 keV assumed by Lee et al. (2017). The treatment presented here additionally fits for albedo effects and instrumental pileup.

In general, the low-energy cutoff presented in this work was higher than found in other, similar, studies, particularly Milligan et al. (2014), who studied a flare of a similar size (X2.2). The study by Warmuth & Mann (2016) contained several flares of similar magnitude, all of which had low-energy cutoffs less than found here. Most similar was the X1.3 flare of 2005 January 19, studied by Warmuth et al. (2009), who found a low-energy cutoff between 30-40 keV during parts of that event. Due to the low-energy electron electron cutoff level, the particularly steep slope of nonthermal emission, and the choice of a multithermal plasma model, the derived electron power was, on the whole, weaker than studies of flares of a similar size. As with other studies (Xia et al. 2021), a consequence of uncertainty in the low-energy cutoff is that the $4.8 \times 10^{30}$ erg total energy fit should be treated only as a lower limit (Warmuth et al. 2009; Aschwanden et al. 2019).

In Figure 4.2, a secondary enhancement in the *RHESSI* 25–50 keV band occurred around 14:24 UT. At the same time, flux in the GOES 1–8Å band is boosted. Taken together, this would imply the existence of a second nonthermal event at this time. Fits to the HXR spectrum were attempted from 14:15 UT through this secondary peak, until 14:30 UT, but the presence of a second nonthermal event could not be determined. Excess HXR emission was equally well fit by a thick-target bremsstrahlung component as by a pulse-pileup phenomenon component, with both cases yielding a similar $\chi^2$. `CLEAN` images formed during this interval showed no significant sources of emission above the 30 keV low-energy electron cutoff derived during the nonthermal electron event.

### *4.3.2. EIS Results below 10 MK*

Fit-derived parameters from ions with temperature T $<$ 10 MK are shown in Figure 4.10 for the four rasters spanning 14:02:39–14:16:56 UT. Line intensities, Doppler velocities, and nonthermal velocities are shown as rows in Figure 4.10 for each raster time interval, with ion formation temperature increasing left to right across each row. Columns in Figure 4.10 correspond to one emission line each (labelled at the top of each column). Each parameter was scaled to the same range across each time interval and temperature, to allow direct comparison between ion species, and the location of the flare footpoint (from *RHESSI* 25–50 keV `CLEAN` images) is overlaid in cyan. All HXR sources are part of the eastern flare footpoint; the western footpoint lay outside the *EIS* FOV. Alignment between *EIS* rasters and *RHESSI* imaging was performed by first determining the offset between *EIS* rasters and *AIA* filtergrams using the `eis_aia_offsets` procedure

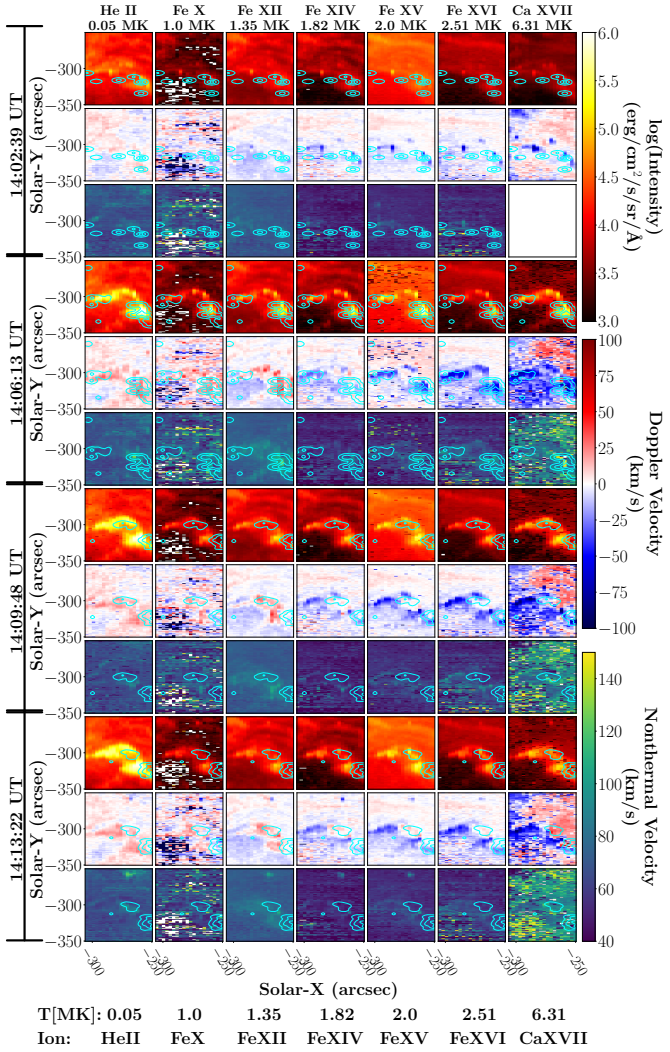


Fig. 4.10.— Line intensities, Doppler velocities, and nonthermal velocities for ions with $T < 10$ MK, for four rasters beginning at: 14:02:39 UT, 14:06:13 UT, 14:09:48 UT, and 14:13:22 UT, corresponding approximately to the pre-flare/early impulsive phase, peak impulsive phase, end of impulsive/beginning of the gradual phase, and after the cessation of nonthermal electron injection, respectively. Each column represents a different ion, with formation temperatures increasing left-to-right across the figure. The provided scales for each parameter are scaled to be consistent between observed ions and observation times. In the case of Ca XVII, there was no significant nonthermal velocity at 14:02:39 UT, and this panel is left blank. *RHESSI* 25–50 keV CLEAN imaging contours are overlaid in cyan on all images, corresponding to 5%, 30%, and 70% of the image maximum.

available in SSW, then aligning *AIA* filtergrams with *RHESSI* `CLEAN` maps. The alignment between *AIA* and *EIS* is accurate to within $\approx 5''$(Mariska 2016). The accuracy of alignment between *AIA* and *RHESSI* is accurate to $2.26''$, within the minimum spatial resolution element of *RHESSI* imaging. The middle column of Figure 4.1 shows the *EIS* FOV in context of the flaring region for comparison to the structures shown in Figure 4.10.

In the rasters beginning at 14:06:13, UT, 14:09:48 UT, and 14:13:22 UT, the velocity distribution found in *EIS* spectral lines was typical of explosive chromospheric evaporation. Within the flare footpoint, warmer ions exhibited strong blueshifts, while cooler ions exhibited only redshifts. Given adequate temperature sampling, the Doppler velocities *EIS* spectral lines can be used to derive a range for the temperature of flow reversal. The flow reversal temperature (FRT) is the temperature at which the division between evaporative upflows and condensation-driven downflows occurs during periods of explosive chromospheric evaporation. Analysis of Doppler velocities at or near this temperature provide insight into the processes that transport energy from the corona to the chromosphere (Brannon & Longcope 2014; Fisher et al. 1985). With six different ion species between T=1 MK and T=6.3 MK, the *EIS* observations presented in this study are adequate to place constraints on this temperature.

Figure 4.10 shows a clear delineation in Doppler velocity cospatial with HXR emission between 1.35–1.82 MK, first observed in the 14:06:13 UT raster. This raster spanned the time interval with the largest nonthermal electron flux density (Figure 4.9). The distribution of nonthermal electrons during this interval was characterized by a steepening power-law index. In this, and the two following rasters, the Fe XII line, formed at 1.35 MK, exhibited mild downflows within the

flare footpoint, on the order of ≈ 10–40 km $s^{-1}$, while the Fe XIV line, formed at 1.82 MK, was blueshifted between ≈ −20 and ≈ −60 km $s^{-1}$. The FRT fell within this 0.5 MK range during this raster, and remained in this range for the remainder of the flare. This range is consistent with limits determined in previous studies (Kamio et al. 2005; Milligan & Dennis 2009). Above this temperature, spectral lines were observed to have increasingly strong blueshifts, peaking at nearly -100 km $^{-1}$ for the Ca XVII line, while the cooler ions exhibited relatively consistent redshifted emission across the three cool species studied, including the weak Fe X line.

Minor evolution in the Doppler velocity distribution was found throughout the duration of the flare. The earliest raster studied, which began at 14:02:39 UT, showed markedly different behaviour compared to later observations. Nonthermal emission from *RHESSI* observations were first observed at 14:04:40 UT, thus, this raster observed both the pre-flare and early-flare chromosphere. As early as 14:03:00–14:03:11 UT, ions warmer than the FRT were observed to have blueshifted velocity enhancements, 90 s before the *RHESSI* instrument detected nonthermal emission. The Fe XVI ion, in particular displayed a blueshift of -68.9±4.6 km $s^{-1}$ in the region that subsequently became the flare footpoint. This early velocity behaviour is more consistent with gentle chromospheric evaporation (Schmieder et al. 1987; Zarro & Lemen 1988), possibly driven by a nonthermal electron component with an energy below the *RHESSI* sensitivity threshold.

The compact kernels of blueshifted emission apparent in warm (≥1.82 MK) ions during the 14:02:39 UT raster expanded to fill both lobes of the flare ribbon during the 14:06:13 UT raster. At this time, additional blueshifted material bridged the two HXR sources. By the 14:13:22 UT raster, while significant up-

flows remained in these species, they were mostly contained within the eastern structure, while the larger, western structure had begun to return to rest as early as the 14:09:48 UT raster. The blueshifted material bridging the two HXR sources persisted through the 14:09:48 UT raster, but is largely absent by 14:13:22 UT.

During the 14:02:39 UT raster, ions cooler than the FRT (He II, Fe X, and Fe XII) exhibited small Doppler velocity enhancements within the region that would later become the flare footpoint. The downflows in these species peak during the 14:06:13 UT raster (for He II, downflows peaked at $v_{max} = 41.7 \pm 5.5$ km s$^{-1}$ during this raster), gradually returning to rest over the remaining duration. The results presented here are broadly consistent with the results of Lee et al. (2017), who presented selected ion species within a point in the western lobe.

Nonthermal velocities (calculated from the line width) are shown in every third row of Figure 4.10. The highest nonthermal velocities derived from *EIS* spectral fits were found at cooler temperatures, specifically, those below the FRT, and are largest for Fe XII and He II. The ion observed by *EIS* with the smallest nonthermal velocity was Fe XIV, which is formed at a temperature just above the FRT. Ions warmer than Fe XIV showed higher nonthermal velocities with increasing temperature. There is little evolution in nonthermal velocity after 14:06:13 UT. During the 14:02:39 UT raster, the nonthermal velocity, particularly in Fe XIV, Fe XV, and Fe XVI was mildly enhanced across the region that would later become the flare footpoint. Overall, the nonthermal velocities observed are markedly similar in magnitude to those observed by Milligan (2011), though the flare studied in that work was significantly smaller (C1.1).

### *4.3.3. EIS Results above 10 MK*

Figure 4.11 shows Doppler velocity behaviour for the hottest *EIS* ions: Fe XXIII and Fe XXIV, with temperatures of 14.13 and 18.20 MK respectively. The *EIS* instrument observed one line of Fe XXIII, and two of Fe XXIV. Of the three, the reference wavelength constraints for Fe XXIV 192.02Å were most reliable, and this line serves as the focus of this discussion. In every raster where these lines were present, the core was accompanied by strong enhancements to the blue wing. Figure 4.11 presents the fits to the core and the blue wing enhancement, with time increasing top to bottom for the same four raster time intervals presented in Figure 4.10. The six columns correspond to: Fe XXIII core and blue wing, the Fe XXIV 255.13Å core and blue wing, and the Fe XXIV 192.02Å core and blue wing, while the rows alternate between intensity and Doppler velocity for these four components. For the blue wing, Doppler velocity was measured relative to the same reference wavelength as the line core. Where the detector saturated observing Fe XXIV 192.02Å, or where there was insufficient signal to fit the emission line, as was often the case outside the flare ribbon, the fits were replaced with a null value.

During the 14:02:39 UT raster, no emission was detected from the Fe XXIII line or the Fe XXIV 255.13Å line. The Fe XXIV 192.02Å line, while faint, was present in locations that later became a part of the footpoint during this time interval.

An example of this early, low-intensity emission is shown in the top panel of Figure 4.12. Where it is present at 14:02:39 UT, the magnitude of Doppler velocity for Fe XXIV is small for the core, and the separation of the wing is approximately

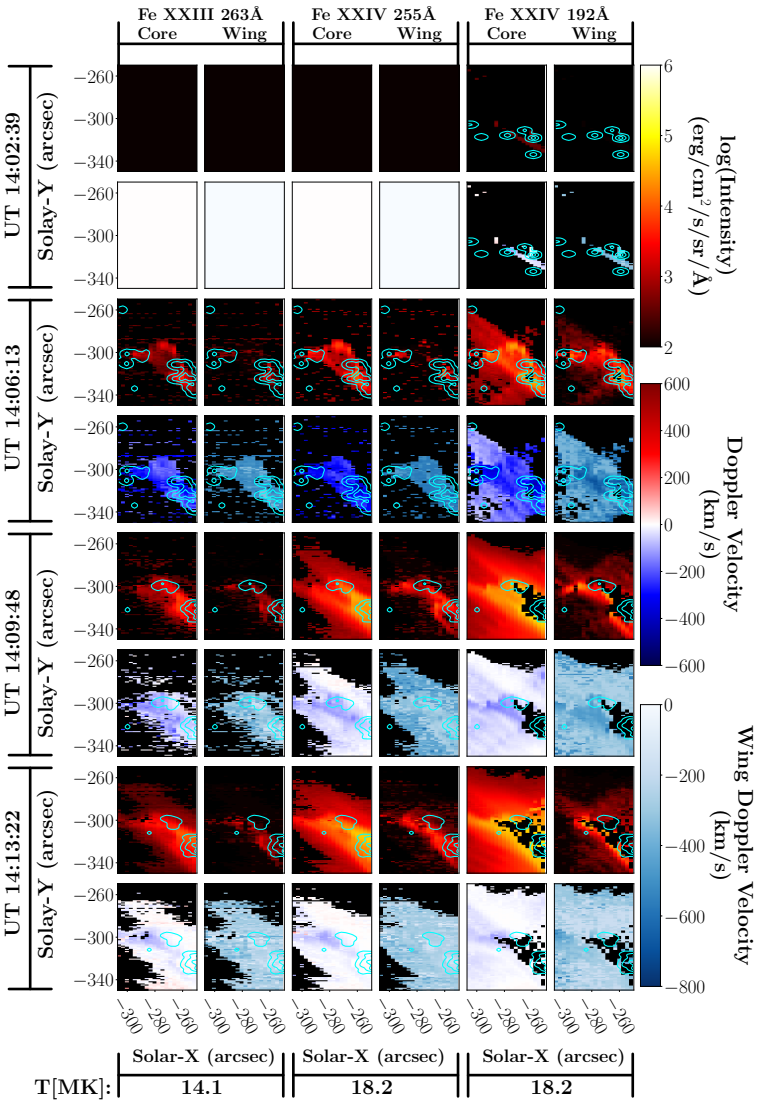


Fig. 4.11.— Line intensities, line core Doppler velocities, and velocity separation of blue-wing components for ions Fe XXIII 263.78Å, Fe XXIV 255.13Å, and Fe XXIV 192.02Å, for four rasters beginning at 14:02:39 UT, 14:06:13 UT, 14:09:48 UT, and 14:13:22 UT. These times correspond approximately to the pre-flare/early impulsive phase, peak impulsive phase, end of impulsive/beginning of the gradual phase, and after the cessation of nonthermal electron injection. Each raster time occupies two rows (intensity and Doppler velocity for each time interval), while each ion occupies two columns (line core and blue wing). The colorbar scale is consistent between ion species and observation times. At the earliest times, only Fe XXIV 192.02Å displays emission above the background. *RHESSI* 25–50 keV CLEAN imaging contours are overlaid in cyan on all images, corresponding to 5%, 30%, and 70% of the image maximum.

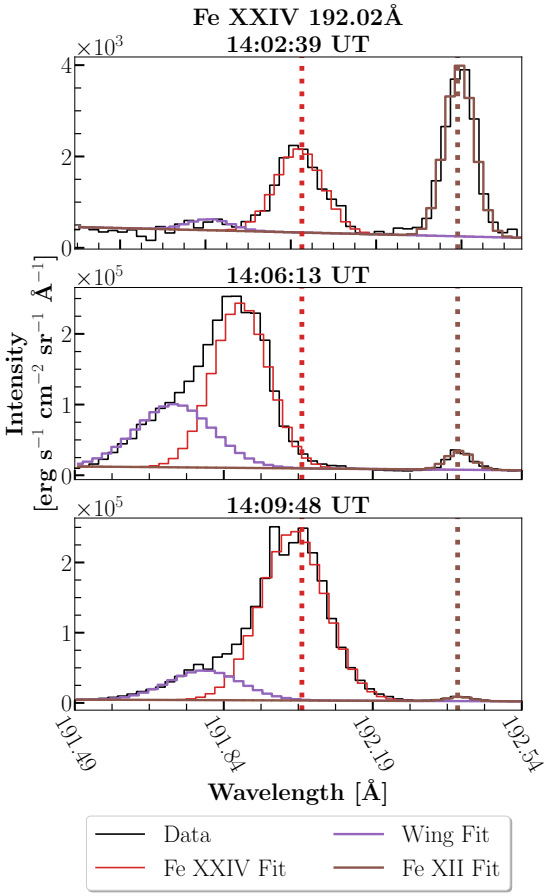


Fig. 4.12.— The Fe XXIV 192.02Å complex for three times, 14:02:39 UT (**Top**, pre-nonthermal HXR), 14:06:13 UT (**Middle**, peak nonthermal HXR), and 14:09:48 UT (**Bottom**, late nonthermal HXR). Fit profiles for the core of the line are shown along with the fit to the blue wing enhancement and the fit to the Fe XII 192.39Å line used for reference wavelength determination. The rest position of Fe XXIV is overlaid as the **dotted red** line, and the **dotted** brown line denotes the rest position of the Fe XII line. Note the difference in intensity scale between the top and middle panels.

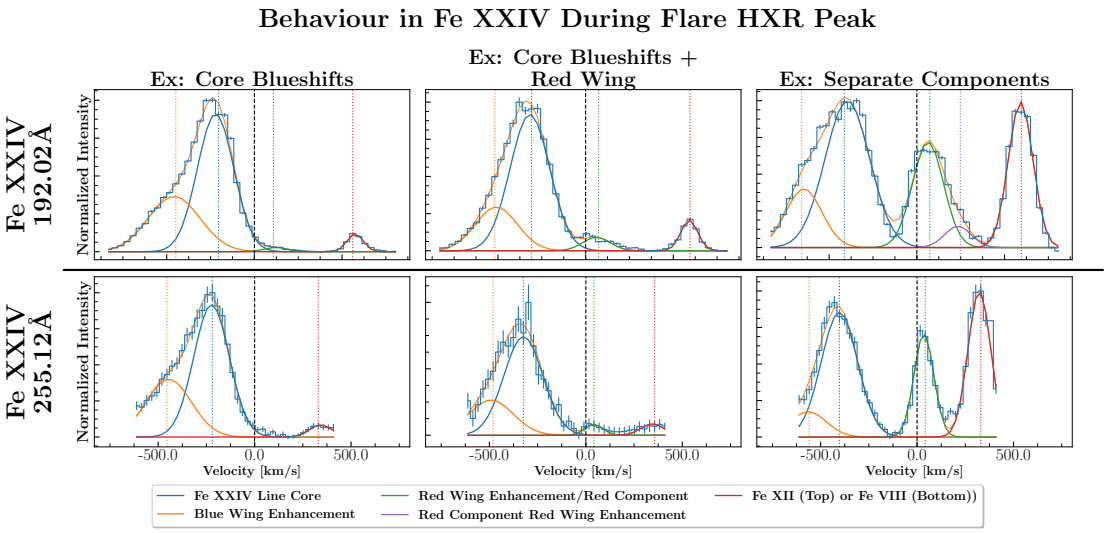


Fig. 4.13.— In addition to the evolution of the Fe XXIV profile through time (see Figure 4.12), the 14:06:13 UT raster shows significant profile variations across the field of view. Three typical behaviours are observed; an example of each is given for each the 192.02Å line (top) and the 255.12Å line (bottom).

constant.

Significant Fe XXIII and Fe XXIV 255.13Å emission first appeared during the 14:06:13 UT raster, and grew in intensity with each successive raster. All three lines exhibited core blueshifts within the footpoint at this time, with further blue-wing enhancement. The Doppler velocity of the blue wing peaked during the 14:06:13 UT raster, and decreased thereafter.

Generally, these hot ions are expected to display a stationary core, with an enhanced blue wing (Milligan & Dennis 2009). During the raster covering the flare peak (14:06:13 UT), however, the entire line complex for both the Fe XXIII line, and the Fe XXIV line pair was significantly blueshifted. Within non-saturated footpoint pixels, the *core* of the Fe XXIV 192.02Å line was found to have blueshifts as high as -240 km $s^{-1}$, while maintaining a blue wing enhancement. For the same

profile, the blue wing velocity was as high as -480 km $s^{-1}$, relative to the same reference wavelength. By the 19:09:48 UT raster, while core blueshifts were still found within the flare ribbon, the magnitude and extent were far less than found one raster prior, and by 14:13:22 UT the core of these lines had mostly returned to rest. Significant Doppler velocities observed in the "rest" component of this line complex is not expected. An example of this atypical behaviour is shown in Figure 4.12, which shows the Fe XXIV 192.02Å complex across three rasters from the same location.

The situation becomes even more complex for the 14:06:13 UT raster. Figure 4.13 shows three examples of atypical Fe XXIV emission for both the 192.0Å line (top row) and 255.12Å line (bottom). The left column shows the "simple" situation of a core blueshift with a blue-wing enhancement, also shown in the middle panel of Figure 4.12. The middle column shows a profile that is similar to the expected situation, where a nearly-stationary component is present. However, where it is present at this time, the stationary component is significantly diminished relative to the first blueshifted component, all of which maintain a further blue-wing enhancement. The right-hand column shows perhaps the most confusing profile, found in only a small number of pixels. In both Fe XXIV lines, in addition to the blueshifted component, the associated blue-wing enhancement, and the blend profiles (Fe XII in the 192Å window, and a combination of Fe VIII and Fe XVII in the 255Å window), a profile is found at a redshift of 30–60 km $s^{-1}$. It appears at approximately the same location in both lines, and it is never found in one line where it is not present in the other. This points to it being yet another component of Fe XXIV emission. If this is the case, there are three separate and distinct flow structures within these pixels.

### 4.3.4. EIS Densities

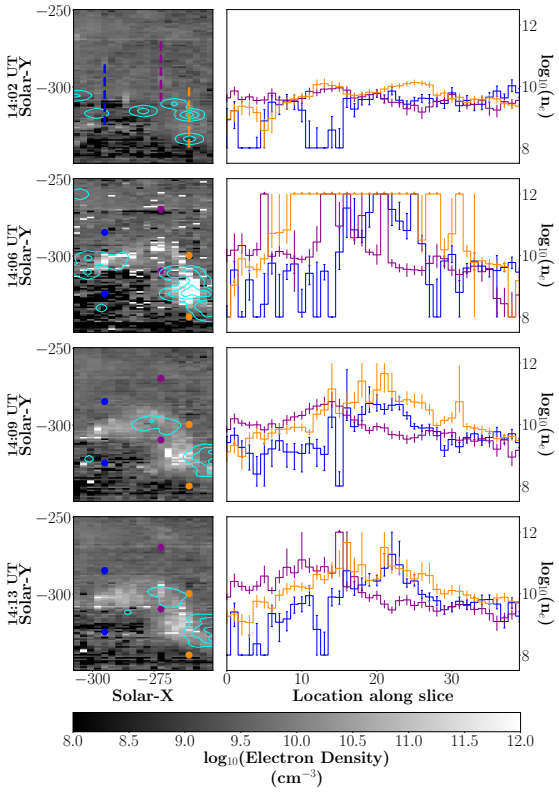


Fig. 4.14.— Fe XIV 264.81/274.23 Å calculated electron density. **Left:** Density maps for four *EIS* rasters spanning the impulsive, peak, and early gradual phases of the flare. **Right:** Selected density slices along the flare ribbon. Each slice is cospatial with an HXR emitting source during one or more raster. The raster beginning at 14:02:39 UT has three dashed lines overplotted corresponding to the location in the raster of each slice. The lines are omitted for following times, but the endpoints remain as a reference. *RHESSI* 25–50 keV CLEAN imaging contours are overlaid in cyan on all images, corresponding to 5%, 30%, and 70% of the HXR maximum.

Density maps formed from the Fe XIV 264.81/274.23 Å line pair are presented in Figure 4.14 (left column) for the same four raster times as shown in Figures 4.10 and 4.11, with extracted slices in the Solar-Y direction shown in

Table 4.3: Density, Velocity Correlation Coefficients

| **Ion:** | **Raster:** (UT) | **Pearson $\|r\|$:** $n_e$, $v_{nth}$ | **Pearson $\|r\|$:** $v_{nth}$, $v_{Dopp}$ |
|---|---|---|---|
| Fe XII | 14:02:39 | — | 0.151 |
| Fe XII | 14:06:13 | — | 0.624 |
| Fe XII | 14:09:48 | — | 0.502 |
| Fe XII | 14:13:22 | — | 0.526 |
| Fe XIV[a] | 14:02:39 | 0.037 | 0.377 |
| Fe XIV | 14:06:13 | 0.069 | 0.360 |
| Fe XIV | 14:09:48 | 0.095 | 0.114 |
| Fe XIV | 14:13:22 | 0.040 | 0.032 |
| Fe XIV[b] | 14:02:39 | 0.014 | 0.287 |
| Fe XIV | 14:06:13 | 0.092 | 0.063 |
| Fe XIV | 14:09:48 | 0.114 | 0.045 |
| Fe XIV | 14:13:22 | 0.112 | 0.058 |
| Fe XV | 14:02:39 | — | 0.710 |
| Fe XV | 14:06:13 | — | 0.102 |
| Fe XV | 14:09:48 | — | 0.089 |
| Fe XV | 14:13:22 | — | 0.273 |
| Fe XVI | 14:02:39 | — | 0.714 |
| Fe XVI | 14:06:13 | — | 0.506 |
| Fe XVI | 14:09:48 | — | 0.579 |
| Fe XVI | 14:13:22 | — | 0.545 |

[a] 264.81Å

[b] 274.23Å

the right column, in order to provide a density cross section of the flare ribbon. The three slices selected for plotting are the same at every time, and are color-coordinated (such that the purple points on the left image denote the start and end of the purple curve right). The density evolution along the flare ribbon (identified by cyan *RHESSI* `CLEAN` contours) exceeded the upper limit of the line ratio at various times. Several regions within the ribbon exceed the limits of the intensity ratio, reaching electron densities greater than $10^{12}$ cm$^{-3}$, with the highest densities over the largest areas found in the 14:06:13 UT raster. Lee et al. (2017) focused on a particular kernel of density enhancement, the peak of which coincided with the SXR emission peak, with only a smaller enhancement found at 14:06:13 UT. However, when the entire field of view is considered, the density enhancement is greatest during the peak of the nonthermal electron event, with much of the field exceeding the limits of the density relation.

Potential mechanisms responsible for excess line broadening within the flare ribbon can be investigated by correlations of density, nonthermal velocity, and Doppler velocity. A strong correlation between Doppler and nonthermal velocity within the flare ribbon may be indicative of a blend of unresolved plasma flows. Conversely, a stronger correlation between electron density and nonthermal velocity would indicate other effects, such as opacity, pressure, or potentially even turbulent broadening, are dominant. Measured correlations between these quantities within the flare ribbon are presented in Table 4.3 for Fe XII, Fe XIV, Fe XV, and Fe XVI, which span a 1.15 MK range. No correlations are presented with density for Fe XII, Fe XV, or Fe XVI, as there are no reliable density measurements in these lines.

For the entire duration studied, neither Fe XIV line exhibited any correlation

between electron density and nonthermal velocity. There is a weak correlation between nonthermal velocity and the Doppler shift of the line core, with a peak correlation of $|r|$=0.377 in Fe XIV 264.81Å during the early flare 14:02:39 UT raster. The two hotter lines exhibited correlation between nonthermal velocity and Doppler velocity during the 14:02:39 UT raster. By the 14:06:13 UT raster, this correlation is found only in Fe XVI. The cooler Fe XII 195.12Å line only exhibits correlation between nonthermal and Doppler velocities after the peak of energy injection. During the 14:06:13 UT raster, coincident with the peak of nonthermal electron injection, this correlation peaked at $|r|$= 0.624, indicating significant unresolved flow structure.

The behaviour of the Fe XIV line pair stands in contrast with Milligan (2011), who found a strong correlation between nonthermal velocities and densities within the this line pair. The low correlations are more consistent with the findings of Doschek et al. (2007), who studied plasma in a quiescent active region and also found no evidence of such a correlation.

These correlations, taken from temperatures surrounding the FRT are a signature of explosive chromospheric evaporation, as observed in the vicinity of a major energy deposition layer. At temperatures above and below the FRT, the nonthermal widths are likely due to a superposition of unresolved flows. Near the FRT, both nonthermal and Doppler velocities were small, implying that the Doppler velocity structure was well resolved.

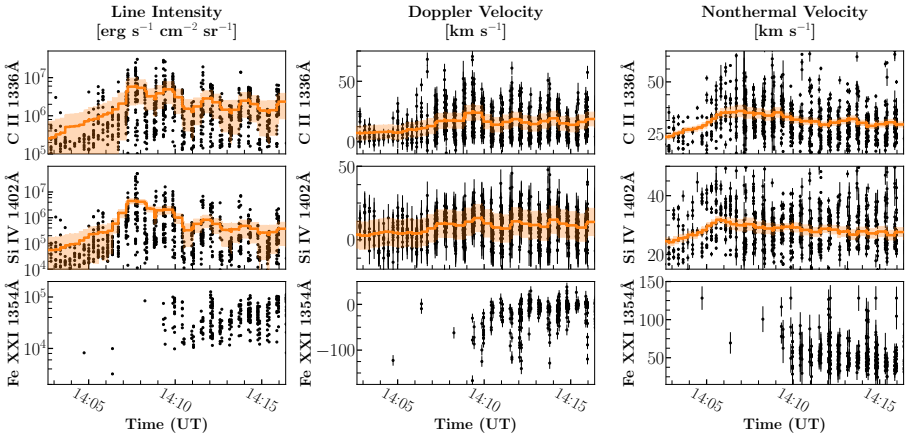


Fig. 4.15.— *IRIS* spectral fitting results for the C II 1335.71Å line (**Top** row), Si IV 1402.81Å (**Middle** row), and Fe XXI 1354.07Å (**Bottom** row). **Left Column:** Intensity for each of the three lines. **Middle Column:** Doppler velocity for each of the three lines. **Right Column:** Nonthermal velocity width for each of the three lines. For C II 1335.71Å and Si IV 1402.81Å, which are signficantly brighter, and more easily fit that Fe XXI 1354.07Å, the running mean of each parameter is overlaid in orange. Note that the appearance of periodicity in the running mean of C II and Si IV parameters is an artifact induced by the loss of spatial information.

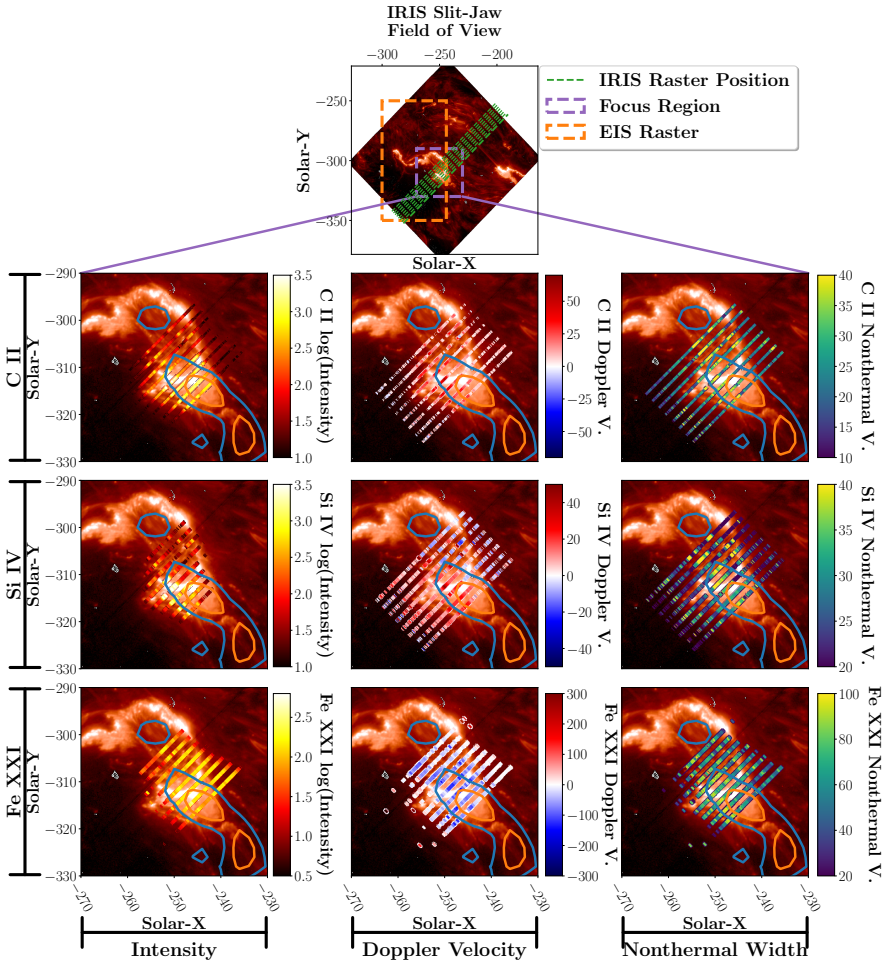


Fig. 4.16.— Spectral fitting parameters from the *IRIS* raster spanning 14:08:21–14:10:24 UT, superimposed upon the co-temporal C II slit-jaw image. **Top:** the full slit-jaw image with the field-of-view of the *EIS* instrument overlaid in orange, and each raster slit position shown in green. The purple box denotes the region of interest shown in each panel below. Each column denotes the line intensity (in photons $s^{-1}$ $Å^{-1}$), the Doppler velocity of the line (in km $s^{-1}$, and the nonthermal width (in km $s^{-1}$), for C II 1335.71Å (**Top**), Si IV 1402.81Å (**Middle**), and Fe XXI 1354.07Å (**Bottom**). In the case of Fe XXI, where fewer profiles could be fit, the overlaid images are integrated through the duration studied, taking the value with the larger magnitude where multiple values existed. The width of the *IRIS* slit has been exaggerated by a factor of five. Overlaid contours represent the 25% (blue) and 50% (orange) levels of *RHESSI* 40–100 keV emission.

### *4.3.5. IRIS Results*

Line intensities, Doppler velocities, and nonthermal velocities from *IRIS* spectral fitting are shown in Figure 4.15 for each of the three ions fit for pixels lying within the flare ribbon. Points lying outside the flare ribbon were masked. The left column shows the integrated line intensity for C II 1335.71Å, Si IV 1402.81Å, and Fe XXI 1354.07Å, while the middle shows the Doppler velocity, and the right shows nonthermal velocities. For the bright C II and Si IV lines, the running mean of each parameter is overlaid in orange, with the $1\sigma$ error in the running mean overlaid as filled contours in the same color.

The cool Si IV and C II ions, exhibit small Doppler shifts. Over the duration of the event, 81% of Si IV profiles, and 96% of C II profiles were redshifted, with peak velocities of 47.9 $\pm$ 9.6 km s$^{-1}$ at 14:09:19 UT and 59.6 $\pm$ 5.6 km s$^{-1}$ at 14:07:16 UT, respectively. This cool chromospheric condensation provides context for *EIS* observations of He II. For example, He II exhibited a maximum redshift of 41.7 $\pm$ 5.5 km s$^{-1}$ during the 14:06:13 UT raster. At this time (14:06:42 UT), Si IV redshifts peaked at 27.6 $\pm$ 9.4 km s$^{-1}$.

More notable is the behaviour of the calculated nonthermal velocity for Si IV. The running mean of this quantity peaks at 14:05:49 UT, with a mean nonthermal velocity of 31.9$\pm$1.0 km s$^{-1}$. This is coincident with the time of the hardest electron distribution, with a power-law index less than 6. As the nonthermal velocities in Si IV level off later in the flare, and finally flattens at 14:10 UT, the power-law index increases, until the nonthermal electron event ceases shortly before 14:11 UT. In the case of Si IV, at least, the excess widths calculated from spectral fitting may be linked to line opacity changes, driven by the deposition of

energy from a particularly hard distribution of nonthermal electrons.

For the hot, low-emissivity Fe XXI line, there are comparatively few spectra with significant observable emission, particularly at earlier times. The earliest instance of an Fe XXI profile that could be reasonably fit was at 14:04:44 UT, and was already highly blueshifted to -122.5 $\pm$ 11.6 km s$^{-1}$, with a nonthermal width of 128.2 $\pm$ 15.4 km s$^{-1}$. Most of the emission from this line during the flare impulsive phase was obscured by high levels of noise in the continuum as a consequence of shorter exposure times. At later times in the flare, Fe XXI was observed to have Doppler velocities mostly between 0– -80 km s$^{-1}$, with outliers observed in excess of -150 km s$^{-1}$ ($|v_{max}|= 166.67 \pm 11.4$ km s$^{-1}$ at 14:09:19 UT).

The Doppler shifts presented here are observed earlier and have values in excess of those profiles fit by Lee et al. (2017), who found no Fe XXI Doppler velocities in excess of -60 km s$^{-1}$, which they measured at 14:10 UT, for a particular kernel of emission. Li et al. (2015) were able to fit velocities as early as 13:45 UT. However, their measured Doppler velocities were, overall, smaller. Comparable Doppler velocities were found by Li et al. (2015), who studied an X1.0 flare that occurred on 2014 March 29, and found Fe XXI Doppler velocities of $-214$ km s$^{-1}$. Tian et al. (2015) also found similar blueshifts for the X1.6 flare on 2014 September 10, reaching a maximum of $-240$ km s$^{-1}$, while Graham & Cauzzi (2015) found velocities of up to $-300$ km s$^{-1}$ for the same event.

Fe XXI nonthermal velocities were high for the entire duration of the flare, with a mean of 54.5 km s$^{-1}$ and an observed maximum nonthermal velocity of 128.2 $\pm$ 15.1 km s$^{-1}$. These measurements are larger by than other studies of this flare. Lee et al. (2017) found no nonthermal velocities greater than $\approx$

54 km $s^{-1}$ (0.6Å FWHM) within the kernel chosen by that study. The nonthermal velocities presented here are some of the highest observed for this ion, comparable to observations by Graham & Cauzzi (2015), Polito et al. (2015), and Polito et al. (2016).

All parameters in Figure 4.15 exhibited a large amount of scatter. As only pixels within the flare ribbon were selected, the remaining scatter must be due to differences across the field-of-view. The spatial context for these measurements is shown in Figure 4.16, which shows the line intensities, Doppler velocities, and nonthermal velocities along each raster. For the C II and Si IV lines, the raster beginning at 14:08:21 UT was selected for the high spatial coverage and low levels of saturation. For the weak Fe XXI line, the entire time span was stacked to provide a coherent depiction of the region of interest. Where multiple Fe XXI profiles were present, the parameter of greatest magnitude was selected for display.

When displayed in this manner, it is apparent that enhancements in C II and Si IV intensity, Doppler velocity, and nonthermal velocity track the structure of the flare ribbon. The Fe XXI intensities, Doppler velocities, and nonthermal velocities, however, do not appear to track the flare ribbon. Rather, enhancements in these parameters appear to trace the edges of a loop structure connecting the two flare ribbons visible in slit-jaw imaging. A similar structure appears in the hottest *EIS* ions (Fe XXIII and Fe XXIV) during the 14:09:48 UT and 14:13:22 UT rasters. As this structure is not visible in any other *EIS* emission lines, the minimum temperature of this structure must be between 6.31 MK (Ca XVII) and 11.48 MK (Fe XXI).

### *4.3.6. Mg II Results*

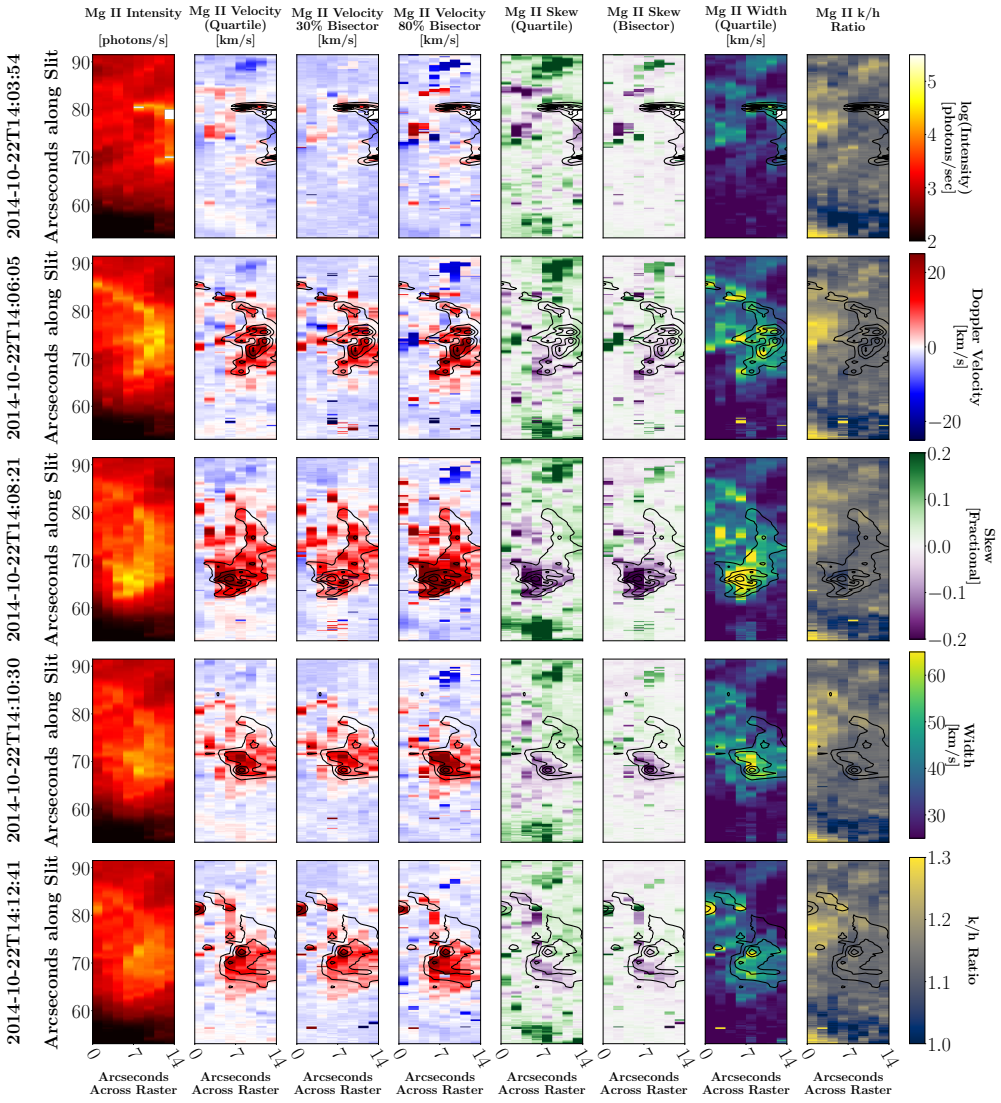


Fig. 4.17.— Mg II k line intensities, Doppler velocity metrics, line skew measurements, linewidths, and the Mg II k/h intensity ratio for five times corresponding approximately to those displayed in Figures 4.10 and 4.11. Contours corresponding to the 20%, 40%, 60%, and 80% intensity levels are overlaid on the velocity, skew, width, and ratio plots. Velocity and skew measurements from both quartile and bisector analyses are shown. The progression of flare energy deposition can be seen traveling right-to-left across the field of view during the first three rasters. Note that the axes are in units of arcseconds across the field-of-view due to the 45° tilt of the spacecraft.

Line intensities, Doppler velocities, measures of line asymmetry, and line widths from *IRIS* Mg II spectral analysis are shown in Figures 4.17 & 4.18 for five times that correspond approximately to the same times as the *EIS* rasters shown in Chapter 4.3.2. Each row corresponds to one raster, advancing from top to bottom. The columns of each figure display a different metric. The first column shows the integrated intensity in the line. The second, third, and fourth column each show a different metric for the velocity. The second column shows the velocity as measured from quartile analysis, while the third and fourth show velocities at two bisector positions. The fifth and sixth columns show the skew of the line as measure from the quartile analysis and the slope of the bisector analysis. A negative skew indicates a blue asymmetry in the line relative to the position of its peak, while a positive skew indicates a red asymmetry. The seventh column shows the width of the line from quartile analysis. Figure 4.17 additionally shows the ratio of the Mg II k/h intensities.

The intensity ratio of the Mg II line pair is nearly constant at $\approx 1.13$, with little variation found throughout the flare, or across the field-of-view. This is consistent with an optically-thick plasma (Schmelz et al. 1997; Mathioudakis et al. 1999; Kerr et al. 2015), and indicates that radiative processes cannot be directly responsible for intensity enhancements (as that would result in a line ratio closer to 4 (Harra et al. 2014)). As electron impact excitation is the dominant mechanism responsible for populating the upper levels of the Mg II h&k lines, intensity enhancements are indicative of density enhancements within the same region.

For the first three rasters, enhancements in intensity, velocity, skew, and width are observed travelling diagonally across the frame. The orientation of the overlying loop (Figure 4.1) and positioning of the HXR footpoints (Fig-

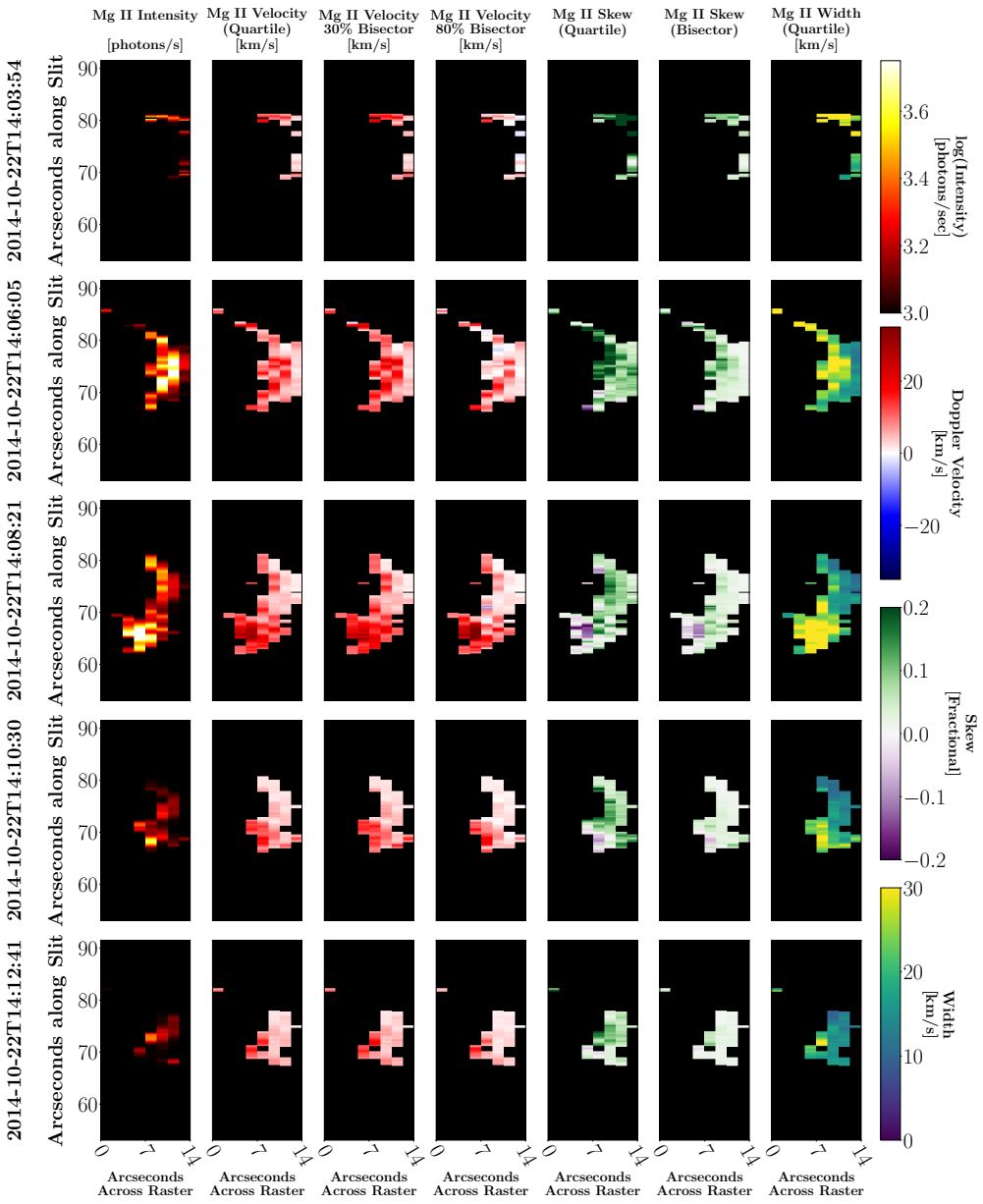


Fig. 4.18.— Mg II subordinate triplet, 2791.6Å component, line intensities, Doppler velocity metrics, line skew measurements, and linewidths from both quartile and bisector analyses for five times corresponding approximately to those displayed in Figures 4.10 and 4.11. The progression of flare energy deposition can be seen traveling right-to-left across the field of view during the first three rasters. Note that the axes are in units of arcseconds across the field-of-view due to the 45° tilt of the spacecraft. Locations where the triplet line was found to have negligible emission, or were observed in absorption are masked.

ures 4.7 & 4.16) implies that this perceived motion is occurring in the same direction as the nonthermal electron propagation. For all rasters, the region of largest Doppler velocity was coincident with intensity enhancements, and all velocity diagnostics showed redshifts coincident with greatest intensity. As shown in Figure 4.16, these enhancements are coincident with HXR emission. Within this region, the skew in Mg II k is negative for both metrics, implying blue wing enhancement in the fully-redshifted line profiles. Taken together, this is a clear signature of explosive chromospheric evaporation, as observed with *EIS* extending to deeply chromospheric layers, and directly driven by an injected population of nonthermal electrons.

The behaviour in the subordinate triplet line is much the same. The progression across the frame is clear when absorption profiles are masked, and redshifts are observed of a similar magnitude as the Mg II k profiles. The line widths are, overall, narrower, as expected for the weaker line. Skew measurements in the subordinate line are far more mixed. Early in the flare, there are pronounced red-wing enhancements, and only some compact regions show the blue wing enhancement observed in Mg II k during the 14:08:21 UT raster.

## 4.4. Evolution of Doppler and Nonthermal Velocity as a function of Temperature

Figure 4.19 shows Doppler and nonthermal velocities as a function of temperature and time for a region within the primary flare ribbon. The *IRIS* data are cospatial with *EIS* data, and approximately co-temporal to the extent that the differing cadences could be matched. For ions that exhibited a strong blue-

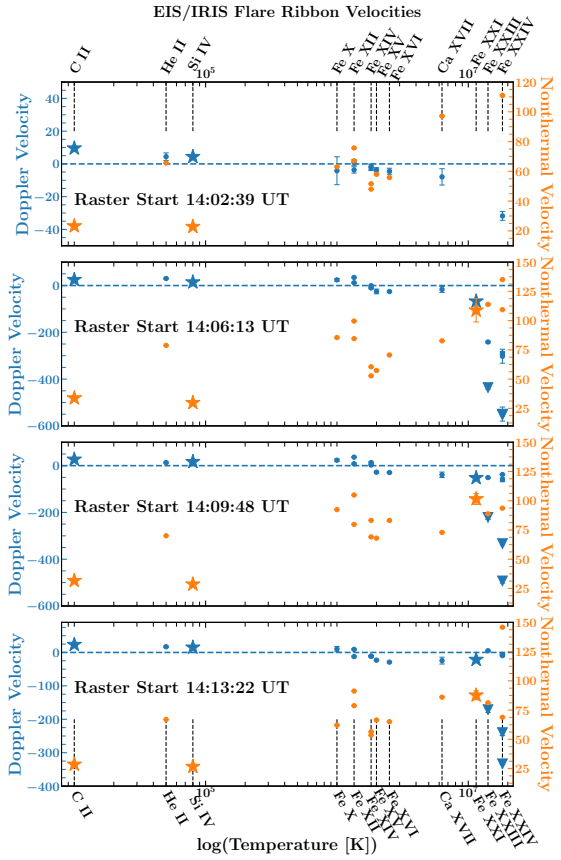


Fig. 4.19.— Spatially-averaged Doppler and nonthermal velocities taken from a region in the center of the HXR footpoint (approximate coordinates are X: -250″, Y: -320″), for each of the four rasters presented in Figure 4.10. Doppler velocities are shown in blue, while nonthermal velocities are shown in orange. Points obtained from *IRIS* spectral fitting are denoted by stars ($\star$), and points corresponding to *EIS* line core fits are denoted by circles, while fit blue wing enhancements are denoted by triangles ($\nabla$). Each point displays associated error bars. However, the wide span of velocities causes many of the error bars to fall within the area subtended by the data point.

wing enhancement (Fe XXIII and Fe XXIV), the Doppler velocities of the core and wing components are included, as well as the nonthermal velocity of the core component only.

The FRT is clearly between Fe XII and Fe XIV. *IRIS* observations showed redshifts from chromospheric condensation, which continued to the coolest temperatures studied. Within the blueshifted lines, the Fe XXI line observed with *IRIS* appeared to more consistent with the blueshifts observed in the cores of the Fe XXIII and Fe XXIV lines, rather than the blue wing enhancements (which were noticeable outliers in Doppler velocity).

Nonthermal velocities increased with temperature from the cool *IRIS* lines through the Fe XII line observed by *EIS*. There was a sudden drop in nonthermal velocity at this temperature, observed to some extent in all time bins studied. Within the blueshifted lines, the nonthermal velocity again increased with increasing temperature approximately linearly through Fe XXIV. The Fe XXI *IRIS* line fit well into this linear relation. By the 14:13:22 UT raster, while the break in nonthermal velocities was still present, the relation has become a great deal more shallow when compared to the peak raster at 14:06:13 UT.

## 4.5. Discussion and Conclusions

Solar flares are true multiwavelength events in every sense of the word, with telltale signatures across spectral bands from radio to HXR. Events covered with a wide range of instrumentation across a wide spectral range are exceedingly rare (Milligan & Ireland 2018). A holistic understanding of the generation, transport, and deposition of flare energies may be composed by integration of the many

spectral windows provided by numerous instruments in the current state-of-the-art. These connected observations of the response of the chromosphere to the call of electron injection are critical to initializing models and guiding the results of numerical simulations.

In this work, a notably-complete set of observations were used to relate the flare-driven nonthermal energy release with the response of the chromosphere. The results presented here place an emphasis on the time-resolved profile of nonthermal electron-driven emission in conjunction with the evolving chromosphere. The nonthermal electron distribution was provided via *RHESSI* spectral fitting, while emission lines observed with the *EIS* and *IRIS* instruments probed the response of the event in intensity, Doppler velocity, nonthermal velocity, and density. As the nonthermal electron event began and proceeded, the chromosphere was observed to transition from gentle to explosive chromospheric evaporation, with densities and high-temperature velocities peaking during the interval identified as the peak of nonthermal electron energy deposition.

The injection of nonthermal electrons lasted 352 seconds and deposited more than 4.8 $\times 10^{30}$ erg into the chromosphere. Prior to the onset of nonthermal emission, gentle chromospheric evaporation was observed in *EIS* rasters, characterized by compact blueshifted regions observed in ions with T $\geq$ 1.35 MK. After this time, the chromosphere responded explosively, with upflows in excess of -50 km s$^{-1}$ in Fe XVI, -65 km s$^{-1}$ in Ca XVII, and a core blueshift of $-242$ km s$^{-1}$ in the Fe XXIV line.

During the period of explosive chromospheric evaporation, several unique behaviours were observed in *EIS* rasters. Most notable was the monolithic shift

of the Fe XXIV complex. Typically, the Fe XXIV line can be well characterized by a stationary core, with a strong enhancement to the blue wing, characterized by a blend of Gaussian profiles. While this behaviour is observed at various times during the event, *EIS* raster covering the peak of the flare (14:06:13 UT) exhibited monolithic shifts of the entire Fe XXIV line complex, with little to no stationary emission. This behaviour is greatly diminished by the start of the next raster, and absent by the following.

The presence of blue wing enhanced spectral lines at hot temperatures was first noted in observations of Ca XIX using the Bragg Crystal Spectrometer (BCS) aboard *Yokoh* by Doschek & Warren (2005). Milligan & Dennis (2009) found similar profiles in *EIS* observations of Fe XXIII and Fe XXIV lines during a solar flare. This behaviour was theorized to be a consequence of the low spatial resolutions of these instruments (BCS in particular was a disk-integrated instrument). The low resolution had the effect of superimposing stationary looptop emission with blueshifted footpoint emission. Confirmation seemingly came with observations of the Fe XXI line utilizing the higher-resolution *IRIS* instrument. Graham & Cauzzi (2015); Polito et al. (2015, 2016) found that this line exhibited no notable asymmetry. Doschek et al. (2013) and Brosius (2013) both found instances of symmetric, blueshifted Fe XXIII profiles in an M1.8 and C1 flare, respectively. The behaviour exhibited by the Fe XXIV line here, where the core of the line was found to be highly blueshifted while maintaining an enhanced blue wing is not an expected behaviour.

This behavior may be attributed to a superposition of unresolved flows. During the peak of this flare, several atmospheric strata with temperatures $\geq 14.1$ MK could have formed. However, the absence of a stationary population of 14.1 MK

plasma until late in the flare remains unexplained. That it is present later in the event could indicate either that the stationary plasma was heated beyond the 18.2 MK Fe XXIV formation temperature, or that the looptop heating lagged behind the heating of the flare footpoint. *RHESSI* spectral fitting showed the presence of plasma as hot as 70 MK during the peak of the flare, and as hot as 40 MK by the time a strong stationary core was observed at 14:13:22 UT.

The temperature sampling provided by the *EIS* instrument allowed constraints on the FRT, which was found to be in the range 1.35–1.82 MK. This is comparable to the FRT presented in Milligan & Dennis (2009), between 1.5–2.0 MK, despite the differences in flare size (GOES C1.1 versus X1.6). This is similar to values presented by several other studies, including Graham et al. (2011) (1.25–1.6 MK for a C6.6 flare), Young et al. (2013) (1.1–1.6 MK for an M1.1 flare), and Watanabe & Imada (2020), who found two FRTs; T<1.3 MK in one region, 1.3<T<1.8 MK in another during an X1.8 flare. Brannon & Longcope (2014), however, modeled flow reversal properties in flares driven by thermal conduction, and found FRTs ranging from 0.526–4.78 MK, with some evolution in time. While the FRT range found for this event is similar to the range found in much smaller events, the area affected by the energy input is significantly larger, with a second flare ribbon well outside the *EIS* field for this event. It may be that flow reversal always, or nearly always occurs around this temperature, which is independent of deposited energy.

Every emission line studied exhibited line broadening. In *EIS* rasters, the smallest nonthermal velocities are found just above the FRT in the Fe XIV emission line pair. The nonthermal velocities of *EIS* emission lines increase up to the FRT, with a sudden drop in nonthermal velocity just above temperature, before

increasing again to the highest temperatures. Two particular emission lines, Si IV and Fe XXI, both observed by the *IRIS* instrument, are of note. The Fe XXI line exhibited broad, symmetric profiles, that were often low-intensity. While the magnitude of the nonthermal widths of these profiles are not unprecedented (Young et al. 2015; Lee et al. 2017; Kerr et al. 2020), they are among the broadest yet observed (Graham & Cauzzi 2015; Polito et al. 2015, 2016). Broad, highly-shifted profiles in this line appeared early in the flare, prior to the peak of electron injection, implying that even relatively weak electron precipitation is sufficient to generate profiles with large nonthermal widths, lending further questions as to their generation (Polito et al. 2019). The cool Si IV line also exhibited enhanced nonthermal widths, albeit at a much lower level. These enhancements are notable due to their similarity with the evolution of the nonthermal electron spectral index, implying that the nonthermal velocity enhancement at cool temperatures may be linked directly to the deposition of energy in the lower atmosphere by nonthermal electrons.

The electron density within the flare footpoint, as measured by the Fe XIV 264.81/274.23 Å ratio, increased by nearly two orders of magnitude in the minutes following the onset of the electron injection event. Enhancements in nonthermal velocity in Fe XIV were found to be small and not correlated with the density or Doppler velocity, standing in contrast to the findings of Milligan (2011). The Fe XVI emission line exhibited correlation between Doppler and nonthermal velocity, in agreement with the findings of Milligan (2011) and Doschek et al. (2013) for this emission line. A significant correlation was also observed between the Doppler and nonthermal Fe XII velocities, suggesting that nonthermal velocities in lines formed above and below the FRT originated from unresolved velocity flow

structures along the line of sight, similar to the findings of Young et al. (2013).

The behaviour of the optically-thick Mg II lines provides further insight to the dynamics throughout the chromosphere. The brightest kernels of both the Mg II k-line and the subordinate triplet component were observed to travel along the direction of the overlying loop, with significant redshifts observed in both bisectors and quartile measurements. The regions of peak intensity coincide with the largest linewidths, and the ratio of the Mg II k/h line intensities rule out significant radiative processes driving intensity enhancements. Skew in the line profiles differed between the resonant k-line and the subordinate triplet component, with the k-line exhibiting primarily blue-wing enhancements within regions of enhanced intensity. The subordinate line displayed primarily red-wing asymmetries with small kernels of blue wing asymmetry within the highest-intensity regions. The behaviour of velocities, intensities and linewidths is consistent with the behaviour found by Kerr et al. (2015) and Graham & Cauzzi (2015). Kerr et al. (2015) found blue-wing asymmetries within the Mg II k-line, but did not show the skew of the subordinate line. The magnitude and extent of the blue-wing enhancement found here is far larger, however, consistent with the scale of the event (Kerr et al. (2015) studied an M1.8 flare). Heinzel et al. (1994) observed blue-wing asymmetries in a variety of other chromospheric lines, and theorized that this asymmetry could be caused by downward-propagating plasma absorbing radiation from the red wing, causing the blue-wing to appear enhanced.

This could potentially explain the presence of blue wing asymmetry in the Mg II k-line that is absent or reversed in the subordinate triplet line. The Mg II h&k lines contain the well-studied Mg II $k/k_3$ component, a self absorption core at the center of the line. Shifts in the self-absorption core are well-studied, and

modelling in preparation of the *IRIS* launch suggested that the shifts in the self-absorption core are directly related to the velocity flows at the formation height of the Mg II k/$h_3$ component (Leenaarts et al. 2013b). The self-absorption core frequently disappears during flare observations. If, rather than disappearing, the core was redshifted to a greater extent than the bulk of the line, this could cause a significant blue-wing enhancement within the h&k lines. The subordinate triplet, which typically lacks this feature, would be unaffected, and the asymmetries in this line would be more sensitive to a superposition of flows. Heinzel et al. (1994) proposed the absorbing band in order to account for fast evolution of the blue wing asymmetry during initial stages. While the observations of the Mg II k line show blue-wing asymmetries over a longer time than proposed by Heinzel et al. (1994), it is worth noting both that the blue-wing asymmetries progress across the field of view, and are wholly contained within the duration of the nonthermal electron event.

This study combined detailed observations of a large number of distinct emission lines, resolving the energy injection event of a large flare across time, temperature, and space. This set of flare parameters combined a time-dependant electron injection profile with a time-dependant chromospheric response, including Doppler and nonthermal velocities, electron densities, and emission line intensities, with multiple rasters covering the nonthermal electron event. In addition to providing a detailed profile of this large solar flare, the derived parameters can be used to guide and interpret modeling of the atmosphere, using state-of-the-art hydrodynamic flare simulation codes, such as HYDRAD (Bradshaw & Mason 2003; Bradshaw & Cargill 2013), RADYN (Carlsson & Stein 1997; Allred et al. 2005, 2015), or FLARIX (Kašparová et al. 2009; Varady et al. 2010). Time-dependant

parameters of nonthermal electron energy injection from *RHESSI* would be used to provide the electron beam input. The chromospheric response across temperatures from $10^4$–$10^7$ K provides guidance for the correlation of simulation outputs. Together, this allows for both a deeper understanding of the dynamic response of the chromosphere to an impulsive injection of energy, as well as the ability to constrain the numerical simulations to the underlying physics.

# 5. HARD X-RAYS AS THE SOURCE OF SMALL-SCALE CHROMOSPHERIC BRIGHTENINGS

The existence of quasi-periodic fluctuations intrinsic to solar flares is well-established, and has been observed in lightcurves at a variety of wavelengths (Nakariakov & Melnikov 2009; Wang et al. 2000, 2003; Asai et al. 2001; Kliem et al. 2002; McAteer et al. 2005, 2007; Melnikov et al. 2005; Jackiewicz & Balasubramaniam 2013; Brosius & Daw 2015). Of particular note are fluctuations in the H$\alpha$ 6563Å line, which has been known to be particularly sensitive to nonthermal processes (Canfield et al. 1984; Canfield & Gayley 1987). Previous observations have found nonthermally-driven oscillations evident in the H$\alpha$ profile for a variety of flares (Wang et al. 2000, 2003; McAteer et al. 2005; Jackiewicz & Balasubramaniam 2013; Radziszewski et al. 2011). In general, the blue wing of H$\alpha$ provides the greatest sensitivity to nonthermal processes, as it is uncontaminated by thermal processes (unlike the core of the line) or downflows driven by chromospheric condensation (unlike the red wing of the line). While the wings of the Ca II 8541Å line are known to have similar features to the H$\alpha$ line, albeit with morphological differences (Watanabe et al. 2011; Vissers et al. 2013), high cadence observations are somewhat rarer for this line. In this chapter, we link the timing and oscillatory signatures of HXR peaks with corresponding bursts in the lower solar atmosphere to reveal the fundamental locations of HXR energy deposition.

## 5.1. Observations and Data Reductions

For this study, data were selected from the DST Service Mode archive. Between January 2013 and October 2014, three service mode campaigns were con-

ducted with the *IBIS*, *FIRS*, and *ROSA* instruments. Care was taken to standardize the instrumental setups, available filters and spectral lines, and calibrations between service mode dates. Of the service mode data obtained, three dates were selected for use in this study; 2013-10-17, 2013-10-26, 2014-10-26[1]. A fourth dataset, 2014-10-25 was considered for its coverage of an X-class flare, however, the final cadence was determined to be too slow for the purposes of this project. These dates were selected to contain *IBIS* scans of either the H$\alpha$ or Ca II 8542Å spectral lines with high cadence. Additional requirements applied were adequate seeing and weather stability, and pointing that captured an active region with flare-driven HXR emission observed by *RHESSI*. These conditions, as a result, exclude datasets where *IBIS* was operated in its polarimetric mode, as no polarimetric observations approach the required cadence. A summary of the *IBIS* data can be found in Table 5.1, and a description of *IBIS* data and reductions can be found in Section 5.1.1. *ROSA* data were used in the analysis of the 2013-10-17 dataset. A summary of *ROSA* data can be found in Table 5.2, and a description of their calibration can be found in Section 5.1.2. The final instrument used was the *RHESSI* spacecraft. Extensive discussion of *RHESSI* data techniques can be found in Chapters 2.1 and 4.2.1. Specific information pertaining to this project can be found in Section 5.1.3. Figures 5.1 and 5.2 show context images of the studied regions, as well as the availability of *RHESSI* and *IBIS* data and the SXR flux within the time range of interest. Figure 5.3 shows the *IBIS* wavelength modulation schemes used on each date.

[1]Context movies can be found at the following links
2013-10-17: `https://youtu.be/nqmMszm_e-Q`
2013-10-26: `https://youtu.be/meT-kdgiGAo`
2014-10-26: `https://youtu.be/zo6Xl75_AZQ`

Table 5.1: *IBIS* Data Summary

| **Date:** | **2013-10-17** | **2013-10-26** | **2014-10-26** |
|---|---|---|---|
| **NOAA AR:** | 11861 | 11882 | 12192 |
| **Start Acq. (UT):** | 14:33 | 16:25 | 15:25, 18:55 |
| **Stop Acq. (UT):**[a] | 19:00 | 17:53 | 17:58, 20:53 |
| **Pointing:**[b] | S8.1 W60.2 | S7.5 E54.2 | S14.7 W36.3 |
| **Projection Angle:** | 60.7° | 53.8° | 40.9° |
| **Spectral Line:** | Ca II 8542Å | Ca II 8542Å | H$\alpha$ |
| **Scan Positions:** | 3 | 11 | 3 |
| **Consecutive Scans:**[c] | 1 | 1 | 50 |
| **Cadence:** | 0.434–0.470 s | 1.8 s | 0.1/8.7 s[d] |
| **PI:** | K. Radziszewski | Y. Xu | R.T.J. McAteer |
| **Cotemp. *ROSA*:** | 4170ÅCont.<br>Ca II K 3934Å<br>G-Band 4305Å<br>H$\beta$ 4861Å | 4170ÅCont.<br>Ca II K 3934Å<br>G-Band 4305Å<br>H$\beta$ 4861Å | 4170ÅCont.<br>3500ÅCont.<br>G-Band 4305Å |

[a]Due to various limitations, the instruments were not operated continuously within this time span

[b]At start of series

[c]Number of times the same wavelength position was observed consecutively.

[d]First value is for consecutive repetitions, second is between filter repeats

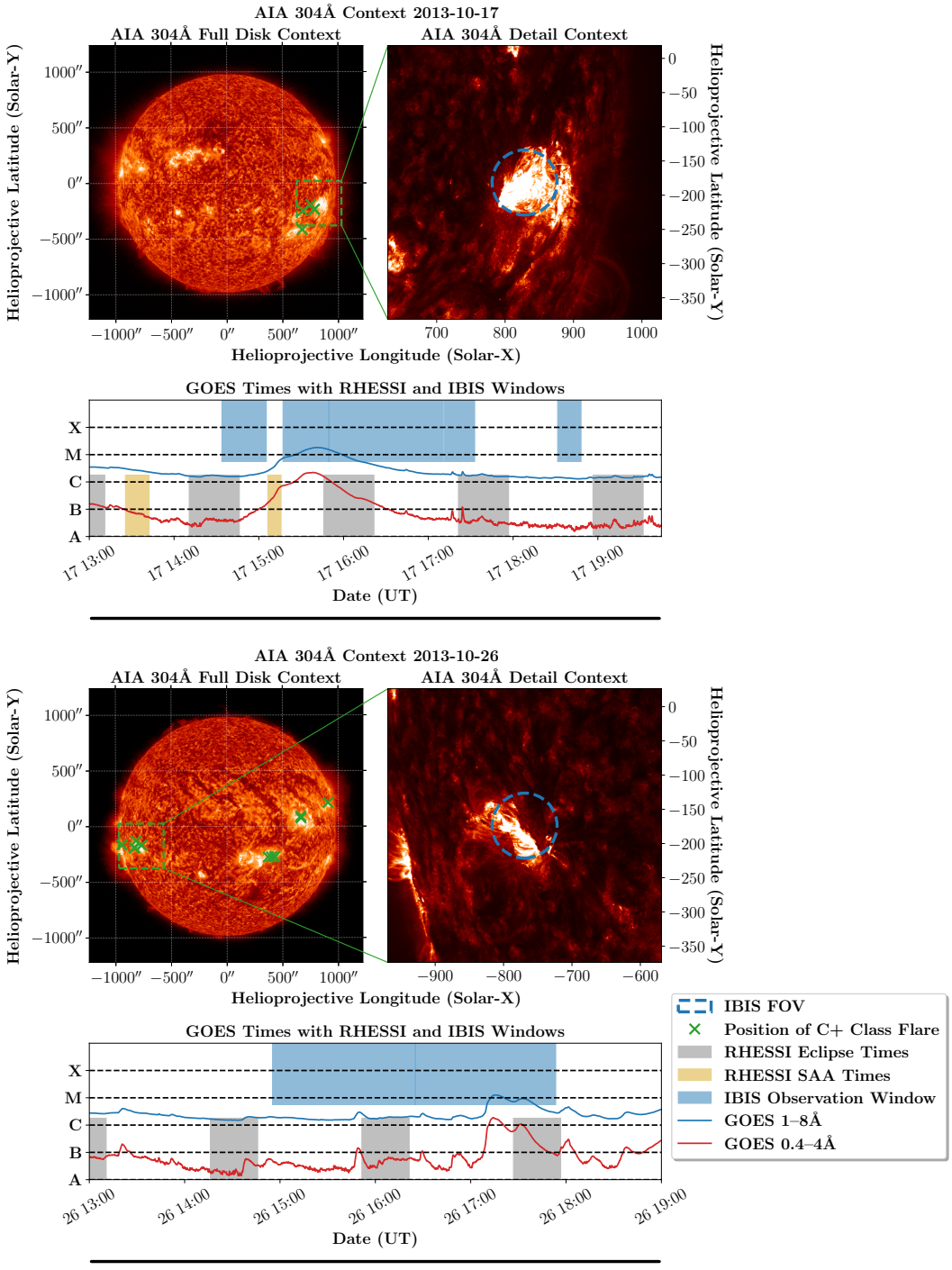


Fig. 5.1.— Overview of Observations from 2013-10-17 and 2013-10-26. Context for the *IBIS* field-of-view is shown from the *AIA* 304Å band. Known flare positions of C-class or greater are shown in green "x" marks. *GOES* SXR flux is shown alongside observation windows from *RHESSI* and *IBIS*.

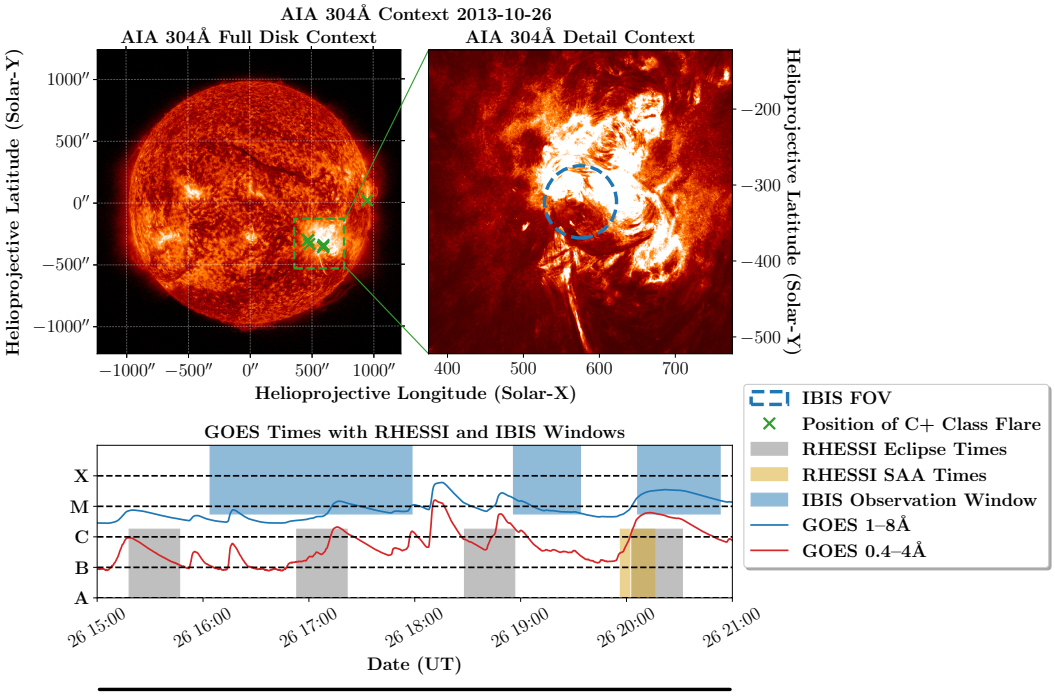


Fig. 5.2.— Overview of Observations from 2014-10-26. Context for the *IBIS* field-of-view is shown from the *AIA* 304Å band. Known flare positions of C-class or greater are shown in green "x" marks. *GOES* SXR flux is shown alongside observation windows from *RHESSI* and *IBIS*.

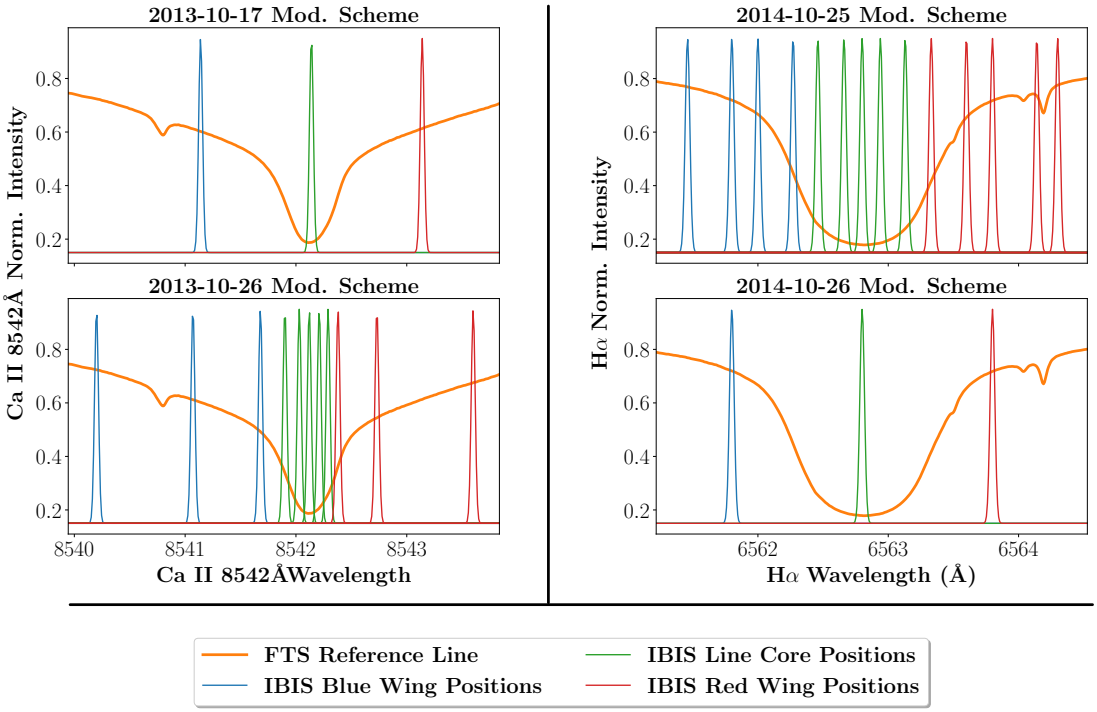


Fig. 5.3.— The wavelength modulation schemes used by *IBIS* on each of the three dates studied.

*IBIS* calibrations were carried out using a modified version of the standard pipeline, originally provided and made available by the NSO. For the datasets obtained on 2013-10-17 and 2014-10-26, modifications were made to the gain and blueshift modules. As these dates contained only three wavelength locations, the typical calibration step of fitting a polynomial to the line core is no longer valid. As the original code propagates the wavelength shift calibrations and gain corrections as one step, the reductions code required minor modification to utilize the gain maps in the final calibration steps without a wavelength correction component. As the wavelength correction affects the field-of-view, these datasets do display

an uncorrected FOV variation that cannot be easily corrected.

The IBIS pipeline does not correct for the prefilter transmission curve. The prefilter curve is most visible in the depressed intensities of spectral line wings, a result of the narrowband filters used between etalons in order to select only relevant modes. Typically, this step is carried out by dividing the spectral profile from flat-field measurements against the Fourier Transform Spectrometer (FTS) atlas from the McMath-Pierce telescope at Kitt Peak National Observatory (Kurucz et al. 1984). *IBIS* flat field imaging is typically performed at Sun-center, with the AO modulated to provide nearly-constant illumination onto the detector. The choice was made for these data not to utilize this correction. For the 2013-10-17 and 2014-10-26 datasets, the lack of a blueshift correction calls into question the validity of the prefilter correction, and for the purposes of this study, the prefilter correction is of little consequence. Rather than comparing the spectral profiles of various features, the time-variations of each filter position is of primary interest. Unfortunately, without this crucial step, full radiometric calibrations cannot be performed. All *IBIS* data are therefore given in units of DN/s, corrected for known factors, such as light-level variations, and normalized by regions of quiescent emission.

*IBIS* data were not processed using speckle-burst reconstruction techniques (Wöger & von der Lühe 2007, 2008), as this processing step would result in an unacceptable loss of cadence. First-order seeing corrections were carried out using a kernel destretch algorithm formed from the running mean of *IBIS*' cotemporal broadband images. Residual effects of seeing on image quality were characterized from the final broadband images using Helmli and Scherer's mean (the HSM), described by Helmli & Scherer (2001). Popowicz et al. (2017) identified this

technique as providing an excellent metric for the relative seeing quality across a wide variety of seeing conditions, in both active regions and quiet granulation. The HSM of a given image is:

$$HSM(x,y) = \begin{cases} \frac{\mu(U(x,y))}{g(x,y)}, \text{ if } \mu(U(x,y)) > g(x,y) \\ \frac{g(x,y)}{\mu(U(x,y))}, \text{ otherwise} \end{cases} \tag{5.1}$$

where $\mu(U(x,y))$ is the mean of the pixels in the neighborhood of the pixel $(x,y)$, and $g(x,y)$ is the value of pixel $(x,y)$. As a given image converges towards a constant value, the HSM for the frame approaches 1. Conversely, as the image quality improves, and smaller-scale features are apparent, the HSM decreases. This metric is not perfect, as it is less-sensitive to the effects of seeing on chromospheric structures, and the presence of clouds can artificially lower the value of the HSM, as dark noise dominates the signal in the frame. For the *IBIS* data used in this work, adequate seeing is defined as having a value of the HSM between $0.9 < HSM < 0.985$.

### *5.1.2. ROSA Data*

High-cadence *ROSA* data were obtained for 2013-10-17. While *ROSA* data exist for the other dates studied, storage and reduction time requirements were prohibitive for the scope of the project. The 2013-10-17 dataset was selected for further study by the combination of excellent seeing conditions, the highest average cadence with the *IBIS* instrument, and the presence of several HXR events associated with the active region. *ROSA* data were reduced using standard dark and flat field techniques. In order to remove the residual effects of seeing, and

Table 5.2: *ROSA* Data Summary

| **2013-10-17** | **GBand** | **4170Å Cont.** | **Ca II K** | **H$\beta$** |
|---|---|---|---|---|
| **Acquisition Start (UT):** | 14:42:10[a] | 14:33:47 | 14:33:47 | 14:33:47 |
| **Acquisition End (UT):** | 18:48:12 | 18:48:12 | 18:48:12 | 18:48:12 |
| **Camera Name:** | DAS1 | DAS2 | DJCCam | HARDCam |
| **Array Size:** | 1002×1004 | 1002×1004 | 512×512 | 512×512 |
| **Frames/File:** | 256 | 256 | 4095 | 4095 |
| **Exposure Time:** | 17 ms | 16 ms | 30 ms | 90 ms[b] |
| **Camera Framerate (Hz):** | 30.3 | 30.2 | 16.5 | 8.3 |
| **Speckle Burst No.:** | 64 | 64 | 39 | 39 |
| **Final Cadence (s):** | 2.11 | 2.12 | 2.37 | 4.69 |

[a]Earlier iterations failed

[b]UBF used, low throughput

restore *ROSA* data to near-diffraction limited resolution, speckle burst reconstructions were carried out using the KISIP code (Wöger & von der Lühe 2007, 2008). The number of sequential images used in the reconstruction were chosen to provide a $\approx 2$ second cadence for 4170Å, g-band, and Ca K data. As H$\beta$ images were obtained using the Universal Birefringent Filter (UBF) (Beckers 1973), which has a low throughput when compared to a traditional narrowband filter, a $\approx 2$ second final cadence could not be safely achieved, and the burst number was selected for a more modest 4.7 second cadence. Destretch calibrations were carried out after speckle reconstruction.

### *5.1.3. RHESSI Data*

*RHESSI* data reductions were carried out in a manner similar to the method described in Chapter 4.2.1. Spectra were obtained for each individual detector that was determined to have adequate remaining sensitivity. This subset of detectors

necessarily varies between datasets. For the two datasets in 2013, detectors 1, 3, 4, 5, 6, 7, 8, and 9 were used. For the two datasets in 2014, detectors 1, 3, 6, 8, and 9 were used. Spectrum and SRM files for each detector were retrieved with a 0.5 second cadence. Lightcurves were formed from the spectrum files by binning energy levels to the desired widths. Three bins with a width of 5 keV (10–15 keV, 15–20 keV, 20–25 keV) and three with widths of 10 keV (10–20 keV, 15–25 keV, 20–30 keV) were created for each date. Additional energy bins were formed for 2014-10-25 and 2014-10-26, which contained larger (M+) class events spanning the 25–50 keV bins. Background levels were determined using the high energy bins as a template for the orbital background variation as described in Chapter 4.2.1.

Attenuator states were curated to remove certain discontinuous states from the final lightcurves. During large events, a combination of thin or thick attenuators are moved in front of the *RHESSI* detectors in order to reduce the effects of pileup. However, as the event progresses, the instrument will periodically remove one or both attenuators for a short time (4 seconds) in order to determine whether the current attenuator configuration is the best available for the event. This results in sharp, discontinuous jumps in the count rate. For the purposes of this study, these intervals were removed. While corrections for attenuator state changes exist, they are not a perfect characterization of the pileup effect, which can only be determined via detailed spectral fitting outside the scope of this study. As this project is concerned with timing and subsecond variation of the HXR peaks, these gaps can be safely ignored. Likewise, semi-accurate photometric calibrations require spectral fitting. Final lightcurves are expressed as counts/second/detector for reasons of precision.

Once individual detectors were corrected for background and attenuator state changes, emission was summed across detectors to improve the count statistics of the light curve. At this stage there was still significant scatter in the time series measurements owing to the degradation of the *RHESSI* instrument combined with the short cadence. In order to minimize scatter in the time series, two different methods were used to denoise the lightcurves. The first, a simple running median with a time window of 4 seconds was deemed adequate, and has the advantage of preserving count rate errors. The second technique employed Fourier deconvolution of small-amplitude signals, and is less prone to deletion of small scale fluctuations, and additionally allowed the removal of signals with a period of 4 seconds, corresponding spatial sensitivity effects from the spacecraft's rotation. Both were used in analysis of extracted burst events.

### *5.1.4. Data Alignment*

Spatial alignment of ground-based data is a nontrivial process owing to the high resolution and small field-of-view of the instruments used. Aligned data were produced by first aligning the highest-quality *IBIS* continuum image (as determined from the HSM) with a cotemporal *AIA* image. *AIA* 1700Å images are used for this step, and pointing corrections are carried out using the aiapy Python package. Pointing information from the DST is used as an initial guess, and images are fine-aligned by cross-correlation. The design of the DST precludes the need for derotation. Once the relative offset of *AIA* and *IBIS* is established, the pointing of the DST is determined by calculating the differential rotation across the observation time interval at the position on this disk. The rotation

rate is determined from the `solar_rotate_coordinate` function available within the SunPy `physics.differential_rotation` subpackage. Once the coordinates of each *IBIS* frame were determined, alignment was visually checked for the first and last image in the sequence with acceptable seeing quality. At this step, *ROSA* data were aligned to the 2013-10-17 dataset from the Air Force target images obtained with both *ROSA* and *IBIS*. Alignment of the target images provides the relative orientation and offset of the *ROSA* cameras. After this step, the data is considered aligned. The accuracy of this technique is within $1.5''$, the approximate spatial resolution of *AIA* 1700Å images.

## 5.2. Analysis Methods

The size of the datasets analyzed in this work necessitates automation at every step. The *IBIS* and *ROSA* datasets represent approximately 1.5 TB when discarding raw and intermediate datasets and cover approximately 120 minutes at a cadence of 2 seconds for *ROSA*, and 0.4 seconds for *IBIS*. When intermediate steps, such as the pre-destretch *IBIS* images or the post-speckle *ROSA* images, are considered (which cannot be safely discarded due to inconsistencies with the reduction pipelines), the data used in this work reaches a size of 12TB.

The extraction and tracking of burst-like sources was the major target for automation. To this end, we expanded a preexisting automated detection algorithm, developed by Vissers et al. (2013) and based on constraints set by Watanabe et al. (2011). Specific applications of the algorithm have been used for Ellerman bomb detection in UV bands by Vissers et al. (2015) and Vissers et al. (2019). The code developed for this project attempted to generalize and expand the algorithm de-

scribed in these works, with a generalized source extraction and tracking algorithm as the final product[2]. The algorithm consists of the following constraints.

1. *Brightness:* Similar to Vissers et al. (2013), this step applies a double intensity threshold to a given data frame. The user defines the lower and upper thresholds (typically a multiple of the frame mean). The algorithm creates an image mask that contains the contours of sources that are above the lower threshold that contain emission above the upper threshold.

2. *Size:* The user additionally defines minimum and maximum allowed source sizes. The maximum source size becomes important when tracking, e.g., flare ribbons, which the algorithm is easily able to do. Sources from the previous step that do not meet the minimum size are eliminated from the mask. If any sources are above the maximum size, the user is prompted to revise either the maximum size or the threshold parameters. Additionally, the user is able to artificially expand the size of every source found in the mask. This is helpful for eventual tracking, as larger sources are more easily tracked when seeing conditions are less than optimal.

3. *Continuity:* In order to minimize the RAM usage of the algorithm when applied to large data sets, the necessary results of the previous steps can be saved to the disk. This is usually not necessary, as the required parameters for the next steps are minimal. Sources found within a 42GB data set can be contained within 25MB. Once the entire data set has been processed for the first two constraints, the tracking algorithm begins. The user defines

[2]Code available at `https://github.com/sgsellers/vissers_algorithm`

a window, corresponding to a number of frames. The algorithm iterates through the dataset and checks for overlaps between the source contours in each new frame and the source contours found within the window.

4. *Source Sorting:* Sources in each successive frame can be propagated into the database the algorithm is building as one of four categories:

    - The simple continuation of one prior source to one continuing source
    - The cutoff where the source is no longer found to be active
    - The product of a split event, where one event already in the database overlaps with two or more sources in the new frame. The largest of the "daughter" sources is propagated as the continuation of the original, while the remainders are entered into the database as new entries.
    - The result of a merge event, where two or more parent events within the database bother overlap with a single source in the new frame. The largest parent is propagated through, and the smaller are discontinued.
    - A fringe case where two or more parents match with two or more daughters. In practice, this tends to occur when a recently propagated split event is still within the user defined window, and the products of the split event are still within the original parent's footpoint. In this case, the daughter events are propagated according to size.

    In practice, split and merge events are rare for most burst events, though in the cores of Ca II 8542Å and H$\alpha$ they are somewhat more common.

5. *Curation:* A final argument to the tracking function finally curates the database and prunes events shorter than the user-defined length.

Once sources were extracted using the above algorithm, the results were examined for correlations between the flux extracted as part of a burst-like event and the HXR lightcurve obtained from *RHESSI*. When possible, wavelet analysis was carried out on the fast temporal variations of the burst events, using standard method described by Torrence & Compo (1998). For the 26 October, 2014 dataset, wavelet analysis could not be carried out, due to the nature of the *IBIS* modulation scheme on that date. Wavelet analysis requires a continuous dataset, and while each individual 50-exposure image set is continuous, the 8 second gap between successive repetitions of each filter is impossible to interpolate across in a realistic way.

## 5.3. Burst Correlation Results

### *5.3.1. 17 October, 2013*

For the dataset on 17 October 2013, the *IBIS* instrument was operated with three spectral positions covering the blue wing, core, and red wing of the Ca II 8542Å line. The pointing of the telescope was focused on NOAA AR 11861, though the pointing was adjusted midway throughout the observation series to different locations within the same active region. During the times observed by the DST, *RHESSI* recorded two significant events in the 15–25 keV lightcurve that were confirmed by imaging to be cospatial with the *IBIS* FOV and coincident with adequate seeing at the telescope. The first event peaked at 15:31 UT and corresponded to an M1.6 flare. The second was significantly smaller, and occurred in the aftermath of the first, with a peak around 16:44 UT. Any SXR enhancement for this second event was obscured by the decay phase of the M1.6 flare.

Source extraction was carried out for all three wavelengths of the Ca II 8542Å line, as well as the Ca K and H$\beta$ lines, which were observed simultaneously with *ROSA*. Sources were curated to last for at least 4 seconds, with the exception of H$\beta$, for which 8 seconds were required due to the lower cadence at this wavelength.

Figure 5.4 shows the response of Ca II 8542Å Ca II K, and H$\beta$ during the larger HXR event associated with the M-flare. Very little direct response to this event was observed in any of the available ground-based metrics. While the lightcurve at the core of Ca 8542Å indicates that the event occurred within the frame, and *RHESSI* images place a source within the *IBIS* FOV, the post-flare ribbons were dynamically quiet, and few sources were recorded in the line wings. Only one source, within the red wing of Ca 8542Å was found to correlate with the HXR lightcurve, with an r-value $r = 0.581$. When the decay of this source is discounted, the r-value increases to $r = 0.63$. Additionally, this source exhibits peaks at 15:25:17 UT, 15:28:10 UT, and 15:29:10 UT, which correspond within 10 seconds to locations of smaller enhancements in the HXR lightcurve.

The second, smaller HXR event at 16:43 UT, conversely, exhibited several sources that were well-correlated to the HXR lightcurve. These are shown in Figure 5.5. A total of four events were found in the wings of Ca II 8542Å which showed correlation with the smaller 16:44 UT HXR event: two in the red wing of the line, and two in the blue wing. All four are located within $20''$ of each other, and each has an r-value, $r > 0.5$. The HXR lightcurve has three distinct peaks between 16:43–16:45 UT, and each of the sources exhibits the same behaviour. The weighted mean of these events was chosen for study via wavelet analysis. Weighting was determined from the median value of the respective filter positions.

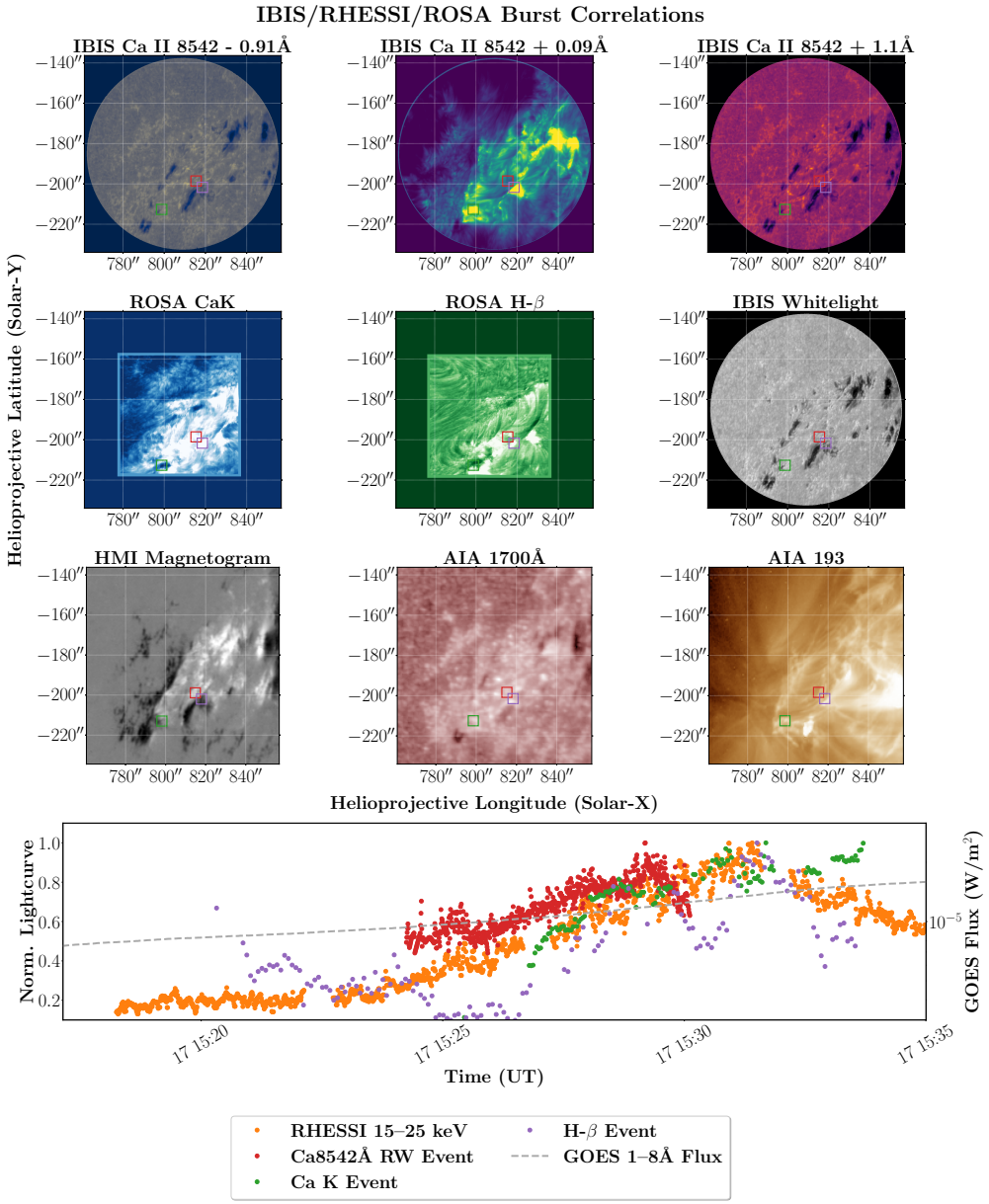


Fig. 5.4.— Detail from an HXR event on 17 October, 2013. Only one correlating event in the wings of Ca 8542Å was found. This event is marked by the red rectangle in all images, and its lightcurve is shown by the red points in the bottom row. The green event corresponds to a source in *ROSA* CaK, and the lilac event corresponds to *ROSA* H$\beta$.

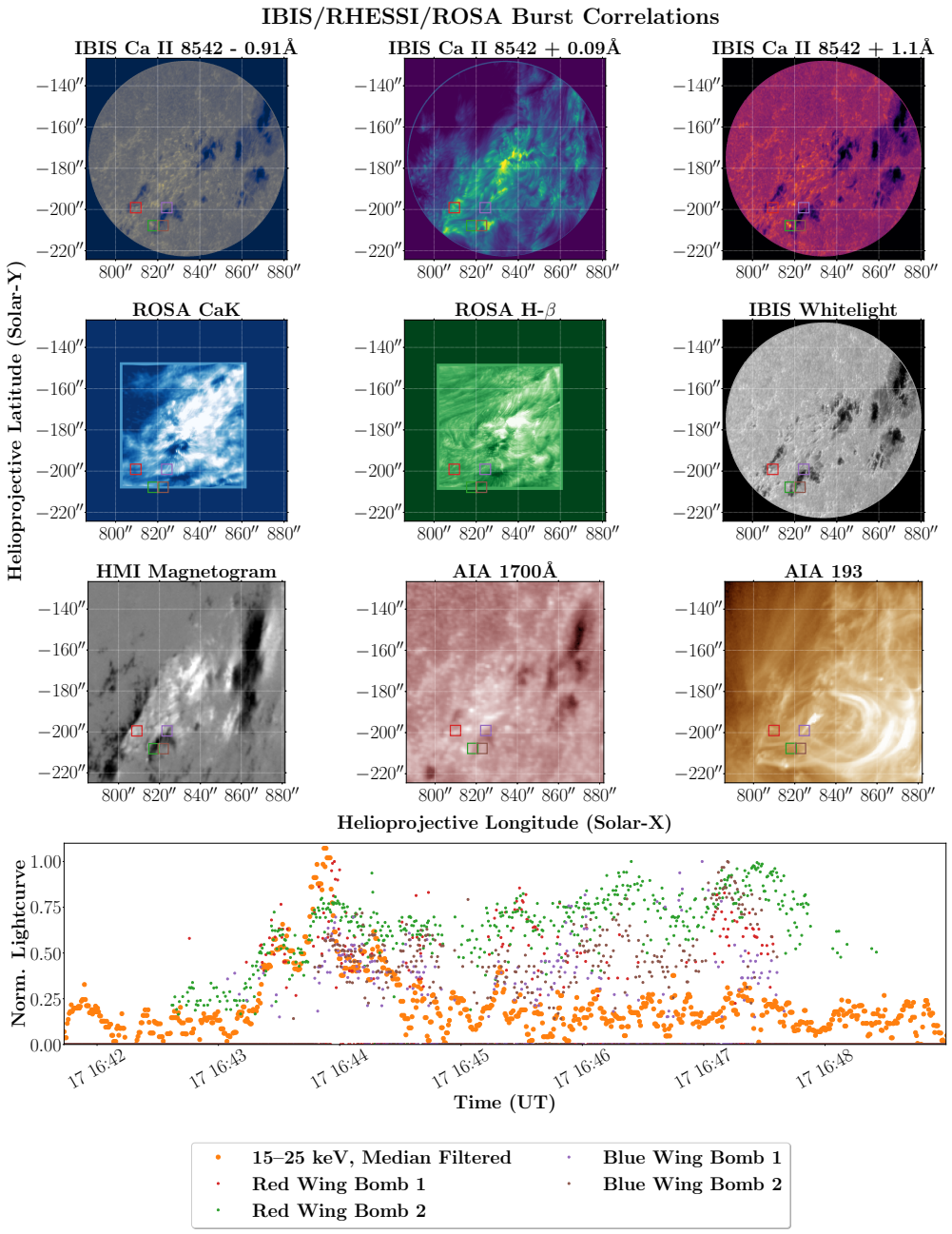


Fig. 5.5.— Detail from a small HXR spike on 17 October, 2013. Four sources in the red wing of Ca 8542Å were found to correlate with the time of all three sub-peaks in the HXR event. Each colored box on the solar images marks the location of the source corresponding to the color-matched lightcurves shown in the bottom row.

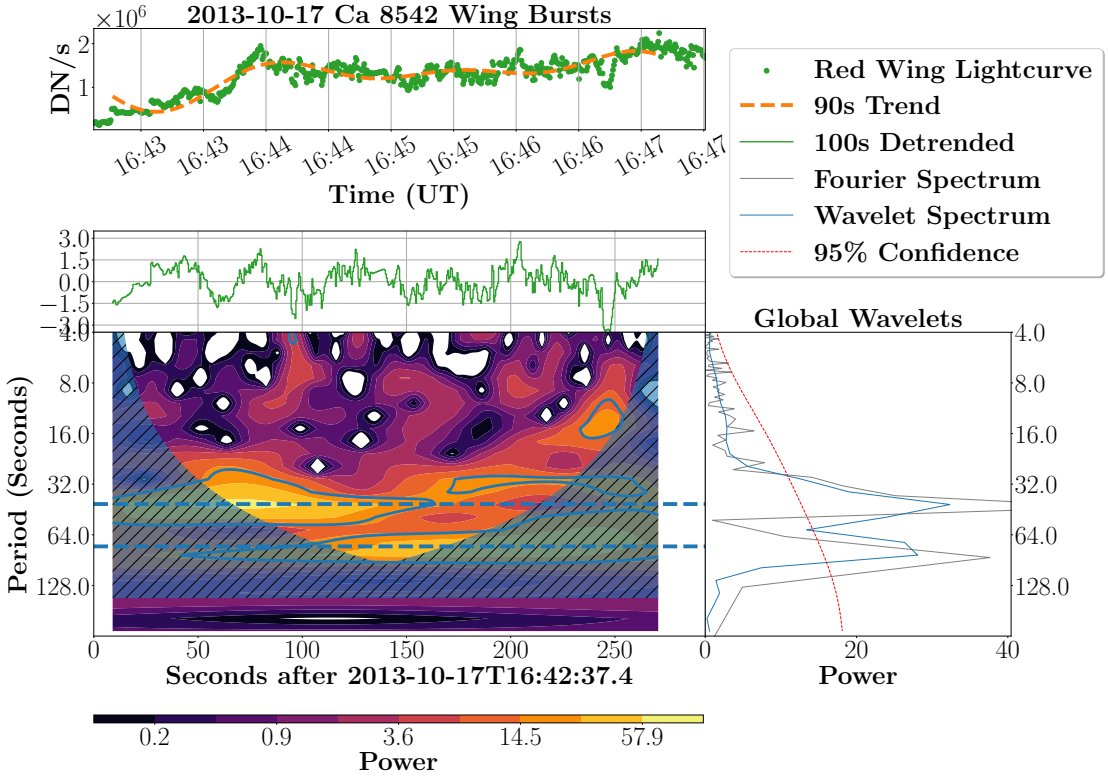


Fig. 5.6.— Wavelet analysis of the combination of sources shown in Figure 5.5. The top panel shows the combination of the four bursts shown in that figure. The dashed line is the periodicities above 90 seconds. The second panel shows the same lightcurve with those periodicities removed, while the bottom panel shown the wavelet analysis of that lightcurve. The hatched region denotes the cone of influence, while the blue contours outline the 95% confidence interval. Dashed blue lines denote regions of interest shared with Figure 5.7

The wavelet analysis for this combination of events is shown in Figure 5.6. Periodicities longer than 90 seconds were detrended from the combined lightcurve, and wavelet analysis techniques using a Morlet wavelet were applied to the detrended lightcurve. The same process was repeated for the HXR lightcurve over the same time range. The wavelet results for the HXR lightcurve are shown in Figure 5.7.

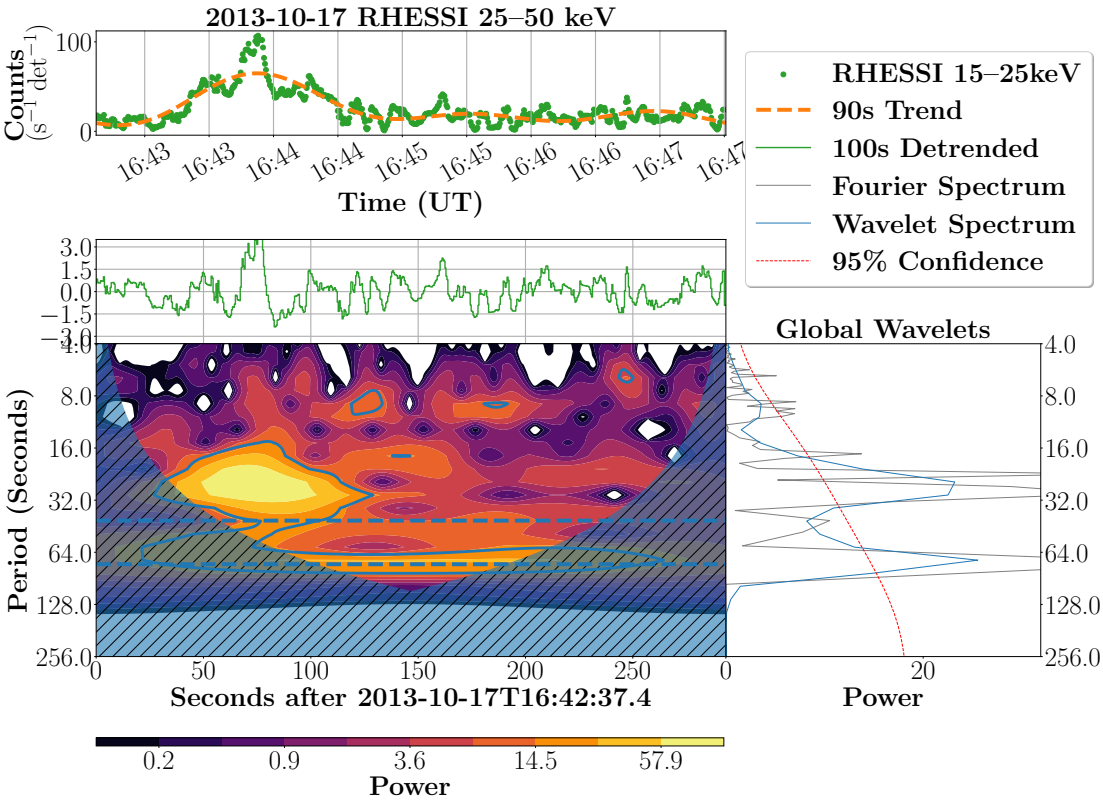


Fig. 5.7.— Wavelet analysis of the *RHESSI* lightcurve shown in Figure 5.5. The top panel shows the full lightcurve in green, with the dashed line denoting periodicities above 90 seconds. The second panel shows the same lightcurve with those periodicities removed, while the bottom panel shown the wavelet analysis of that lightcurve. The hatched region denotes the cone of influence, while the blue contours outline the 95% confidence interval. Dashed blue lines denote regions of interest shared with Figure 5.7

### *5.3.2. 26 October, 2013*

For the dataset on 26 October, 2013, the *IBIS* instrument was operated with eleven spectral positions covering the Ca II 8542Å with five spectral positions dedicated to fine coverage of the 0.25Å span on either side of the line core, and three positions for each the red and blue wing. The pointing was chosen to cover NOAA AR 11882, which had recently appeared around the eastern limb. During the range observed at the DST, *RHESSI* recorded two HXR events, a small event peaking at 16:49 UT with no associated *GOES* event, and a larger event at 17:13 UT corresponding to a C8.8 event recorded by *GOES*. Both events were confirmed via *RHESSI* imaging to have occurred within the *IBIS* FOV, however, seeing during the larger event was suboptimal and ensuing coverage inadequate.

Source extraction was carried out for all eleven scan positions for the Ca II 8542Åline. Sources were curated for 9 seconds. In general, core sources responded in an approximately-thermal manner, as expected for chromospheric sources. Little consistent variation was seen in the far wings of the line, though the number of detected sources increased by $\approx 20\%$ during small windows of adequate seeing corresponding to the larger HXR peak. Of the eleven scan positions, Ca II $8542 + 0.33/-0.37$Å scan positions showed the best response to HXR emission during the smaller event. The same scan positions showed significant response during the C8.8 flare, as did the Ca II $8542+0.68/-0.98$ positions, formed at a significantly lower height and corresponding primarily to photospheric emission. These positions correspond to a mix of photospheric and chromospheric emission, showing the footpoints of the overlying loop structure in great detail. Over half the sources tracked during the smaller HXR burst were found to cor-

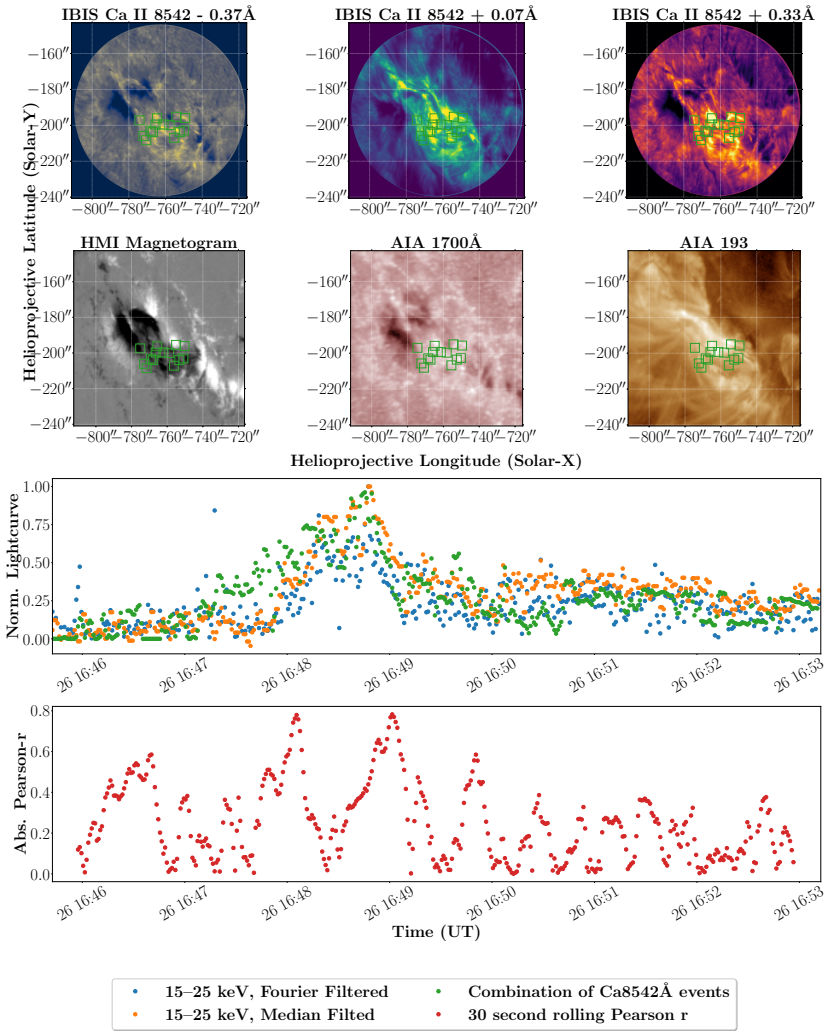


Fig. 5.8.— Detail from a small HXR spike on 26 October, 2013. Twelve sources in the near red wing of Ca 8542Å were found to correlate with the time of all four sub-peaks in the HXR event. Each green box on the solar images marks the location of the source corresponding to the green lightcurve shown in the third row. The fourth row shows the rolling Pearson correlation coefficient, as a first approximation of the correlation on fine temporal scales.

relate well with the HXR emission. The set of bursts that did not correlate well were either short-lived, with lifetimes just above the curation time, products of split events, or physically remote from the other sources. Uncorrelated events during the larger event were fewer, and typically could be attributed to facular brightening rather than flare kernel emission.

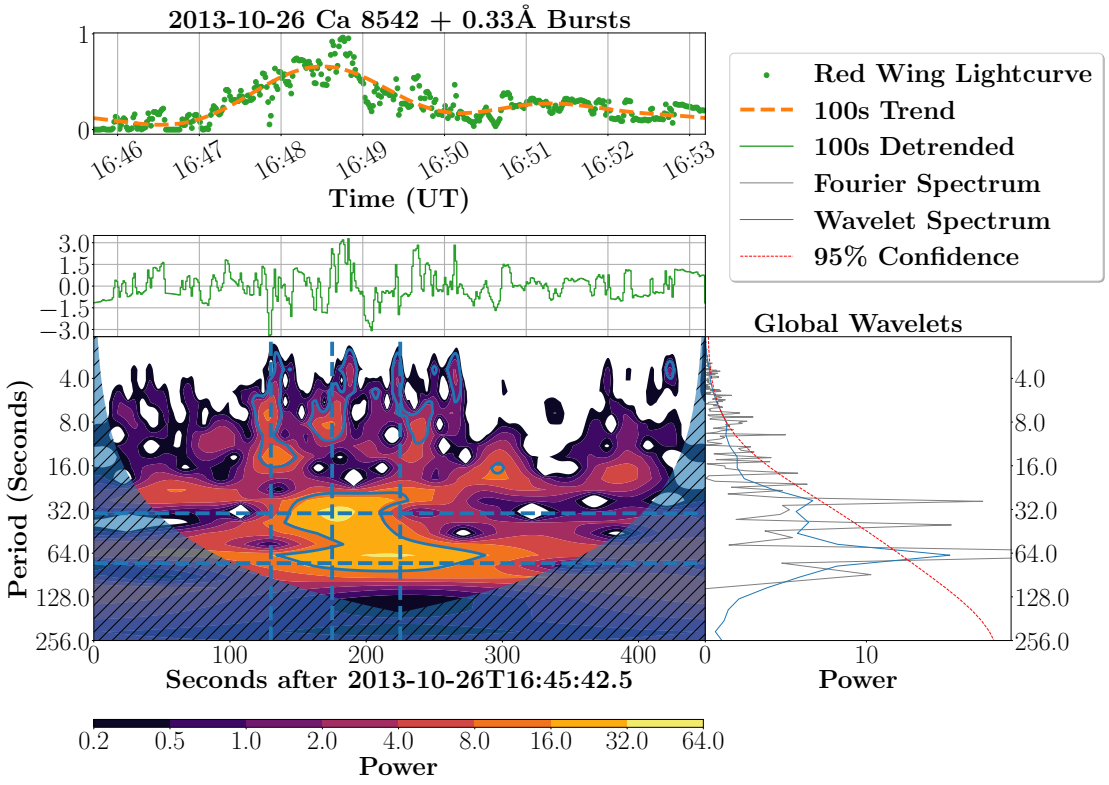


Fig. 5.9.— Wavelet analysis of the combination of sources shown in Figure 5.8. The top panel shows the combination of the twelve bursts shown in that figure. The dashed line is the periodicities above 100 seconds. The second panel shows the same lightcurve with those periodicities removed, while the bottom panel shown the wavelet analysis of that lightcurve. The hatched region denotes the cone of influence, while the blue contours outline the 95% confidence interval. Dashed blue lines denote regions of interest shared with Figure 5.8

Figure 5.8 shows the response in the Ca II 8542 + 0.33Å scan position during

the smaller HXR burst at 16:49 UT. The green boxes in the top row mark the locations of sources used to form the green lightcurve in the third row. The second row shows the locations of these sources in the context of a cotemporal *HMI* magnetogram and *AIA* filtergrams. All twelve sources are clustered near the center of the field of view, and correspond to the footpoints of emission observed in the line core. This combination of sources resulted in a correlation r-value of $r = 0.698$ between the combined lightcurve and HXR flux from 15–25 keV. A rolling application of the Pearson correlation coefficient found that the correlation between the lightcurves was highest during times when the slope of the HXR lightcurve was increasing, and while the dual peak present in the HXR lightcurve was also present in the combined Ca II 8542Ålightcurve, the demarcation was significantly less pronounced in the Ca II 8542Å lightcurve.

Wavelet analysis for this combination of events is shown in Figure 5.9. Periodicities longer than 100 seconds were detrended from the combined lightcurve, and a Morlet wavelet was applied to the detrended variations. The same process was repeated for the HXR lightcurve, the results of which are shown in Figure 5.10.

Wavelet analyses of these lightcurves showed significant similarities. During the HXR peak, both lightcurves revealed significant enhancements at 10 s, 34 s, and 75 s periodicities. The 75 s enhancement carry throughout the full 7 minutes studied, while the 34 s enhancement is present in both lightcurves for 100 s during the peak of HXR emission. The 10 s periodicity is present only for approximately 20 s during the flare peak. Overall, the oscillatory response of the two lightcurves display significant similarities, though much of the highest frequencies were obscured.

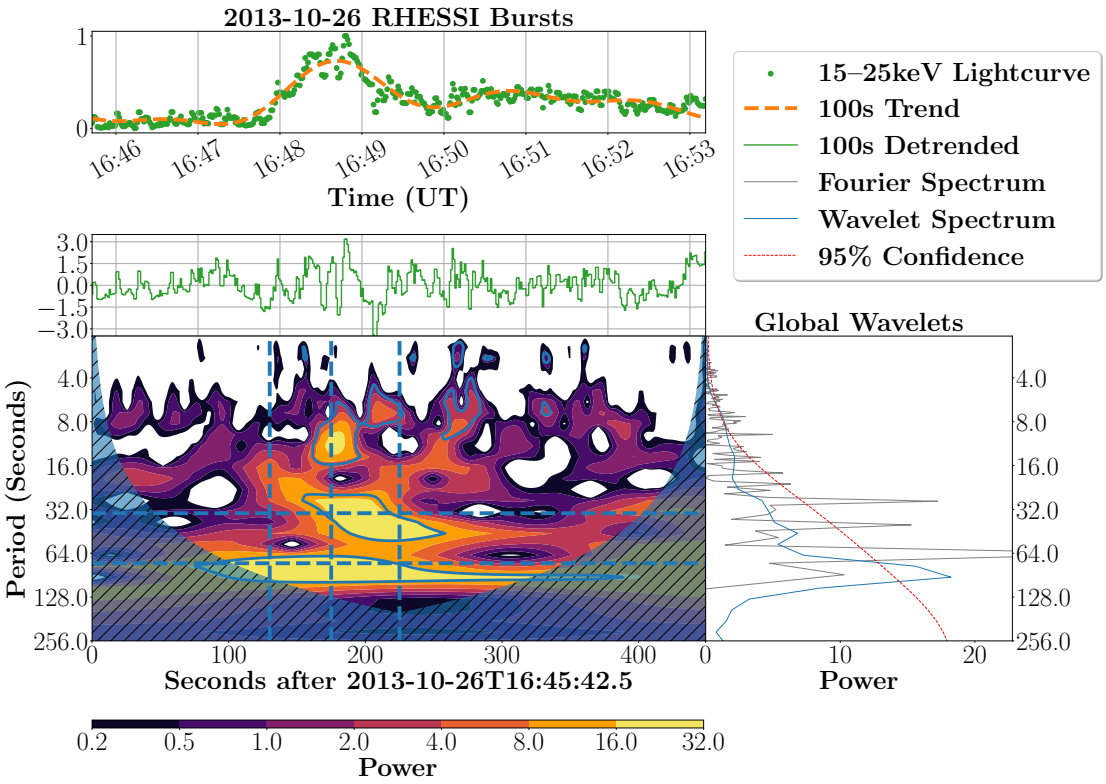


Fig. 5.10.— Wavelet analysis of the *RHESSI* lightcurve shown in Figure 5.8. The top panel shows the full lightcurve in green, with the dashed line denoting periodicities above 100 seconds. The second panel shows the same lightcurve with those periodicities removed, while the bottom panel shown the wavelet analysis of that lightcurve. The hatched region denotes the cone of influence, while the blue contours outline the 95% confidence interval. Dashed blue lines denote regions of interest shared with Figure 5.7

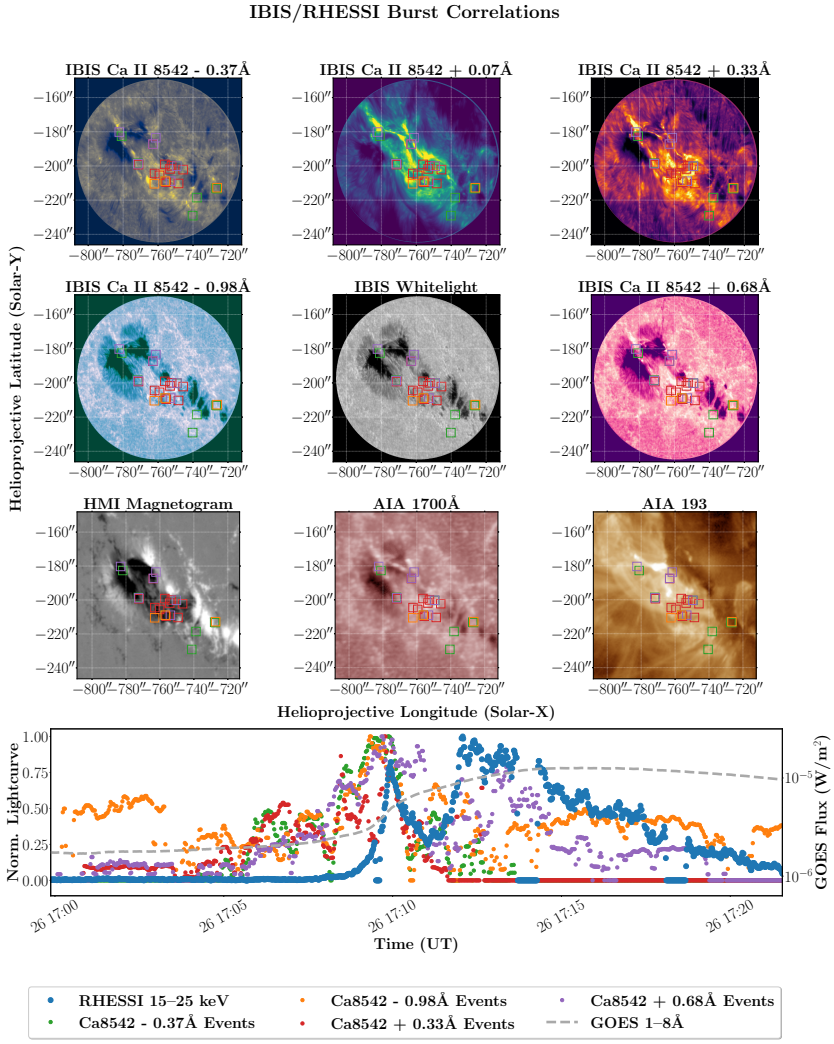


Fig. 5.11.— Examination of the C8.8 flare on 2013-10-26 on 26 October, 2013. Ten sources in the near red wing of Ca II 8542Å and eight in the blue wing show a peak time cotemporal with the first HXR spike at the start of the flare. Poor seeing obscured the larger HXR event, however, significant precursor activity is clear.

Figure 5.11 shows the response during the early impulsive phase of the C8.8 flare. The HXR emission displayed a characteristic double peak. The first coincided with a short period of excellent seeing, however observations during the second peak were mostly obscured. The first two rows show *IBIS* images taken early in the event. Boxes mark the approximate positions of sources extracted from the four line wing positions. All sources that were found to track the HXR emission fell along the line of sunspots, with most sources clustered between the two larger sunspot groups. This central cluster is found to lie in a region of significant flux cancellation from cotemporal *HMI* magnetograms, while the more remote sources were in strong unipolar regions. Many of the central cluster were associated with the locations of enhanced line core emission, however, none corresponded to the overlying arcade as determined from *AIA* imaging, cementing these sources as originating in the deep chromosphere. It is notable that the larger event was characterized by strong source correlations in the far wings of Ca II 8542Å. By contrast, the earlier HXR burst showed almost no enhancement in these scan positions, suggesting a difference in particle deposition depth, usually associated with a change in the electron distribution low-energy cutoff.

### *5.3.3. 26 October, 2014*

For the dataset on 26 October, 2014, the *IBIS* instrument covered the H$\alpha$ line with three spectral positions covering the far wings and line core. The telescope was pointed to NOAA AR 12192, which was one of the largest active regions of Solar Cycle 24, and extremely flare productive, with a total of 6 X-class events recorded, including one prior to the start observing on 2014-10-26. During the

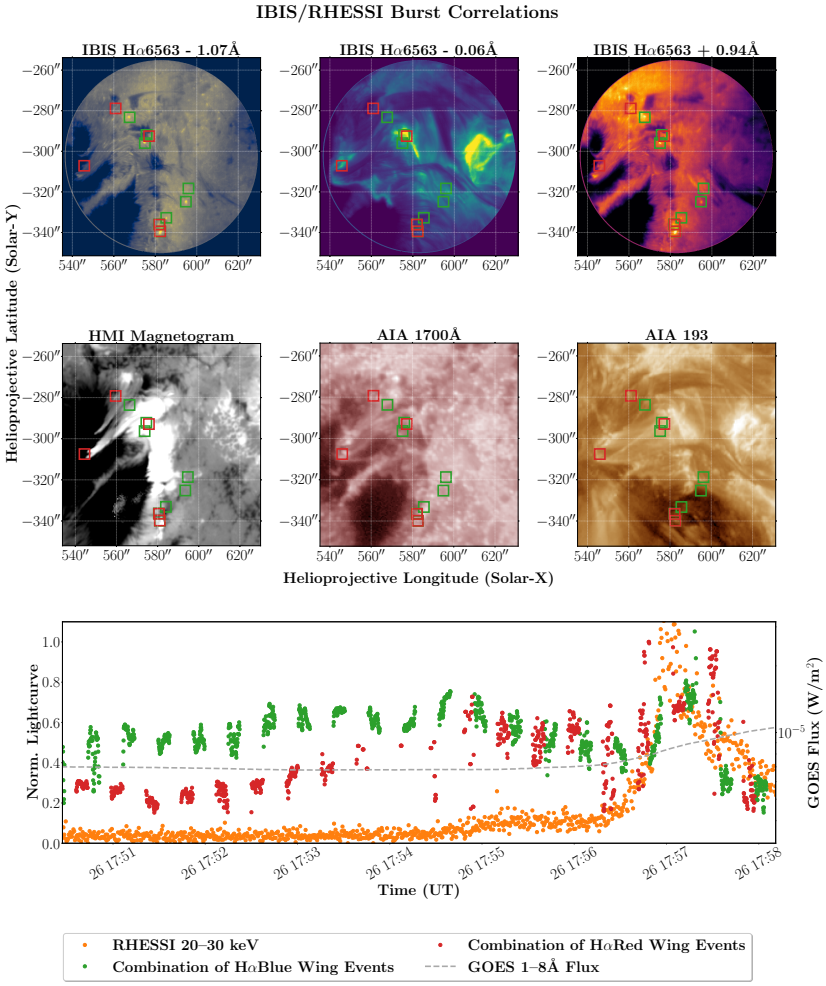


Fig. 5.12.— Detail from a HXR spike on 26 October, 2014. Five sources in the red wing and six in the blue wing of H$\alpha$ were found to correlate with the 20–30 keV HXR lightcurve. The HXR lightcurve is characterized a small enhancement beginning at 17:54:30 UT, with an impulsive peak at 17:57 UT. The boxes overlaid on the top two rows of images correspond with the locations of blue-wing flare kernels (green) and red-wing kernels (red).

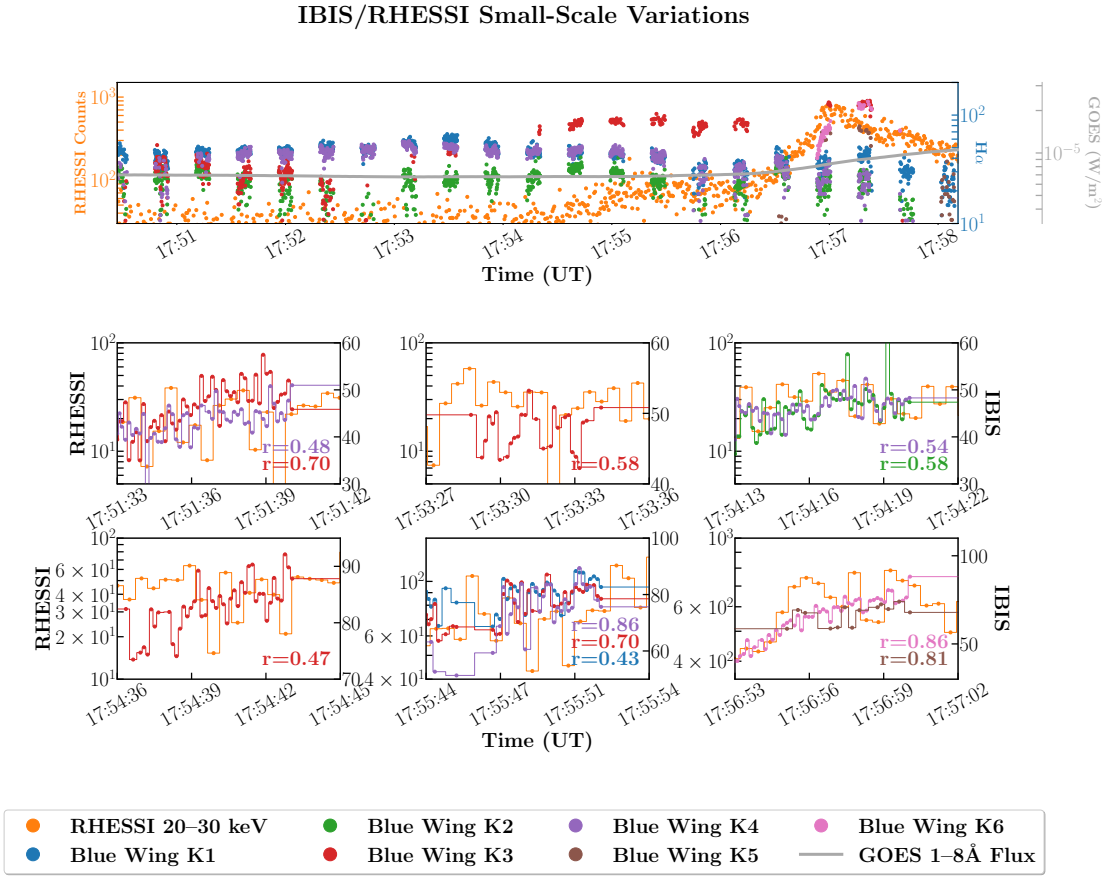


Fig. 5.13.— Detail of H$\alpha$ blue wing sources during the HXR event on 2014-10-26. The top row shows the lightcurve during the HXR event, while the smaller plots show selected 50-exposure series for the displayed H$\alpha$ kernels.

observing period, *RHESSI* recorded several events, including a C7.8 flare which peaked at 17:59. Variable seeing, an integration time which proved inadequate to capture the red wing sufficiently, and a wavelength-dependant variation across the FOV which could not be corrected as there was insufficient wavelength coverage to fit the line core made this dataset insufficient to characterize the red-wing behaviour of H$\alpha$, and resulted in low coverage of the blue-wing. Additionally, the large gap between successive image series makes wavelet analysis impossible to carry out for this date.

Figure 5.12 shows the response in the wings of H$\alpha$ to the start of the C7.8 flare impulsive event. During the event, the response in the red wing is varied. Overall, the red wing enhancements track the HXR response, however, the short-timescale variations are affected by seeing and low signal, showing a large scatter in individual 50-exposure series. The blue wing emission tracks the large-scale changes in the lightcurve, and selected kernels show good correlation with HXR emission on short timescales. Figure 5.13 shows the six kernels in the blue wing of H$\alpha$ that best track the HXR emission. Of particular note are the correlations found after 17:54 UT, corresponding to the bottom row of the plot, as the HXR counts begin to climb and are tightly correlated with several kernels of emission. It was found that a 2 second offset between the H$\alpha$ emission and HXR emission allows for the best behaviour at subsecond scales, consistent with findings from Wang et al. (2000) and Radziszewski et al. (2011).

## 5.4. Discussion

In total, three dates with high-quality observations yielded five HXR bursts that are correlated with response in the wings of the chromospheric H$\alpha$ and Ca II 8542Å lines. During the HXR events, most (more than 50% in all cases) of the active burst-like events were found to have some measure of correlation with the HXR light curve. Of the events that did not correlate, a common reason was the accidental inclusion of facular brightenings, which remained a problem in studies of Ellerman bombs by Vissers et al. (2013).

With the exception of the M1.6 flare on 17 October, 2013, several sources were found for all other events that were well-correlated with the corresponding HXR lightcurve, exhibiting peaks cotemporal to the HXR peaks, and behaviour consistent with the lightcurve evolution. In the Ca II 8542Å line, red-wing sources were found to be more abundant and better correlated with the HXR emission. While many sources found in the red wing of the line appear in the blue wing as well, they are significantly dimmer in the blue wing, and are frequently below the threshold of the extraction algorithm. From the 26 October, 2014 dataset, the red wing of the line at Ca II 8542 + 0.33Åand 8542 + 0.68Å showed the best correlations with the HXR emission. Both scan positions show a mix of photospheric and chromospheric structures. The +0.33Å images show the low-lying flare ribbon and energy deposition regions, while brightenings at +0.68Å are far more compact, and correspond spatially to the footpoints of the ribbons themselves.

The H$\alpha$ data seem to show better correlations in the blue wing of the line, however, a number of factors predominately affected the red wing observations,

resulting in a large amount of scatter in the extracted sources. During the period of heightened HXR emission, correlation between the fluxes of certain individual kernels was and HXR flux was high, with a peak correlation value, $r = 0.86$ from 17:56:53–17:57:02 UT. This mirrors results from Wang et al. (2000), who were also able to discern subsecond correlations in the wing of H$\alpha$, but were mismatched on the precise timing of the HXR peaks with respect to the H$\alpha$ response.

Combining multiple sources that each exhibited some measure of correlation to the HXR event yielded the best match between source peaks and HXR peaks, suggesting that rather than being deposited into two flare ribbons, the electrons are able to precipitate into the lower atmosphere. No individual kernel carries the full HXR signature, and it is instead shared between multiple nonthermal electron deposition sites. This is partially confirmed by comparing the wavelet analyses of the HXR lightcurve and chromospheric lightcurve. Both HXR emission (Asai et al. 2001) and flare kernel emission (McAteer et al. 2005) are known to harbor QPP signals, however, this dataset is uniquely suited to compare the two on short timescales.

Wavelet analyses for the small event on 2013-10-17 show matches between the Ca II 8542Å kernels and the 15–25 keV emission. Particularly, significant enhancements in power are observed with a periodicity of 72 s that spans the full duration 300 s duration. A partial match is evident at 37 s, particularly below the 95% confidence interval in the HXR lightcurve. Another 32 s periodicity is enhanced through the latter half of the flare. Shorter periods are observed to match in the latter half of the event, however, the short periods are obscured through much of the first half of the Ca II kernel lightcurve.

Wavelet analysis of the 2013-10-26 event shows the match between the two in greater detail. Again, a longer period variation at 70 s is evident in both lightcurves across the event duration, and a match between 25–55 s is found at the $\approx$ 130 s mark. Around the HXR event peak at 180 s, a matched periodicity between 5–16 seconds is found in both lightcurves. The match in periodicities implies that the Ca II 8542Å red wing is responding directly to small-scale fluctuations in HXR power. The timing match in both the 8542Å line and H$\alpha$ further confirms that the extreme low chromosphere can be thought to respond directly to HXR burst event, and may be though of as the site of elementary bursts in the HXR event. This conclusion is supported by Wang et al. (2000), McAteer et al. (2005), McAteer et al. (2007), and Radziszewski et al. (2011), and was first predicted for H$\alpha$ by Canfield & Gayley (1987). As the combination of sources is required to fully reproduce the HXR lightcurve, this is further evidence for episodic electron acceleration, as predicted by Asai et al. (2001) and McAteer et al. (2007).

Notably, the kernel profiles shown in Chapter 5.3 exhibit little ($t < 5$s) to no delay with respect to the HXR profile. This delay is far shorter than found by Radziszewski et al. (2011). It is notable that many of the HXR events studied here are of small magnitude and short duration. The time delays found by Wang et al. (2000); Radziszewski et al. (2011); Falewicz et al. (2017) occur in larger events, with corresponding *GOES* emission. The smaller low-atmosphere bursts found here may be signatures of a far smaller arcade of loops, with a proximate reconnection region. The detected bursts are found to correlate even in the extreme wings of Ca II 8542Å and H$\alpha$, suggesting an extremely low deposition layer. The red wing of Ca II 8542Å is nearly photospheric in height. Stark broadening

makes the determination of the line formation height nontrivial without detailed inversions, however, observations of Ca II 8542Å during the 2013-10-26 dataset showed the HXR signature persisting through several wavelengths in the red wing. This, combined with the lack of time delay points to significant energy deposition in extremely low atmospheric layers cotemporal with emission typically attributed to grand loop footpoints. The compact sizes of these structures indicates that, even in extremely small HXR events, some population of electrons is able to propagate to the deepest atmospheric layers, either being channeled by the magnetic field, or through an already low-lying reconnection layer. An alternate, more esoteric explanation involves the elusive proton beam, most famously championed by Švestka (1970). Indeed, more recent models indicate that electron beams deposit energy primarily at the upper edge of the chromosphere Procházka et al. (2018). This is an assumption furthered by observations in this very document; Chapter 4 finds the FRT to be an energy deposition layer, with characteristic temperatures in the millions of Kelvin. A proton beam, conversely, is free to penetrate to the low atmosphere, being a candidate for whitelight flare emission. In these observations, with extremely low-atmospheric energy signatures simultaneous with HXR emission (i.e., with the deposition of electrons in the upper atmosphere), a population of accelerated protons are a strong candidate for the energetic driver. The chromosphere is a thick target, but a thin atmospheric layer, and the extended travel time is negligible.

Further work is needed to explore the broader implications of this work. Radiometric calibration of these observations should place limits on the radiated energy budget. These limits are expected to vary with the low-energy nonthermal electron cutoff, and will be higher for larger electron cutoffs. Detailed *RHESSI*

analysis including spectral fitting will provide further context. *ROSA* data in the chromosphere can assist in tracking the thermal response to the event.

A future project coordinating DKIST observations and DST observations could prove especially useful. DKIST provides unparalleled spatial and spectral resolution, however, the combination of mosaicing in the Visible Broadband Imager (VBI, Wöger et al. (2021)) and the requirement of onsite speckle reconstructions results in a slower cadence than would be ideal. The addition of further DST observations, particularly making use of the UBF with the newer 2k×2k *ROSA* cameras would allow flexibility to increase the cadence and FOV in select spectral lines higher than DKIST could otherwise obtain. Simultaneous observations from the *STIX* instrument aboard Solar Orbiter would provide the HXR coverage needed.

# 6. CONCLUSIONS AND FUTURE WORK

The investigations detailed within this document used a multi-instrument, multi-wavelength approach to describe and quantify the effects of nonthermal energy deposition upon the solar atmosphere. The most dramatic effects of solar flares, including hot EUV loop formation, are visible for minutes to hours in the wake of an event but the conditions that lead to these more obvious signatures are short-lived and decided in the seconds to minutes after the energy injection event. Monitoring the response of the solar atmosphere in these crucial moments is vital to understanding the energy signature, deposition, and efficiency of the flare process. The combinations of instruments used throughout these studies allowed assembly and application of a holistic viewpoint for the flaring atmosphere.

The goal of Chapter 4 was to investigate the evolution of chromospheric plasma throughout the duration of, and in the immediate aftermath of, a temporally resolved nonthermal electron injection event produced by a solar flare. Utilizing high-quality spectroscopic observations in the HXR from the *RHESSI* spacecraft, a model of the electron beam profile was constructed with a 16 second cadence. HXR imaging of the event was inadequate to constrain the area of the footpoints as a proxy for the cross-sectional area affected by electron injection. The decision was made instead to rely on slit-jaw imaging from the *IRIS* spacecraft, which observed spectral bands dominated by C II and Mg II emission throughout the flare with minimal detector saturation. The resulting electron beam profile, at its peak had an energy flux of $3.07 \pm 0.34 \times 10^{11}$ erg s$^{-1}$ cm$^{-2}$, with a shallow distribution ($\delta < 6$), and an extremely high value found for the low-energy cutoff ($E_c > 30$ keV during the HXR peak). This implies that the electrons

are able to deposit large amounts of energy even in extremely low atmospheric layers.

The effects of electron deposition across the EUV and UV atmosphere were studied using the *EIS* and *IRIS* instruments in Chapter 4.3.2–4.3.5. EUV emission line spectra from *EIS* were used to characterize the properties of the explosive chromospheric evaporation associated with this event. The flow reversal temperature did not vary with time after the flare onset, nor was it significantly different from FRT's found by other studies, suggesting that the FRT appears to be very nearly constant. The FRT also marked a delineation in nonthermal widths and a significant density enhancement. The *IRIS* instrument confirmed the condensation-flow response of the cooler chromosphere, and placed the Fe XXI line in context of *EIS* observations. *IRIS* observations additionally hinted at small-scale variations that were obscured by the comparatively-low resolution of *EIS*. *EIS* observations of extremely hot ions (Fe XXIII and Fe XXIV) showed complex profiles dominated by several significantly blueshifted components. *IRIS* observations of the Mg II line showed structures containing a blue asymmetry, commonly theorized to be the result of preferential absorption from a downward-propagating plasma absorbing emission from the red-wing of the line.

Chapter 5 sought to investigate the fine-scale structure of the chromosphere to connect short-timescale HXR variations to their atmospheric counterparts. Archival datasets featuring the *IBIS* instrument, formerly mounted at the Dunn Solar Telescope, were searched to find three datasets that had high-cadence observations of the Ca II 8542Å or H$\alpha$ chromospheric lines. These observations were processed to extract lightcurves for small-scale brightenings in the wings of these lines. The constructed lightcurves were compared to HXR lightcurves from

*RHESSI*, searching for correlations that could provide clues as to the locations of energy deposition. Four of the five HXR bursts studied were found to have some measure of correlation between chromospheric brightenings and the HXR lightcurve, and wavelet analyses were applied to two of these events to highlight overlaps in the periodic structures of these events. While individual brightenings were not found to correlate particularly well with the full HXR lightcurve, combinations of events yield good correlations. This can be considered to be a hallmark of episodic magnetic reconnection depositing elementary bursts of nonthermal electrons into the lower solar atmosphere.

## 6.1. Future Work

These assembled datasets have the potential to uncover more about the partition of flare energy throughout the solar atmosphere. The work outlined in Chapter 4 is an ideal starting point for detailed hydrodynamic modelling and validation of flare code results. There is also significant latitude available to re-examine several assumptions made throughout the chapter, all predicated on the base assumption of a Maxwellian distribution within the plasma. Analysis using a kappa-type distribution, as pursued by Dzifčáková et al. (2018) for another X-class flare, would allow the construction of a differential emission measure, updated formation temperatures, and updated density diagnostics that may clarify the atmospheric conditions post-flare. Analysis of the periodic behaviour driven by this flare would be of interest as well, searching particularly for the presence and locations of 3-minute oscillations within the available array of instrumentation, similar to analyses by Farris & McAteer (2020) and Milligan et al. (2017).

The datasets studied in Chapter 5 are also ideal for further investigation. A detailed analysis of available *ROSA* data would be valuable for determining an approximate height profile of various features observed in the *IBIS* datasets. Analysis of NUV data from *AIA* 1600Å and 1700Å channels may prove useful, however, whether these channels have adequate cadence or resolution remains to be seen. As mentioned in Chapter 5.4, a coordinated study combining the spatial resolution available to DKIST and the flexibility with regards to cadence and instrumentation available to the DST would allow not only coordinated time series, but also detailed atmospheric inversions on extremely small scales. There may also be significant utility in an examination of the spectrum of the active region as a whole, in the context of not one spectral line but the full solar spectrum. Observations of the shape of the continuum, and response in the myriad of other spectral lines populating the solar spectrum are rare. When combined with other, well-studied spectral lines such as those presented here, these rarer observations have potential to realize the goal of observing the flare as a connected event.

Of course, the ideal followup would be to combine all of the observations detailed within this work to create a truly holistic picture of a solar flare from the photosphere to the corona. This could be accomplished with adequate planning (and luck) with available tools. HXR observations are becoming available from the STIX instrument aboard Solar Orbiter, allowing (with some reduced capacity) the construction of time-resolved electron beam parameters. The *IRIS* and *EIS* instruments continue to produce high-quality spectra, and the suite of available ground-based instrumentation has never been more varied in sheer utility. These types of holistic observations, performed for flares of different magnitudes and energies would allow a previously unimaginable ability to parameterize and

understand flares as a class of events. The next several years will usher in the rise of Solar Cycle 25, and also the tools and instrumentation necessary to further untangle the long-standing problem of the dynamics and particulars of the complicated and varied event known as the solar flare.

Were this accomplished, the plasma could once again be considered well-behaved.

## REFERENCES


Abbett, W. P., & Hawley, S. L. 1999, ApJ, 521, 906

Allred, J. C., Hawley, S. L., Abbett, W. P., & Carlsson, M. 2005, The Astrophysical Journal

Allred, J. C., Hawley, S. L., Abbett, W. P., & Carlsson, M. 2005, ApJ, 630, 573

Allred, J. C., Kowalski, A. F., & Carlsson, M. 2015, ApJ, 809, 104

Asai, A., Shimojo, M., Isobe, H., Morimoto, T., Yokoyama, T., Shibasaki, K., & Nakajima, H. 2001, ApJ, 562, L103

Aschwanden, M. J. 2007, ApJ, 661, 1242

Aschwanden, M. J., Kontar, E. P., & Jeffrey, N. L. S. 2019, ApJ, 881, 1

Bamba, Y., Lee, K.-S., Imada, S., & Kusano, K. 2017, ApJ, 840, 116

Battaglia, M., Motorina, G., & Kontar, E. P. 2015, ApJ, 815, 73

Beckers, J. M. 1973, in Bulletin of the American Astronomical Society, Vol. 5 (American Astronomical Society), 269

Benz, A. 2002, Plasma Astrophysics, second edition, Vol. 279 (Kluwer Academic Publishers, Dordrecht, Netherlands)

Benz, A. O. 2017, Living Reviews in Solar Physics, 14, 2

Berghmans, D., et al. 2021, A&A, 656, L4

Bong, S.-C., Lee, J., Gary, D. E., & Yun, H. S. 2006, ApJ, 636, 1159

Bornmann, P. L. 1999, in The many faces of the sun: a summary of the results from NASA's Solar Maximum Mission., ed. K. T. Strong, J. L. R. Saba, B. M. Haisch, & J. T. Schmelz, 301

Bradshaw, S. J., & Cargill, P. J. 2013, ApJ, 770, 12

Bradshaw, S. J., & Mason, H. E. 2003, A&A, 401, 699

Brannon, S., & Longcope, D. 2014, ApJ, 792, 50

Brosius, J. W. 2013, ApJ, 762, 133

Brosius, J. W., & Daw, A. N. 2015, Astrophysical Journal

Brosius, J. W., & Phillips, K. J. H. 2004, The Astrophysical Journal

Brown, J. C. 1971, Solar Physics

Brown, J. C., Emslie, A. G., & Kontar, E. P. 2003, ApJ, 595, L115

Bryans, P., Young, P. R., & Doschek, G. A. 2010, ApJ, 715, 1012

Cai, Q., Shen, C., Raymond, J. C., Mei, Z., Warmuth, A., Roussev, I. I., & Lin, J. 2019, MNRAS, 489, 3183

Cameron, R. H., Dikpati, M., & Brandenburg, A. 2017, Space Sci. Rev., 210, 367

Canfield, R. C., & Gayley, K. G. 1987, The Astrophysical Journal

Canfield, R. C., Gunkler, T. A., & Ricchiazzi, P. J. 1984, ApJ, 282, 296

Carlsson, M., & Stein, R. F. 1997, ApJ, 481, 500

Carmichael, H. 1964, in The physics of solar flares, Vol. 50 (NASA Special Publications, Washington DC), 451

Carrington, R. C. 1859, MNRAS, 20, 13

Cavallini, F. 2006, Sol. Phys., 236, 415

Choithani, V., Jain, R., Awasthi, A. K., Singh, G., Chaudhari, S., & Sharma, S. K. 2018, Research in Astronomy and Astrophysics, 18, 121

Cowling, T. G. 1953, in The Sun, ed. G. P. Kuiper (The University of Chicago Press, Chicago), 532

Culhane, J. L., et al. 2007, Sol. Phys., 243, 19

De Pontieu, B., et al. 2014, Sol. Phys., 289, 2733

Del Zanna, G. 2013, A&A, 555, A47

Del Zanna, G., Mitra-Kraev, U., Bradshaw, S. J., Mason, H. E., & Asai, A. 2011, A&A, 526, A1

Dennis, B. R., & Pernak, R. L. 2009, ApJ, 698, 2131

Dere, K. P., Landi, E., Mason, H. E., Monsignori Fossi, B. C., & Young, P. R. 1997, A&AS, 125, 149

Dere, K. P., Zanna, G. D., Young, P. R., Landi, E., & Sutherland, R. S. 2019, The Astrophysical Journal Supplement Series, 241, 22

Ding, M. D., Fang, C., & Huang, Y. R. 1995, Sol. Phys., 158, 81

Doschek, G. A. 1983, Solar Physics

Doschek, G. A., & Warren, H. P. 2005, ApJ, 629, 1150

Doschek, G. A., Warren, H. P., Mariska, J. T., Muglach, K., Culhane, J. L., Hara, H., & Watanabe, T. 2008, ApJ, 686, 1362

Doschek, G. A., Warren, H. P., & Young, P. R. 2013, ApJ, 767, 55

Doschek, G. A., et al. 2007, ApJ, 667, L109

Dzifčáková, E., Zemanová, A., Dudík, J., & Mackovjak, Š. 2018, ApJ, 853, 158

Ellerman, F. 1917, ApJ, 46, 298

Emslie, A. G. 1978, ApJ, 224, 241

Falewicz, R., Radziszewski, K., Rudawy, P., & Berlicki, A. 2017, ApJ, 847, 84

Farris, L., & McAteer, R. T. J. 2020, ApJ, 903, 19

Fisher, G. H. 1989, ApJ, 346, 1019

Fisher, G. H., Canfield, R. C., & McClymont, A. N. 1985, The Astrophysical Journal

Fletcher, L., et al. 2011, An observational overview of solar flares

Gary, G. A. 2001, Sol. Phys., 203, 71

Giovanelli, R. G. 1947, MNRAS, 107, 338

Gough, D. O. 1981, Sol. Phys., 74, 21

Graham, D. R., & Cauzzi, G. 2015, ApJ, 807, L22

Graham, D. R., Fletcher, L., & Hannah, I. G. 2011, Astronomy and Astrophysics

Hale, G. E. 1908, ApJ, 28, 315

Hara, H., Watanabe, T., Harra, L. K., Culhane, J. L., Young, P. R., Mariska, J. T., & Doschek, G. A. 2008, ApJ, 678, L67

Harra, L. K., Matthews, S. A., Long, D. M., Doschek, G. A., & De Pontieu, B. 2014, ApJ, 792, 93

Harra, L. K., Williams, D. R., Wallace, A. J., Magara, T., Hara, H., Tsuneta, S., Sterling, A. C., & Doschek, G. A. 2009, ApJ, 691, L99

Hawley, S. L., & Fisher, G. H. 1994, ApJ, 426, 387

Heinzel, P., Karlicky, M., Kotrc, P., & Svestka, Z. 1994, Sol. Phys., 152, 393

Helmli, F., & Scherer, S. 2001, in ISPA 2001. Proceedings of the 2nd International Symposium on Image and Signal Processing and Analysis. In conjunction with 23rd International Conference on Information Technology Interfaces (IEEE Cat. (IEEE), 188–193

Hirayama, T. 1974, Sol. Phys., 34, 323

Hodgson, R. 1859, MNRAS, 20, 15

Holman, G. D., et al. 2011, Space Sci. Rev., 159, 107

Hoyle, F. 1949, Some recent researches in solar physics. (Cambridge University Press, Cambridge)

Hurford, G. J., et al. 2002, Sol. Phys., 210, 61

Jackiewicz, J., & Balasubramaniam, K. S. 2013, ApJ, 765, 15

Jaeggli, S. A., Lin, H., Mickey, D. L., Kuhn, J. R., Hegwer, S. L., Rimmele, T. R., & Penn, M. J. 2010, Mem. Soc. Astron. Italiana, 81, 763

Jess, D. B., Mathioudakis, M., Christian, D. J., Keenan, F. P., Ryans, R. S. I., & Crockett, P. J. 2010, Sol. Phys., 261, 363

Jones, C. A., Thompson, M. J., & Tobias, S. M. 2010, Space Sci. Rev., 152, 591

Kamio, S., Kurokawa, H., Brooks, D. H., Kitai, R., & UeNo, S. 2005, ApJ, 625, 1027

Kašparová, J., Varady, M., Heinzel, P., Karlický, M., & Moravec, Z. 2009, A&A, 499, 923

Kerr, G. S., Allred, J. C., & Polito, V. 2020, ApJ, 900, 18

Kerr, G. S., Carlsson, M., Allred, J. C., Young, P. R., & Daw, A. N. 2019, ApJ, 871, 23

Kerr, G. S., Simões, P. J. A., Qiu, J., & Fletcher, L. 2015, A&A, 582, A50

Kliem, B., Dammasch, I. E., Curdt, W., & Wilhelm, K. 2002, ApJ, 568, L61

Kontar, E. P., Jeffrey, N. L. S., & Emslie, A. G. 2019, ApJ, 871, 225

Kopp, R. A., & Pneuman, G. W. 1976, Sol. Phys., 50, 85

Krucker, S., et al. 2008, A&A Rev., 16, 155

—. 2020, A&A, 642, A15

Kuhar, M., Krucker, S., Martínez Oliveros, J. C., Battaglia, M., Kleint, L., Casadei, D., & Hudson, H. S. 2016, ApJ, 816, 6

Kurucz, R. L., Furenlid, I., Brault, J., & Testerman, L. 1984, Solar flux atlas from 296 to 1300 nm (National Solar Observatory, Sunspot, New Mexico)

Lee, K.-S., Imada, S., Watanabe, K., Bamba, Y., & Brooks, D. H. 2017, The Astrophysical Journal, 836, 150

Leenaarts, J., Pereira, T. M. D., Carlsson, M., Uitenbroek, H., & De Pontieu, B. 2013a, ApJ, 772, 89

—. 2013b, ApJ, 772, 90

Lemen, J. R., et al. 2012, Sol. Phys., 275, 17

Li, D., Ning, Z. J., & Zhang, Q. M. 2015, Astrophysical Journal, 813

Li, Y., Ding, M. D., Qiu, J., & Cheng, J. X. 2015, ApJ, 811, 7

Lin, R. P., et al. 2002, Sol. Phys., 210, 3

Longcope, D. W. 2014, ApJ, 795, 10

Mariska, J. 2016, EIS Software Note No. 20: EIS/AIA Coalignment, Tech. rep., George Mason University, College of Science

Mariska, J. T. 1992a, The Solar Transition Region (Cambridge University Press)

—. 1992b, Cambridge Astrophysics Series, 23

Massa, P., Schwartz, R., Tolbert, A. K., Massone, A. M., Dennis, B. R., Piana, M., & Benvenuto, F. 2020, ApJ, 894, 46

Mathioudakis, M., McKenny, J., Keenan, F. P., Williams, D. R., & Phillips, K. J. H. 1999, A&A, 351, L23

McAteer, R. T. J., Young, C. A., Ireland, J., & Gallagher, P. T. 2007, ApJ, 662, 691

McAteer, R. T. J., et al. 2005, ApJ, 620, 1101

Melnikov, V. F., Reznikova, V. E., Shibasaki, K., & Nakariakov, V. M. 2005, A&A, 439, 727

Miesch, M. S. 2005, Living Reviews in Solar Physics, 2, 1

Milligan, R. O. 2011, ApJ, 740, 70

—. 2015, Sol. Phys., 290, 3399

Milligan, R. O., & Dennis, B. R. 2009, Astrophysical Journal, 699, 968

Milligan, R. O., Fleck, B., Ireland, J., Fletcher, L., & Dennis, B. R. 2017, ApJ, 848, L8

Milligan, R. O., Gallagher, P. T., Mathioudakis, M., & Keenan, F. P. 2006, The Astrophysical Journal

Milligan, R. O., Gallagher, P. T., Mathioudakis, M., Keenan, F. P., & Bloomfield, D. S. 2005, MNRAS, 363, 259

Milligan, R. O., & Ireland, J. 2018, Sol. Phys., 293, 18

Milligan, R. O., et al. 2014, ApJ, 793, 70

Nakariakov, V. M., & Melnikov, V. F. 2009, Space Sci. Rev., 149, 119

Narayan, R., & Nityananda, R. 1986, ARA&A, 24, 127

Neupert, W. M. 1968, The Astrophysical Journal

Newton, E. K., Emslie, A. G., & Mariska, J. T. 1995, ApJ, 447, 915

Ortiz, A., Hansteen, V. H., Nóbrega-Siverio, D., & Rouppe van der Voort, L. 2020, A&A, 633, A58

Parker, E. N. 1957, J. Geophys. Res., 62, 509

Pereira, T. M. D., Carlsson, M., De Pontieu, B., & Hansteen, V. 2015, ApJ, 806, 14

Peter, H. 2010, A&A, 521, A51

Peter, H., et al. 2014, Science, 346, 1255726

Petschek, H. E. 1964, in NASA Special Publication, Vol. 50 (National Aeronautics and Space Administration, Science and Technical Information Division), 425

Phillips, K. J. H. 1995, Guide to the Sun (Cambridge University Press)

Phillips, K. J. H., Chifor, C., & Dennis, B. R. 2006, ApJ, 647, 1480

Polito, V., Reep, J. W., Reeves, K. K., Simões, P. J. A., Dudík, J., Del Zanna, G., Mason, H. E., & Golub, L. 2016, ApJ, 816, 89

Polito, V., Reeves, K. K., Del Zanna, G., Golub, L., & Mason, H. E. 2015, ApJ, 803, 84

Polito, V., Testa, P., & De Pontieu, B. 2019, ApJ, 879, L17

Popowicz, A., Radlak, K., Bernacki, K., & Orlov, V. 2017, Sol. Phys., 292, 187

Procházka, O., Reid, A., Milligan, R. O., Simões, P. J. A., Allred, J. C., & Mathioudakis, M. 2018, ApJ, 862, 76

Radziszewski, K., Rudawy, P., & Phillips, K. J. H. 2011, A&A, 535, A123

Rathore, B., & Carlsson, M. 2015, ApJ, 811, 80

Rathore, B., Carlsson, M., Leenaarts, J., & Pontieu, B. D. 2015, Astrophysical Journal, 811, 81

Rathore, B., Pereira, T. M. D., Carlsson, M., & De Pontieu, B. 2015, ApJ, 814, 70

Reardon, K. P., & Cavallini, F. 2008, A&A, 481, 897

Reep, J. W., Bradshaw, S. J., & McAteer, R. T. J. 2013, ApJ, 778, 76

Righini, A., Cavallini, F., & Reardon, K. P. 2010, A&A, 515, A85

Schmahl, E. J., Pernak, R. L., Hurford, G. J., Lee, J., & Bong, S. 2007, Sol. Phys., 240, 241

Schmelz, J. T., Saba, J. L. R., Chauvin, J. C., & Strong, K. T. 1997, ApJ, 477, 509

Schmieder, B., Forbes, T. G., Malherbe, J. M., & Machado, M. E. 1987, ApJ, 317, 956

Shibata, K., & Magara, T. 2011, Living Reviews in Solar Physics, 8, 6

Shibata, K., Masuda, S., Shimojo, M., Hara, H., Yokoyama, T., Tsuneta, S., Kosugi, T., & Ogawara, Y. 1995, ApJ, 451, L83

Spice Consortium et al. 2020, A&A, 642, A14

Spiegel, E. A., & Zahn, J. P. 1992, A&A, 265, 106

Stark, J. 1913, Nature, 92, 401

Sturrock, P. A. 1966, Nature, 211, 695

Svestka, Z. 1976, Solar Flares (Springer-Verlag)

Sweet, P. A. 1958, in Electromagnetic Phenomena in Cosmical Physics, ed. B. Lehnert, Vol. 6, 123

Tandberg-Hanssen, E., & Emslie, A. G. 1988, The physics of solar flares (Cambridge University Press)

Thalmann, J. K., Su, Y., Temmer, M., & Veronig, A. M. 2015, Astrophysical Journal Letters

Thompson, M. J., Christensen-Dalsgaard, J., Miesch, M. S., & Toomre, J. 2003, ARA&A, 41, 599

Tian, H., Young, P. R., Reeves, K. K., Chen, B., Liu, W., & McKillop, S. 2015, ApJ, 811, 139

Torrence, C., & Compo, G. P. 1998, Bulletin of the American Meteorological Society, 79, 61

Varady, M., Kasparova, J., Moravec, Z., Heinzel, P., & Karlicky, M. 2010, IEEE Transactions on Plasma Science, 38, 2249

Veronig, A. M., & Polanec, W. 2015, Sol. Phys., 290, 2923

Vissers, G. J. M., Rouppe van der Voort, L. H. M., & Rutten, R. J. 2013, ApJ, 774, 32

—. 2019, A&A, 626, A4

Vissers, G. J. M., Rouppe van der Voort, L. H. M., Rutten, R. J., Carlsson, M., & De Pontieu, B. 2015, ApJ, 812, 11

Švestka, Z. 1970, Sol. Phys., 13, 471

Wang, H., Qiu, J., Denker, C., Spirock, T., Chen, H., & Goode, P. R. 2000, ApJ, 542, 1080

Wang, T. J., Solanki, S. K., Innes, D. E., Curdt, W., & Marsch, E. 2003, A&A, 402, L17

Warmuth, A., Holman, G. D., Dennis, B. R., Mann, G., Aurass, H., & Milligan, R. O. 2009, ApJ, 699, 917

Warmuth, A., & Mann, G. 2013, A&A, 552, A86

Warmuth, A., & Mann, G. 2016, Astronomy and Astrophysics

Warren, H. P., Ugarte-Urra, I., & Landi, E. 2014, ApJS, 213, 11

Watanabe, H., Vissers, G., Kitai, R., Rouppe van der Voort, L., & Rutten, R. J. 2011, ApJ, 736, 71

Watanabe, K., & Imada, S. 2020, ApJ, 891, 88

Wöger, F., Rimmele, T., Ferayorni, A., Beard, A., Gregory, B. S., Sekulic, P., & Hegwer, S. L. 2021, Sol. Phys., 296, 145

Wöger, F., & von der Lühe, Oskar, I. 2008, in Society of Photo-Optical Instrumentation Engineers (SPIE) Conference Series, Vol. 7019, Advanced Software and Control for Astronomy II, ed. A. Bridger & N. M. Radziwill, 70191E

Wöger, F., & von der Lühe, O. 2007, Appl. Opt., 46, 8015

Wuelser, J.-P., & Marti, H. 1989, ApJ, 341, 1088

Wülser, J. P., et al. 2018, Sol. Phys., 293, 149

Xia, F., Su, Y., Wang, W., Wang, L., Warmuth, A., Gan, W., & Li, Y. 2021, ApJ, 908, 111

Young, P. R., Doschek, G. A., Warren, H. P., & Hara, H. 2013, ApJ, 766, 127

Young, P. R., Tian, H., & Jaeggli, S. 2015, ApJ, 799, 218

Young, P. R., et al. 2007, PASJ, 59, S857

Zarro, D. M., & Lemen, J. R. 1988, ApJ, 329, 456

Zeeman, P. 1897, Nature, 55, 347

Zharkova, V. V., et al. 2011, Space Sci. Rev., 159, 357

Zhou, Y.-A., Hong, J., Li, Y., & Ding, M. D. 2022, ApJ, 926, 223